Alma Mater Studiorum · University of Bologna

School of Science
Department of Physics and Astronomy
Master's Degree in Physics

Cryogenic optical readout for a liquid argon neutrino imaging detector

Supervisor:
Dr. Gabriele Sirri

Co-supervisor:
Dr. Nicolò Tosi

Submitted by:
Alessandro Badiali

Academic Year 2021/2022

Abstract

The GRAIN detector is part of the SAND Near Detector of the DUNE neutrino experiment.

A new imaging technique involving the collection of the scintillation light will be used in order to reconstruct images of particle tracks in the GRAIN detector.

Silicon photomultiplier (SiPM) matrices will be used as photosensors for collecting the scintillation light emitted at 127 nm by liquid argon. The readout of SiPM matrices inside the liquid argon requires the use of a multi-channel mixed-signal ASIC, while the back-end electronics will be implemented in FPGAs outside the cryogenic environment. The ALCOR (A Low-power Circuit for Optical sensor Readout) ASIC, developed by Torino division of INFN, is under study, since it is optimized to readout SiPMs at cryogenic temperatures.

I took part in the realization of a demonstrator of the imaging system, which consists of a SiPM matrix connected to a custom circuit board, on which an ALCOR ASIC is mounted. The board communicates with an FPGA.

The first step of the present project that I have accomplished was the development of an emulator for the ALCOR ASIC. This emulator allowed me to verify the correct functioning of the initial firmware before the real ASIC itself was available. I programmed the emulator using VHDL and I also developed test benches in order to test its correct working.

Furthermore, I developed portions of the DAQ software, which I used for the acquisition of data and the slow control of the ASICs. In addition, I made some parts of the DAQ firmware for the FPGAs. Finally, I tested the complete SiPMs readout system at both room and cryogenic temperature in order to ensure its full functionality.

Contents

Introduction

DUNE (Deep Underground Neutrino Experiment) is a long-baseline neutrino oscillation experiment that will address some still open questions, as the determination of the neutrino mass ordering, precise measurements of the CP violation phase and of the θ_{23} octant of neutrino mixing matrix. DUNE will consist of a Near Detector complex (ND) and a Far Detector (FD) and will use the neutrino beam with the highest intensity in the world.

The ND will be placed at the Fermi National Accelerator Laboratory (FNAL) close to the neutrino beam source; the FD will be positioned deep underground at the Sanford Underground Research Facility (SURF) in Lead, South Dakota, 1300 km away from the source. The DUNE's FD is designed to be composed of four Liquid Argon Time-Projection Chambers (LArTPCs), with a LAr mass of approximately 17 kt for each cryostat. The DUNE's ND purpose is to monitor the beam at the source, measure the unoscillated neutrinos fluxes and constrain the systematic uncertainties on the analysis of the events at the FD. The ND will be composed of three detectors: two movable and one fixed in an on-axis position. The ND component permanently fixed on the beam axis is called SAND (System for on-Axis Neutrino Detection). The SAND multi-purpose detector will monitor fluxes of neutrinos on the beam axis, with high sensitivity to variations in the neutrino beam. In addition, the accurate control of the configuration, chemical composition and mass of the (anti)neutrino targets in SAND will allow precise measurements of high statistics samples of (anti)neutrino interactions in hydrogen, argon and other nuclear targets.

A small LAr active target detector, with a mass approximately of 1 t, will be placed in the upstream region of the SAND magnetized volume. This detector is called GRAIN (Granular Argon for Interactions of Neutrinos) and it will be used to study neutrino-LAr interactions topology and cross-section. The LArTPCs used in the FD are an established system for the reconstruction of particle tracks. In a LArTPC, the tracks of the charged particles are reconstructed by collecting the ionization charge produced in the liquid argon. However, a traditional LArTPC is not suited for GRAIN, because the electron drift time in a LArTPC is too long (in the order of ms) and would lead to pile-up problems, given the relatively high event rate at the ND.

The GRAIN detector will instead be designed to exploit the abundant scintillation light produced by charged particles (about 40,000 photons/MeV), to perform imaging of particle tracks. The apparatus under development will use an optical detection system capable of collecting the Vacuum Ultraviolet (VUV) LAr scintillation light emitted at 127 nm. Two VUV imaging systems are under study: one is

based on lenses, while the other is based on coded aperture masks. The two technologies have complementary characteristics, and it is possible that the final design will embed both lenses and masks. Regardless of the optical system, SiPM (Silicon Photomultiplier) matrices will be used as photodetectors, since they provide a fast response and have a very low noise at cryogenic temperatures. Furthermore, they are sensitive to a single photon and they are immune to magnetic fields.

A demonstrator of this novel technology is under study. Indeed, the required cryogenic temperature, together with the channel density and the wavelength, pose a real challenge for the implementation of this technology. In particular, the cryogenic temperature modifies the properties and parameters of the readout electronics within the LAr volume. For this reason, the ALCOR (A Low-power Circuit for Optical sensor Readout) mixed-signal ASIC prototype optimized for the readout of SiPMs at cryogenic temperatures is being considered and its usage is under study.

By using a mixed-signal ASIC, the noise is reduced by immediately digitizing the analog signals, which is acquired near the sensor in a cryogenic environment. Besides, a mixed-signal ASIC may consume less power than a discrete amplifier. GRAIN's back-end electronics will instead be implemented in FPGAs outside the cryogenic environment.

I took part in the realization of such a demonstrator with the purpose of proving the imaging capability of the GRAIN system. The demonstrator consists of a 16 $\times$ 16 SiPM matrix mounted onto a custom PCB on which it is possible to mount up to 8 ALCOR ASICs.

In Chap. 1, neutrino physics is illustrated, focusing especially on the oscillation phenomenon, on the experiments and on the still open questions.

The Chap. 2 describes the future DUNE experiment, that together with HK experiment, will represent the next generation of neutrino experiments. In particular, the physics objectives, structure and detectors are outlined.

In Chap. 3, the GRAIN detector is the main topic. The chapter covers the principle of coded aperture imaging, the GRAIN simulations and the description of the GRAIN demonstrator, realized with the purpose of showing the imaging system feasibility. Then, SiPMs theory is shown, together with the ALCOR ASIC that will be used for the demonstrator.

The Chap. 4 is about the development of the DAQ system for the demonstrator. It is described the ALCOR ASIC emulator, which was used to test the link synchronization in the initial stage of the project. Then, they are illustrated the DAQ firmware that can be implemented in FPGAs and the DAQ software that uses the IPbus protocol to communicate with the FPGA.

Finally, in Chap. 5, the measurements performed using the demonstrator system are presented. In particular, they include some preliminary operations, such as the link synchronization, the test pulse generation and the parameter scans, together with measurements with a sensor, performed both at room and cryogenic temperature.

Chapter 1

Neutrino Physics

1.1 Neutrino oscillations

Neutrinos are fermions that interact only via the weak interaction and gravity. Neutrinos were postulated first by Pauli in 1930 to explain how beta decay could conserve energy, momentum and angular momentum. The phenomenon of neutrino oscillations was predicted by Bruno Pontecorvo in 1957 and were later observed in several experiments: neutrino created with a specific flavor were measured to have a different flavor after some path travelled.

Neutrino oscillation are important because they imply that the neutrino has a non-zero mass, which requires a modification to the Standard Model. In 2015 the Nobel Prize for Physics was awarded to T. Kajita and A. McDonald for their contribution to the Super-Kamiokande (SK) and the Sudbury Neutrino Observatory (SNO) experiments, providing experiment evidence of neutrino oscillations, which shows that neutrinos have mass.

1.1.1 Dirac mass term

It is possible to describe neutrinos as Dirac particles and obtain the Dirac mass term. Starting from the Dirac equation:

$$(i\partial\!\!\!/ - m)\nu(x) = 0, \tag{1.1}$$

where $\partial\!\!\!/ \equiv \gamma^\mu \partial_\mu$, it follows the Lagrangian:

$$\mathcal{L}_D(x) = \overline{\nu}(x)(i\partial\!\!\!/ - m)\nu(x), \tag{1.2}$$

and by using the left and right-handed projectors:

$$P_L \equiv \frac{1-\gamma^5}{2} \quad \text{and} \quad P_R \equiv \frac{1+\gamma^5}{2}, \tag{1.3}$$

it is possible to decompose the fermion fields into chiral components: $\nu_L \equiv P_L\nu$ and $\nu_R \equiv P_R\nu$, such that $\nu = \nu_L + \nu_R$.

Thus, the Lagrangian can be rewritten as:

$$\mathcal{L}_D = \overline{\nu}_l i\partial\!\!\!/\nu_L + \overline{\nu}_R i\partial\!\!\!/\nu_R - m(\overline{\nu}_l\nu_R + \overline{\nu}_R\nu_L), \tag{1.4}$$

but since neutrinos do not possess a mass in the Standard Model (SM), neutrinos fields have only the left-handed component ν_L, while all the other elementary fermion fields (charged leptons and quarks) have both components [1].

However, oscillation experiments have shown that neutrinos are massive, subsequently it is necessary to extend the SM Lagrangian by considering also the right-handed component ν_R. Three fields are therefore obtained:

$$L'_{\alpha L} \equiv \begin{pmatrix} \nu'_{\alpha L} \\ l'_{\alpha L} \end{pmatrix}, \quad l'_{\alpha R}, \quad \nu'_{\alpha R}, \quad (\alpha = e, \mu, \tau) \tag{1.5}$$

which enter in the Lepton-Higgs Yukawa Lagrangian:

$$\mathcal{L}_{H,L} = -\sum_{\alpha,\beta=e,\mu,\tau} \left[Y''^{l}_{\alpha\beta} \overline{L}'_{\alpha L} \Phi l'_{\beta R} + Y''^{\nu}_{\alpha\beta} \overline{L}'_{\alpha L} \tilde{\Phi} \nu'_{\beta R} \right] + h.c., \tag{1.6}$$

with

$$\Phi(x) = \frac{1}{\sqrt{2}} \begin{pmatrix} 0 \\ v + H(x) \end{pmatrix}, \quad \tilde{\Phi}(x) = i\sigma_2 \Phi^* = \frac{1}{\sqrt{2}} \begin{pmatrix} v + H(x) \\ 0 \end{pmatrix}, \tag{1.7}$$

after spontaneous symmetry breaking. Thus, the Lagrangian becomes

$$\mathcal{L}_{H,L} = -\left(\frac{v + H}{\sqrt{2}} \right) \left[\overline{l}'_L Y''^{l} l'_R + \overline{\nu}'_L Y''^{\nu} \nu'_R \right] + h.c., \tag{1.8}$$

where Y''^{l} and Y''^{ν} can be diagonalized using the unitary transformations $l'_L = V^l_L l_L$, $l'_R = V^l_R l_R$, $\nu'_L = V^\nu_L n_L$, $\nu'_R = V^\nu_R n_R$, which are allowed since they leave invariant the kinetic terms in the Lagrangian.

Subsequently, defining the diagonal matrices as $V^{l\dagger}_L Y'_l V^l_R = Y^l$ and $V^{\nu\dagger}_L Y'_\nu V^\nu_R = Y^\nu$, it is possible to write the Lagrangian as

$$\mathcal{L}_{H,L} = -\left(\frac{v + H}{\sqrt{2}} \right) \left[\overline{l}_L Y^l l_R + \overline{n}_L Y^\nu n_R \right] + h.c. \tag{1.9}$$

$$= -\left(\frac{v + H}{\sqrt{2}} \right) \left[\sum_{\alpha=e,\mu,\tau} y^l_\alpha \overline{l}_{\alpha L} l_{\alpha R} + \sum_{k=1}^{3} y^\nu_k \overline{\nu}_{kL} \nu_{kR} \right] + h.c., \tag{1.10}$$

where the mass eigenstates are

$$V^{l\dagger}_L l'_L = l_L \equiv \begin{pmatrix} e_L \\ \mu_L \\ \tau_L \end{pmatrix}, \quad V^{l\dagger}_R l'_R = l_L \equiv \begin{pmatrix} e_R \\ \mu_R \\ \tau_R \end{pmatrix}, \tag{1.11}$$

$$V^{\nu\dagger}_L \nu'_L = n_L \equiv \begin{pmatrix} \nu_{1L} \\ \nu_{2L} \\ \nu_{3L} \end{pmatrix}, \quad V^{\nu\dagger}_R \nu'_R = n_R \equiv \begin{pmatrix} \nu_{1R} \\ \nu_{2R} \\ \nu_{3R} \end{pmatrix}. \tag{1.12}$$

However, since $l_\alpha \equiv l_{\alpha L} + l_{\alpha R}$ and $\nu_k \equiv \nu_{kL} + \nu_{kR}$, the Lagrangian can be written separating the mass terms from the lepton-Higgs couplings as it follows

$$\mathcal{L}_{H,L} = -\sum_{\alpha=e,\mu,\tau} \frac{y^l_\alpha v}{\sqrt{2}} \bar{l}_\alpha l_\alpha - \sum_{k=1}^{3} \frac{y^\nu_k v}{\sqrt{2}} \overline{\nu}_k \nu_k$$
$$- \sum_{\alpha=e,\mu,\tau} \frac{y^l_\alpha}{\sqrt{2}} \bar{l}_\alpha l_\alpha H - \sum_{k=1}^{3} \frac{y^\nu_k}{\sqrt{2}} \overline{\nu}_k \nu_k H. \tag{1.13}$$

Therefore, comparing the Dirac mass terms with the present Lagrangian, it is possible to obtain the following relations

$$m_\alpha = \frac{y_\alpha^l v}{\sqrt{2}}, \quad m_k = \frac{y_k^\nu v}{\sqrt{2}}, \tag{1.14}$$

which make evident that the lepton-Higgs couplings are proportional to the lepton masses.

1.1.2 PMNS neutrino mixing matrix

It is possible to write the charged-current weak interaction Lagrangian as

$$\mathcal{L}_{CC} = -\frac{g}{2\sqrt{2}} j_W^\rho W_\rho + h.c., \tag{1.15}$$

where the weak charged current is given by the sum of the leptonic and quark currents. The leptonic weak charged-current can be written as

$$j_{W,L}^{\rho\dagger} = 2 \sum_{\alpha=e,\mu,\tau} \overline{L}'_{\alpha L} \gamma^\rho \nu'_{\alpha L} = 2\bar{l}'_L \gamma^\rho \nu'_L, \tag{1.16}$$

which, using the unitary transformations $l'_L = V_L^l l_L$ and $\nu'_L = V_L^\nu n_L$, can subsequently be written as

$$\begin{aligned} j_{W,L}^{\rho\dagger} &= 2\bar{l}_L V_L^{l\dagger} \gamma^\rho V_L^\nu n_L \\ &= 2\bar{l}_L \gamma^\rho V_L^{l\dagger} V_L^\nu n_L \\ &= 2\bar{l}_L \gamma^\rho U n_L, \end{aligned} \tag{1.17}$$

in which the mixing matrix $U = V_L^{l\dagger} V_L^\nu$ was used [2].

The introduction of a mixing matrix brings the definition of the left-handed flavor neutrino fields as it follows

$$\nu_L = U n_L = V_L^{l\dagger} V_L^\nu n_L = V_L^{l\dagger} \nu'_L = \begin{pmatrix} \nu_{eL} \\ \nu_{\mu L} \\ \nu_{\tau L} \end{pmatrix}, \tag{1.18}$$

and they allow to write the leptonic weak charged current as in the SM:

$$j_{W,L}^{\rho\dagger} = 2\bar{l}_L \gamma^\rho \nu_L = 2 \sum_{\alpha=e,\mu,\tau} \bar{l}_{\alpha L} \gamma^\rho \nu_{\alpha L}. \tag{1.19}$$

Each left-handed flavor neutrino field is associated with the corresponding charged lepton field which describes a massive charged lepton. Basically, left-handed flavor neutrino fields are useful for calculations in SM approximation of massless neutrinos interactions, while if neutrino masses have to be taken into account, it is necessary to consider also the mixing matrix using

$$j_{W,L}^{\rho\dagger} = 2\bar{l}_L \gamma^\rho U n_L = 2 \sum_{\alpha=e,\mu,\tau} \sum_{k=1}^{3} \bar{l}_{\alpha L} \gamma^\rho U_{\alpha k} \nu_{kL}. \tag{1.20}$$

While in the standard model with massless neutrinos all lepton quantum numbers (L, L_e, L_μ, L_τ) are conserved, one can see that, when neutrino masses are considered, just the total lepton number L is conserved, because the Lagrangian is invariant under global $U(1)$ gauge transformations. Instead, single lepton quantum numbers are not conserved by the Dirac mass term.

The unitary mixing matrix U is called PMNS (Pontecorvo-Maki-Nakagawa-Sakata) matrix and is defined as

$$U = V_L^{l\dagger} V_L^{\nu} = \begin{pmatrix} U_{e1} & U_{e2} & U_{e3} \\ U_{\mu 1} & U_{\mu 2} & U_{\mu 3} \\ U_{\tau 1} & U_{\tau 2} & U_{\tau 3} \end{pmatrix} \tag{1.21}$$

Then, thanks to the PMNS matrix, it is possible to express the neutrino flavor basis in function of the neutrino mass basis:

$$\begin{pmatrix} \nu_{eL} \\ \nu_{\mu L} \\ \nu_{\tau L} \end{pmatrix} = \begin{pmatrix} U_{e1} & U_{e2} & U_{e3} \\ U_{\mu 1} & U_{\mu 2} & U_{\mu 3} \\ U_{\tau 1} & U_{\tau 2} & U_{\tau 3} \end{pmatrix} \begin{pmatrix} \nu_{1L} \\ \nu_{2L} \\ \nu_{3L} \end{pmatrix} \tag{1.22}$$

Since a unitary $N \times N$ matrix depends on N^2 independent real parameters, the PMNS matrix has 9 parameters, which are 3 mixing angles and 6 phases. However, just one of these phases is physical and taking this into account, the physical parameters are just four: 3 mixing angles $\theta_{12}, \theta_{23}, \theta_{13}$ and 1 phase δ_{13}. These parameters enter in the standard parametrization of the PMNS matrix as it follows

$$U = \begin{pmatrix} 1 & 0 & 0 \\ 0 & c_{23} & s_{23} \\ 0 & -s_{23} & c_{23} \end{pmatrix} \begin{pmatrix} c_{13} & 0 & s_{13}e^{-i\delta_{13}} \\ 0 & 1 & 0 \\ -s_{13}e^{i\delta_{13}} & 0 & c_{13} \end{pmatrix} \begin{pmatrix} c_{12} & s_{12} & 0 \\ -s_{12} & c_{12} & 0 \\ 0 & 0 & 1 \end{pmatrix}, \tag{1.23}$$

where $c_{ab} \equiv \cos\theta_{ab}, s_{ab} \equiv \sin\theta_{ab}$ and $0 \leq \theta_{ab} \leq \frac{\pi}{2}, 0 \leq \delta_{13} < 2\pi$. The PMNS matrix is given by the product of three independent matrices and each of them belong to a different interactions' sector.

1.1.3 Neutrino oscillations in vacuum

Using the PMNS matrix, it is possible to write the neutrino flavor eigenstate at the source, considered at the initial time $t = 0$:

$$|\nu(t=0)\rangle = |\nu_\alpha\rangle = U_{\alpha 1}^* |\nu_1\rangle + U_{\alpha 2}^* |\nu_2\rangle + U_{\alpha 3}^* |\nu_3\rangle. \tag{1.24}$$

At a certain time $t > 0$ the neutrino propagated state will be

$$|\nu(t>0)\rangle = U_{\alpha 1}^* e^{-iE_1 t} |\nu_1\rangle + U_{\alpha 2}^* e^{-iE_2 t} |\nu_2\rangle + U_{\alpha 3}^* e^{-iE_3 t} |\nu_3\rangle, \tag{1.25}$$

where, using natural units, $E_k^2 = p^2 + m_k^2$ and $t = L$ if it is considered a detector with a distance L from the source. The detector will then measure a neutrino eigenstate $|\nu_\beta\rangle \neq |\nu_\alpha\rangle$, depending on the oscillation probability

$$P_{\nu_\alpha \to \nu_\beta}(L) = |\langle \nu_\beta \,|\, \nu(L) \rangle|^2 = \sum_{k,j} U_{\beta k} U_{\alpha k}^* U_{\beta j}^* U_{\alpha j} \exp\left(-i \, \frac{\Delta m_{kj}^2 L}{2E} \right), \tag{1.26}$$

where $\Delta m^2_{kj} \equiv m^2_k - m^2_j$ is the difference between neutrino masses squared.

Despite the oscillation probability formula being really complex, in some cases, it is possible to consider just two neutrino flavors at a time. This approximation is based on the fact that depending on the different physical processes, the order of magnitude of Δm^2_{kj} is completely different, which allows the decoupling of neutrinos interactions, considering just two flavors.

Therefore, considering just two neutrinos the mixing matrix becomes

$$U = \begin{pmatrix} \cos\theta & \sin\theta \\ -\sin\theta & \cos\theta \end{pmatrix}, \tag{1.27}$$

and then the flavor eigenstates are

$$|\nu_\alpha\rangle = \cos\theta|\nu_k\rangle + \sin\theta|\nu_j\rangle \qquad |\nu_\beta\rangle = -\sin\theta|\nu_k\rangle + \cos\theta|\nu_j\rangle. \tag{1.28}$$

Defining $\Delta m^2 \equiv m^2_k - m^2_j$, it is possible to calculate the transition probability formula, which can be written in natural units as

$$P_{\nu_\alpha\to\nu_\beta} = P_{\nu_\beta\to\nu_\alpha} = \sin^2 2\theta \sin^2\left(\frac{\Delta m^2 L}{4E}\right). \tag{1.29}$$

Hence, the survival probabilities are

$$P_{\nu_\alpha\to\nu_\alpha} = P_{\nu_\beta\to\nu_\beta} = 1 - P_{\nu_\alpha\to\nu_\beta}. \tag{1.30}$$

While, using S.I. units, the transition probability can be written as

$$P_{\nu_\alpha\to\nu_\beta} = \sin^2 2\theta \sin^2\left(1.267\,\frac{\Delta m^2[\mathrm{eV}^2]L[\mathrm{km}]}{E[\mathrm{GeV}]}\right). \tag{1.31}$$

Neutrino oscillations are perfect to measure tiny neutrino masses, since even if Δm^2 is small, the oscillation probability can be amplified by a long baseline L, thus oscillations are observable at macroscopic distances.

At large L or, alternatively, at small E, the oscillation probability tends to the constant value of $\langle P_{\nu_\alpha\to\nu_\beta}\rangle = \frac{1}{2}\sin^2 2\theta$, due to the effect of finite energy resolution, as shown in Fig. 1.1. In fact, the uncertainty relation $1 \sim \Delta E \Delta t \simeq \frac{\Delta m^2}{2E} L$ holds.

In addition, the plane wave treatment of neutrino oscillation is just an approximation. Indeed, since a plane wave has a definite momentum p, it would be impossible to know where the neutrino was produced due to the Heisenberg principle, and then, the distance L would be unknown. It is then necessary to describe each mass eigenstate using a wave packet, which can have a different mass. During time propagation, the wave packets will separate and, as a consequence, there will be no more oscillations. In summary, different mass eigenstates produced at the same instant arrive at separate times, depending on their individual speeds. E.g. supernova neutrinos are no longer oscillating when they reach the Earth: since separation occurs approximately in 10^3 km, they would arrive with a time difference in the order of 10^{-4} s.

Neutrinos come from different sources: the sun, cosmic rays interaction with the atmosphere, nuclear reactors and accelerators. Each of this source produces

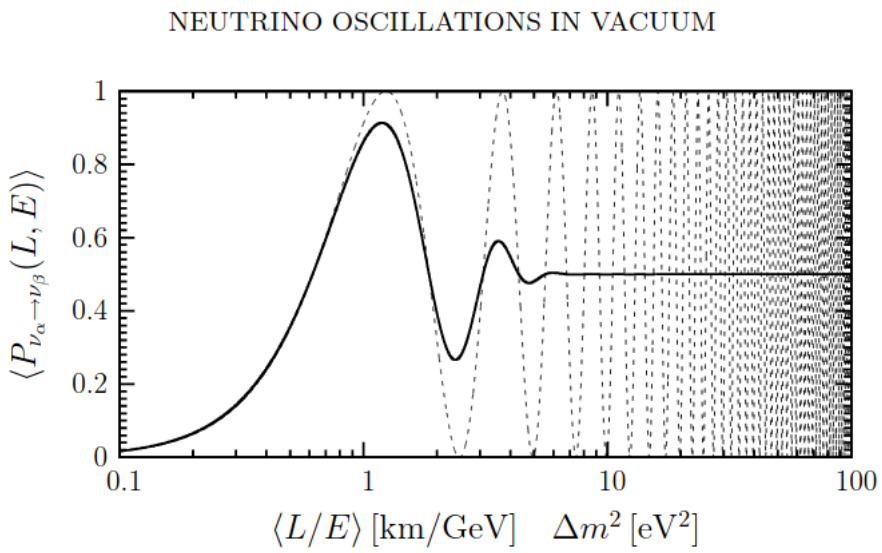

Figure 1.1: Probability of $\nu_\alpha \to \nu_\beta$ transitions for $\sin^2 2\theta = 1$ as a function of $\Delta m^2 \langle L/E \rangle$. The solid line represents the transition probability averaged over a Gaussian L/E distribution with $\sigma_{L/E} = 0.2\langle L/E \rangle$. The dashed line is the unaveraged transition probability [1].

neutrinos with different parameters L and E, and thus with a different accessible Δm^2. Therefore, various experiments were designed to exploit these neutrino sources and to probe different neutrino sectors.

Two possible modes are available for the measure of neutrino oscillations: appearance or disappearance. In both cases, a neutrino source is used. Then, some experiments use a small near detector to measure the neutrino flux near the source, in order to make sure of the composition of the initial flux, while a large far detector measures the neutrino flux after a distance L. The appearance experiments start with a neutrino flavor ν_α at the source and the far detector looks for a different neutrino flavor ν_β at distance L from the source, measuring the appearance probability $P_{\nu_\alpha \to \nu_\beta}$; while the disappearance experiments look for the same neutrino flavor ν_α at distance L from the source, measuring the disappearance probability $P_{\nu_\alpha \to \nu_\alpha}$.

1.2 Atmospheric neutrinos

Atmospheric neutrinos are produced as a consequence of cosmic rays interacting with the atmosphere: pions are produced, which can decay into a muon and a muon neutrino, as exemplified in Fig. 1.2. Low energy muons can then decay again in an electron, an electron neutrino and a muon neutrino.

At the beginning of the '80s, some theories predicted that the proton could decay, e.g. through the decay $p \to e^+ \pi^0 \nu_e$, with a measurable lifetime. In order to prove this possibility, huge detectors were build with size on the order of 10^3 m^3 and mass of 1 kton.

Atmospheric neutrinos interactions represent the main background for the de-

tection of proton decay and that is the reason why their fluxes were studied in detail. In the end, proton decay was not discovered, but neutrino oscillations were observed.

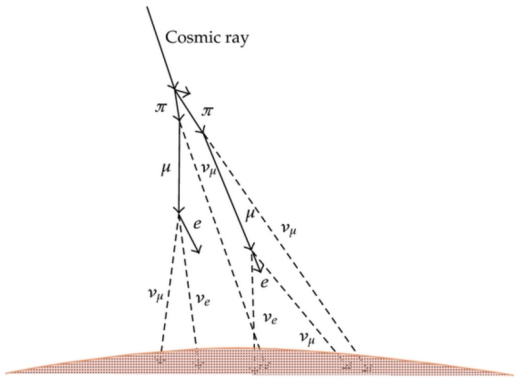

Figure 1.2: Schematic drawing of the production of atmospheric neutrinos [3].

1.2.1 Super-Kamiokande

The experiment Super-Kamiokande (SK) in Japan, was designed for the search of proton decays. It was build 1,000 m underground, to be shielded from cosmic rays muons and it was a Cherenkov detector, which used 50,000 ton of water as radiator, with more than 10,000 PMTs to collect the produced photons. SK's interior is displayed in Fig. 1.3.

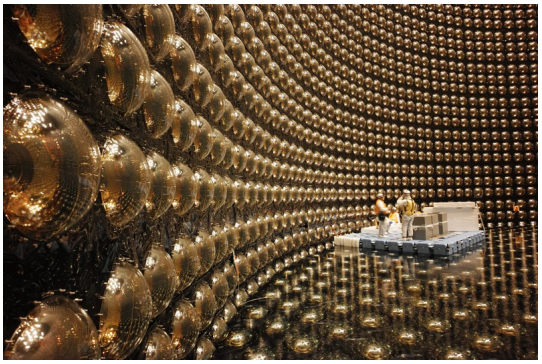

Figure 1.3: Inside the Super-Kamiokande neutrino detector during work on the detectors. Credit: Kamioka Observatory, ICRR, Univ. Tokyo.

The reconstruction of the events was done using the Cherenkov light detected as a ring by PMTs, as exemplified in Fig. 1.4. The vertex was reconstructed using the timing information, the direction using the cone and the energy was measured using the total light collected. Muon neutrinos interactions produce a muon, which produces a very sharp ring, since it is a minimum ionizing particle, while electron neutrinos interactions produce an electron which produces a fuzzy ring, since it scatters more.

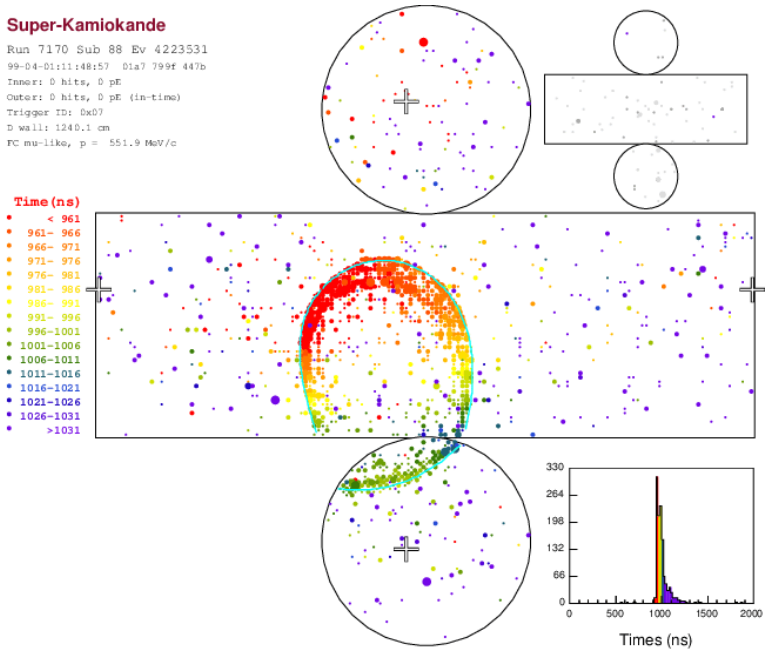

Figure 1.4: An example event display from the Super-Kamiokande detector, showing the sharp-edged Cherenkov ring from a 0.6 GeV muon. Each small circle represents one PMT over threshold, with the size of the circle correlated with the number of photoelectrons, and the color of the circle related to the arrival time of the Cherenkov light [4].

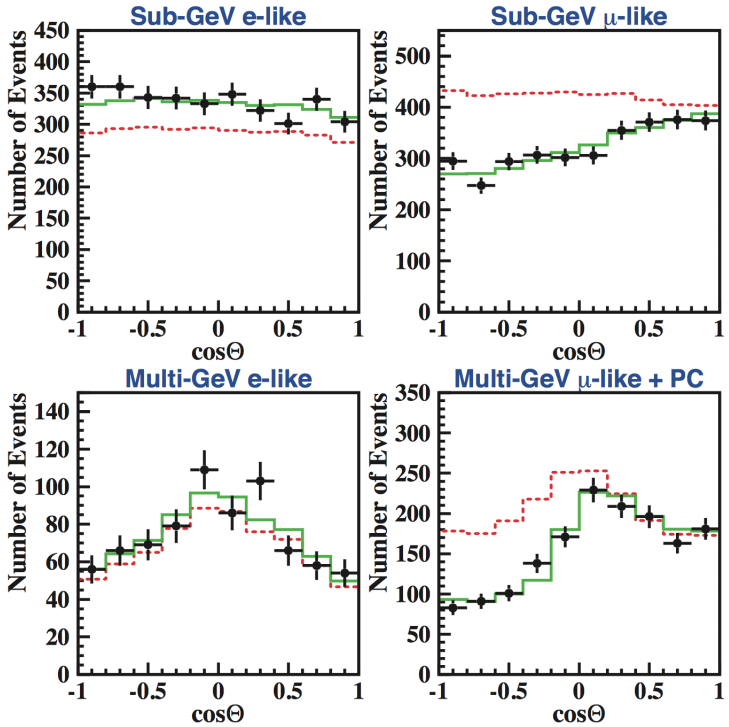

Figure 1.5: SK experiment's measurement of muon or electron neutrino flux as a function of the arrival direction of the neutrinos. $\cos\theta = -1$ means upward going. It shows that muon neutrinos disappear, because they change flavor, during their travel through Earth. The red-dotted line shows the expectations in case of no-oscillation [5].

The energy range was between 0.2 GeV and 100 GeV, while the distance range was between 10 km, for neutrinos travelling the shortest distance not through the Earth, and 13,000 km, for neutrinos travelling for a distance equal to the full diameter of the Earth.

SK observed the dependencies on the zenith angle of electronic and muon neutrinos. These distributions gave interesting results: while for the electron neutrinos the data and the MC simulations were compatible, for the muon neutrinos there was observed a large deficit of the data w.r.t. the MC simulations, especially in the region where the cosine of the zenith angle was equal to -1, which corresponded to a travelled path of 13,000 km. The results can be found in Fig. 1.5.

Since electron neutrino flux had no excess, the deficit could be explained considering neutrino oscillations of muon neutrinos into tau neutrinos, another neutrino flavor which was still not discovered at that time. The best fits gave as parameters $\Delta m^2_{23} \simeq 2.0 \times 10^{-3}$ eV^2 and $\sin^2 2\theta_{23} \simeq 1.00$.

Indeed, thanks to a measure of an exclusion region, which is reported in Fig. 1.6, the Chooz experiment was able to exclude the possibility to have $\nu_\mu \to \nu_e$ oscillations for atmospheric neutrinos events.

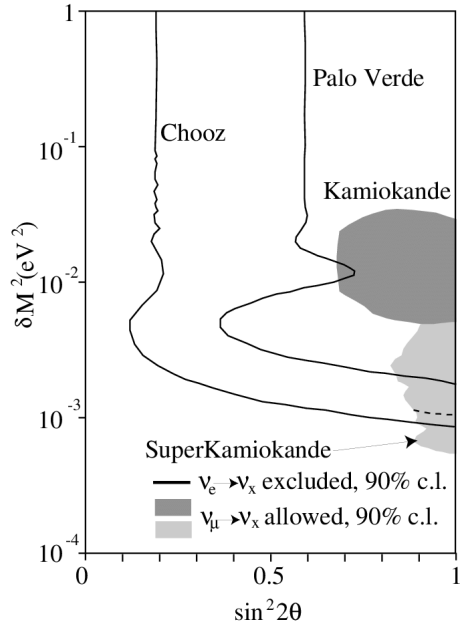

Figure 1.6: Exclusion plot for reactor neutrino experiments. Also shown is the allowed region from the atmospheric experiments. The dotted line in the SK region indicates a lower bound on Δm^2 obtained from an analysis of upward-going muon data [6].

1.2.2 Artificial neutrino beam experiments

Experiments with artificial neutrino beams were designed in order to verify the atmospheric neutrinos oscillations parameters, using a similar L/E ratio.

To obtain a neutrino beam, a proton beam is used to hit a target. The target has to be able to sustain high temperatures without fusing, for example it can be made of graphite. From the beam-target interactions, hadrons are produced. The main products are pions since they are the lightest, but also some kaons are

produced. Then magnetic horns are used to produce neutrino or antineutrino beams. In particular, is possible to change the horns' polarity to focus positive (negative) hadrons, which subsequently are injected into beam pipes to let them decay into neutrino (antineutrinos), due to lepton number conservation rules.

For example, if a neutrino beam is desired, positive charged particle will be selected. In this case, most of the neutrinos come from $\pi^+ \to \mu^+\nu_\mu$, therefore are muon neutrinos, but there can be a beam contamination due to electron neutrinos or antineutrinos from different reactions: if the produced muon decays following $\mu^+ \to e^+\nu_e\overline{\nu}_\mu$ (0.01 contamination from both ν_e and $\overline{\nu}_\mu$), if the pion decays into an electron $\pi^+ \to e^+\nu_e$ (10^{-4} contamination, since this process is suppressed due to a chirality term that is very small because it depends on the electron mass), if a produced kaon (produced with a 10% probability w.r.t. the pion) decays as $K^+ \to \pi^0 e^+\nu_e$ (0.005 contamination, since the branching ratio of this decay is 5%).

The angle with which the neutrino is produced w.r.t. the pion direction of fly is small, since it can be shown that $\theta_C \sim \frac{1}{\gamma_\pi} = \frac{m_\pi}{E_\pi} << 1$, but since the distance L can be very large, it is important to consider it in the design of a far detector.

The experiments which confirmed the atmospheric neutrino oscillations were K2K ($E \sim 1$ GeV, $L \sim 250$ km) and MINOS ($E \sim 3$ GeV, $L \sim 750$ km), both of them were disappearance experiments. MINOS' results are shown in Fig. 1.7, together with previous experiments.

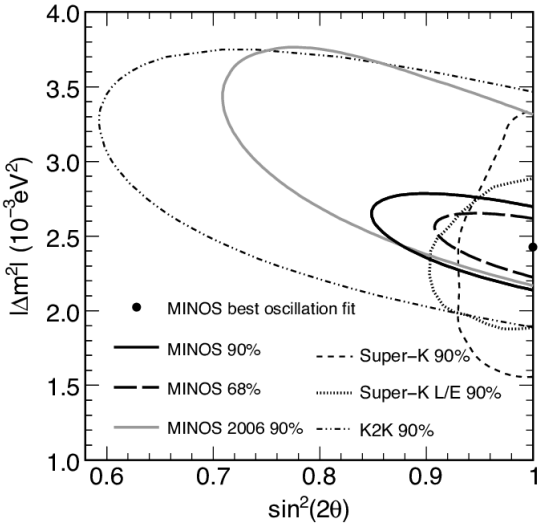

Figure 1.7: MINOS contours for the oscillation fit to experimental data, including systematic errors. Contours from SK, K2K and earlier MINOS result are shown [7].

One can see that while natural experiments have a better resolution on the mixing angle measurement since it is possible to have a large statistics, artificial experiments posses a better resolution on the squared mass difference since they allow a more precise parameters L and E determination. MINOS final results are: $\Delta m^2_{23} = (2.43 \pm 0.13) \times 10^{-3}$ eV^2 (68% cl) and $\sin^2 2\theta_{23} > 0.90$ (90% cl) [8]. More recently, the OPERA experiment ($E \sim 17.7$ GeV and $L \sim 730$ km) had also measured the flux of ν_τ, measuring the appearance probability.

1.3 Solar neutrinos

Photons from the solar core takes a million years to reach the surface, while neutrinos generated by fusion processes take just 2 s. Thus, neutrinos can be used to probe the solar core properties.

For this reason, neutrino fluxes were studied in detail and are described by Bahcall's solar standard model. On earth, a flux of 4.0×10^{10} cm^{-2}s^{-1} electron neutrinos arrives. These neutrinos come mainly from the *pp* cycle, with a continuous distribution with energy under 0.5 MeV, but there are other reactions that bring neutrino with different energies. Therefore, the neutrino flux depends on the neutrino energy and it can be observed in Fig. 1.8.

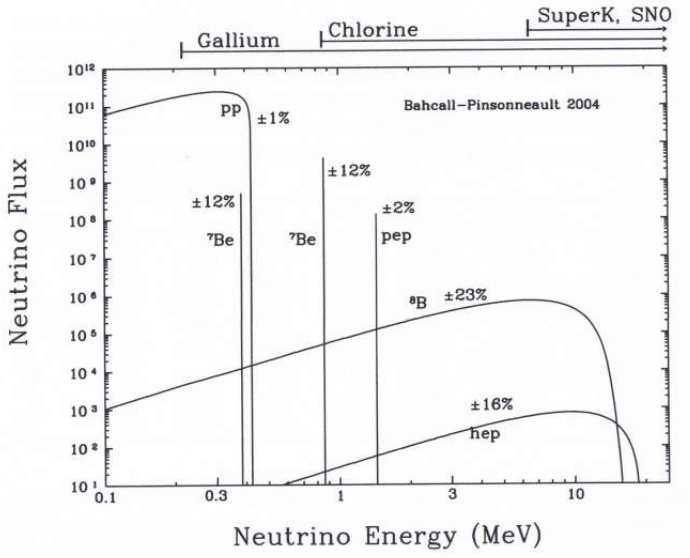

Figure 1.8: The energy spectrum of neutrinos from the pp chain of interactions in the Sun, as predicted by the standard solar model. Neutrino fluxes from continuum sources (pp, hep, ^8B) are given in the units of counts per cm^2 per second. The pp chain is responsible for more than 98% of the energy generation in the standard solar model. The arrows at the top of the figure indicate the energy thresholds for the past neutrino experiments.

1.3.1 Solar neutrino flux problem

Different experiments tried to measure the neutrino fluxes for different energies. The first one was the Homestake experiment, in which the reaction $\nu_e + {}^{37}\mathrm{Cl} \rightarrow {}^{37}\mathrm{Ar} + e^-$ was used to detect the ν_e flux, with an energy threshold above 800 keV. Therefore, it was sensitive just to ^{8}B and ^{7}Be electron neutrinos. Homestake observed only one third of the expected number of solar neutrinos as predicted by Bahcall's model.

The possible explanations were three: the solar model is imprecise, the experiment is not calibrated in a proper way or there is some physical phenomenon that happens to neutrinos as they travel from the Sun to the Earth. Other experiments measured then the solar neutrino flux, such as SK, GALLEX and SAGE experiments, but they also observed a deficit. Indeed, they measured, respectively, approximately a neutrino flux of 0.5 and 0.6 w.r.t. the flux predicted by

the standard solar model. SK used the elastic scattering $\nu_l e^- \rightarrow \nu_l e^-$ and used the direction given by the Cherenkov light to distinguish between background and solar neutrinos. SK was able to measure ^{8}B solar neutrinos with energy threshold higher than 5 MeV. Meanwhile, both GALLEX and SAGE experiments were based on the reaction $\nu_e + {}^{71}\text{Ga} \rightarrow {}^{71}\text{Ge} + e^-$ and were sensitive also to *pp* neutrinos, since this reaction has a threshold of energy of about 0.2 MeV. An important improvement was made w.r.t. Homestake: an artificial source of neutrinos was put inside the detector to calibrate effectively the measurements. However, a deficit was still present.

The reason could have been that ν_e oscillates into ν_μ or ν_τ, but neutrinos from the sun have energies in the order of few MeV, too low to have charged current interactions. The problem was that the detectors were only sensitive to charge current interactions and then they were not able to observe the other neutrino flavors, but they measured just a reduced ν_e flux. Therefore, it was necessary to measure the neutral current interaction rate, which had to be equal to the solar model neutrino flux.

The SNO (Sudbury Neutrino Observatory) was then build in Canada for that purpose. It was a liquid scintillator, with 1,000 ton of heavy water (D_2O) and 10,000 PMTs. The main reactions that were used are: the charged current interaction $\nu_e + d \rightarrow p + p + e^-$, which is sensitive just to the ν_e flux; the neutral current interaction $\nu_l + d \rightarrow p + n + \nu_l$, which is sensitive to all neutrino flavor fluxes equally; the elastic scattering $\nu_l e^- \rightarrow \nu_l e^-$, which is sensitive to all neutrino flavors, but six times more sensitive to the ν_e flux. The resulting measured fluxes where compatible with Bahcall's model. Therefore, the problem could be explained with neutrino oscillations. The results from SNO measurements are illustrated in Fig. 1.9.

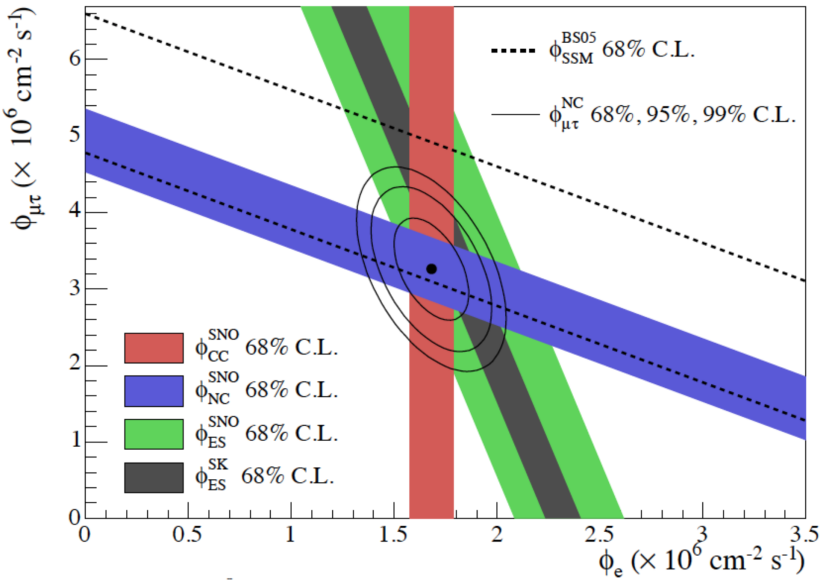

Figure 1.9: Measurement by the SNO experiment of muon and tau neutrino flux from the Sun as a function of the electron neutrino flux, showing that the total flux is consistent with solar models [5].

1.3.2 Matter effect and mass ordering

Another problem arises if it is assumed that neutrinos leave the Sun as ν_e and oscillate just for the distance between Sun and Earth. If this was the case, the distance would be $L \sim 10^8$ km and the energy $E < 10$ MeV, then $\Delta m^2_{12} \sim 3 \times 10^{-10}$ eV^2, but experimentally it is obtained a value of $\Delta m^2_{12} \simeq 7 \times 10^{-5}$ eV^2.

Oscillations come from phase differences between mass states. Therefore, while in vacuum the free Hamiltonian has to be considered, in a material there are also interaction potentials. It is important to consider also the path that neutrinos have to travel inside the Sun, since the density of electron is really high, and electron neutrinos travelling in matter experience extra charged current interactions that the other flavor cannot, since just electron are present. The additional interaction potential $V_W = \sqrt{2} G_F N_e$ modifies the oscillation probability. This phenomenon is called MSW and it is due to matter effects.

The oscillation probability becomes

$$P_{\nu_e \to \nu_e} = 1 - \sin^2 2\theta_M \sin^2 \left(\frac{\Delta m^2_M L}{4E} \right), \tag{1.32}$$

with a squared mass difference due to matter effect equals to

$$\Delta m^2_M = \Delta m^2_V \sqrt{\sin^2 2\theta + (\cos^2 2\theta - \zeta)^2} \tag{1.33}$$

and a relation for the matter effect mixing angle such as

$$\sin^2 2\theta_M = \frac{\sin^2 2\theta}{\sin^2 2\theta + (\cos^2 2\theta - \zeta)^2}, \tag{1.34}$$

where Δm^2_V and θ are the values referred to oscillations in the vacuum, while ζ is linked to the matter electron density and it is given by

$$\zeta = \frac{2\sqrt{2} G_F N_e E}{\Delta m^2_V}. \tag{1.35}$$

From these formulas, it is possible to determine the sign of Δm^2_{12}. In fact, $\Delta m^2_{12} \equiv m^2_2 - m^2_1$ must be positive and then $m_2 > m_1$, otherwise there could not be any resonance and oscillations would not happen. Indeed, only if $\Delta m^2_{12} > 0$, $\zeta = \frac{2\sqrt{2} G_F N_e E}{|\Delta m^2_V|}$ is positive and then

$$\sin^2 2\theta_M = \frac{\sin^2 2\theta}{\sin^2 2\theta + (\cos^2 2\theta - |\zeta|)^2}, \tag{1.36}$$

would allow resonances. In conclusion, the matter effects on neutrino oscillations can be used to measure the mass ordering for the solar sector neutrinos.

1.3.3 Experimental confirmation of solar neutrino oscillations

The KamLAND artificial neutrino experiment was made with a similar L/E ratio as the neutrinos from the Sun, to confirm the observations of the oscillations. A

nuclear reactor was used as neutrino source and the reaction $\overline{\nu}_e + p \rightarrow e^+ + n$ was exploited for the detection of $\overline{\nu}_e$. The parameter values obtained were $\Delta m^2_{12} \simeq 7.53 \times 10^{-5}$ eV^2 and $\tan^2\theta_{12} \simeq 0.436$. KamLAND's results are shown in Fig. 1.10.

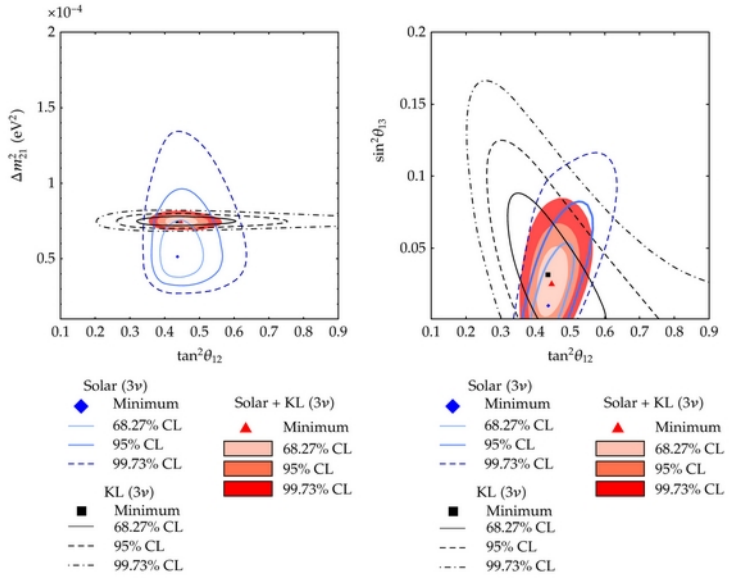

Figure 1.10: Three-flavor neutrino oscillation analysis contour using both solar neutrinos and KamLAND results [9].

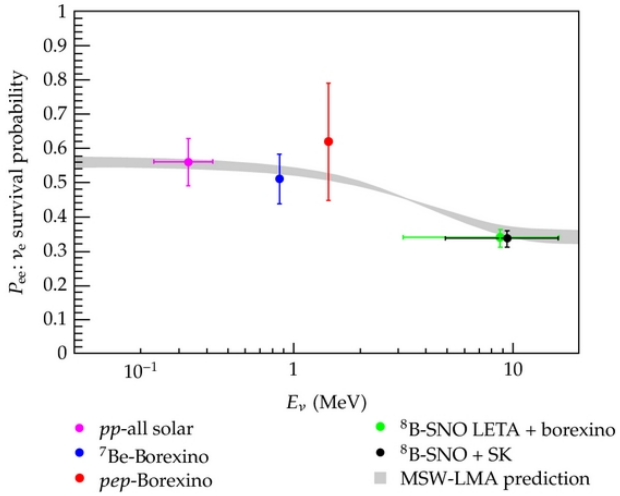

Figure 1.11: The survival probability is represented as a function of neutrino energy. The gray band represents the prediction due to matter effect. The higher survival probability region at low energies is where vacuum-dominated oscillations occur. As the neutrino energy increases, matter effects become important and the lower survival probability at high energies is due to matter-enhanced oscillations. The reported data correspond to solar neutrino flux measurements performed by different experiments [10].

In order to put together all the results from different experiments and solve the solar neutrino puzzle, Borexino experiment studied the survival probability in

function of the energy of the neutrinos, in a range between 10^{-1} MeV and 10 MeV, as shown in Fig. 1.11.

Borexino's results gave a clear picture of the neutrino fluxes, explaining that the observed neutrino fluxes were different for different energies, as predicted by the MSW model in the vacuum regime.

1.4 1-3 sector

Neutrino experiments measured the parameters for both the solar sector oscillations $\nu_\mu \to \nu_e$ and the atmospheric sector oscillations $\nu_\mu \to \nu_\tau$. The measured parameters were respectively $\theta_{12} = (33.7 \pm 1.1)°$, $\Delta m^2_{12} = (7.54 \pm 0.24) \times 10^{-5}$ eV^2 and $\theta_{23} = (42 \pm 3)°$, $\Delta m^2_{23} = |(2.43 \pm 0.06) \times 10^{-3}|$ eV^2.

Therefore, the only oscillation parameter what was still missing was the θ_{13}. Two experimental ways were accessible: accelerator or reactor experiments, both using atmospheric L/E ratio. Accelerator experiments measured the appearance of ν_e in a ν_μ beam, measuring then the oscillation probability

$$P_{\nu_\mu \to \nu_e} = \sin^2 2\theta_{13} \sin^2 \theta_{23} \sin^2 \left(1.27 \, \frac{\Delta m^2_{23} L}{E} \right), \tag{1.37}$$

while reactor experiments measured the disappearance of $\overline{\nu}_e$, measuring the disappearance oscillation probability

$$P_{\overline{\nu}_e \to \overline{\nu}_l} = 1 - \sin^2 2\theta_{13} \sin^2 \left(1.27 \, \frac{\Delta m^2_{23} L}{E} \right). \tag{1.38}$$

1.4.1 Daya Bay experiment

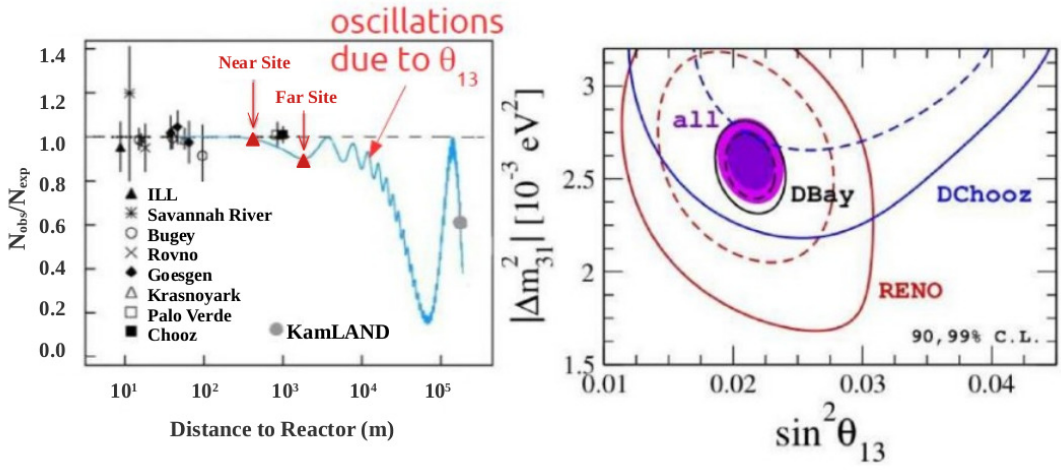

Figure 1.12: On the left, the number of observed electron antineutrinos divided by the number of total antineutrino expected with no oscillations. The main oscillations are due to the Δm^2_{12} term. The superposed oscillations are a second order effect whose amplitude is proportional to $\sin^2 2\theta_{13}$. On the right, 90% and 99% confidence level contours. Credit Daya Bay.

The experiment that firstly measured the θ_{13} was the Daya Bay experiment, a reactor experiment that was able to measure sub-oscillations due to this mixing angle. The value obtained was $\theta_{13} = (8.44 \pm 0.16)^\circ$. The results are shown in Fig. 1.12.

1.5 Unresolved questions

The knowledge on neutrino oscillations as presented by NuFit in 2021 is shown in Tab. 1.1.

Parameter	value best fit $\pm 1\sigma$
θ_{12}	$(33.44^{+0.77}_{-0.74})^\circ$
Δm^2_{12}	$7.42^{+0.21}_{-0.20} \times 10^{-5}$ eV^2
θ_{23}	$(49.2^{+1.0}_{-1.3})^\circ$
$\lvert\Delta m^2_{23}\rvert$	$2.515^{+0.028}_{-0.028} \times 10^{-3}$ eV^2
θ_{13}	$(8.57^{+0.13}_{-0.12})^\circ$
δ_{CP}	$(194^{+52}_{-25})^\circ$

Table 1.1: Three-flavor oscillation parameters from NuFit fit global data in 2021 [11].

Even if past experiment gave some important results, there are still three open problems: the determination of the neutrino mass ordering, i.e. to measure the sign of Δm^2_{23}; the precise measurements of the CP violation phase and of the θ_{23} octant of neutrino mixing matrix, i.e. to measure if the value of this mixing angle is maximal or not.

1.5.1 CP violation phase measurements

If $U \neq U^*$, where U is the PMNS matrix, the CP symmetry is violated. There are 14 general conditions that must be met for the CP violation: charged leptons and neutrinos must not be degenerate in mass (6 conditions), the mixing angles must not be equal to 0 or $\frac{\pi}{2}$ (6 conditions), the δ_{CP} phase must be different from 0 or π (2 conditions).

However, if the matrix $C = -i[M'^{\nu} M'^{\nu\dagger}, M'^{l} M'^{l\dagger}]$ is defined, it is possible to express the previous 14 conditions with just the condition $\det C \neq 0$, which becomes

$$-2J(m^2_{\nu 2} - m^2_{\nu 1})(m^2_{\nu 3} - m^2_{\nu 1})(m^2_{\nu 3} - m^2_{\nu 2})(m^2_{\mu} - m^2_{e})(m^2_{\tau} - m^2_{e})(m^2_{\tau} - m^2_{\mu}) \neq 0, \quad (1.39)$$

where $J = \mathrm{Im}[U_{e2} U^*_{e3} U^*_{\mu 2} U_{\mu 3}]$ is the Jarlskog invariant, useful to measure CP violation in a way independent from the parametrization. Using the standard parametrization, it becomes

$$J = \frac{1}{6} \sin 2\theta_{12} \sin 2\theta_{23} \sin 2\theta_{13} \cos\theta_{13} \sin\delta_{CP}. \quad (1.40)$$

δ_{CP} can be measured only by accelerator based long baseline experiments, therefore, reactor experiments cannot access this parameter. The measurement consists in looking for a different behaviour between neutrino and anti-neutrino oscillations, but matter effects make the measurements more complicate. If $\delta_{CP} = 0$ or π, there would not be CP violation and $P_{\nu_\mu \to \nu_e}$ would be equal to $P_{\overline{\nu}_\mu \to \overline{\nu}_e}$. If $\delta_{CP} = -\frac{\pi}{2}$, $P_{\nu_\mu \to \nu_e}$ would be enhanced, while $P_{\overline{\nu}_\mu \to \overline{\nu}_e}$ would be suppressed. The opposite would happen in case $\delta_{CP} = \frac{\pi}{2}$. An example of oscillation probability for various values of δ_{CP} is illustrated in Fig. 1.13.

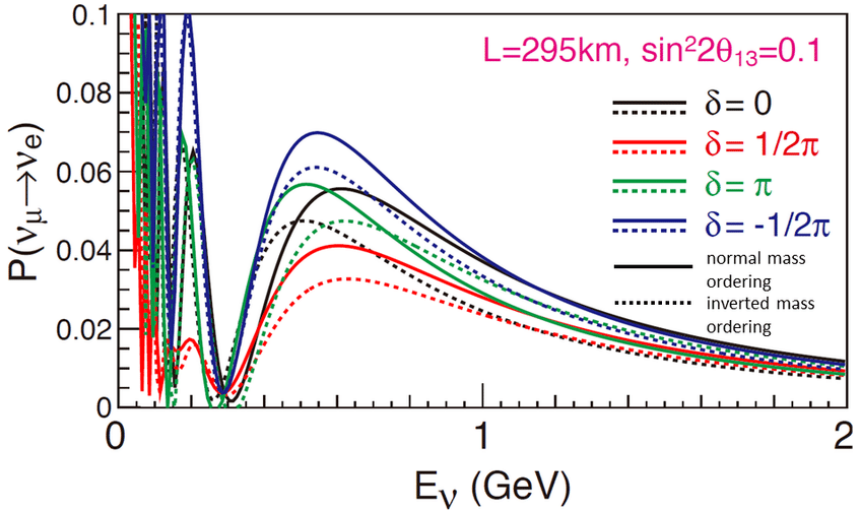

Figure 1.13: $\nu_\mu \to \nu_e$ oscillation probability at T2K as a function of neutrino energy for various values of δ_{CP} and mass ordering. The values of $\sin 2\theta_{23}$ and $\sin 2\theta_{13}$ are fixed to 0.5 and 0.1 respectively [12].

1.5.2 Mass ordering problem

The mass ordering problem is related to the fact that there could be two different ordering for neutrinos' masses depending on whether Δm^2_{13} is positive or negative, as outlined in Fig. 1.14.

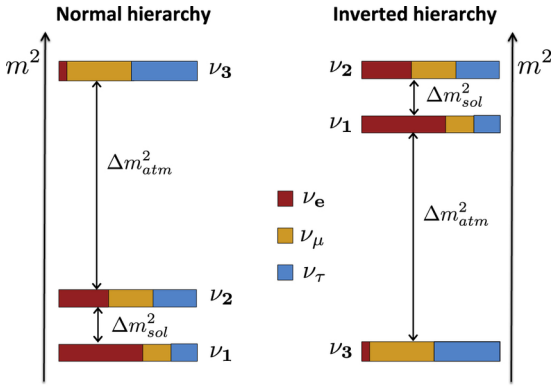

Figure 1.14: Scheme of the two distinct neutrino mass ordering. The colour code indicates the fraction of each flavor $(\nu_e, \nu_\mu, \nu_\tau)$ present in each of the mass eigenstates (ν_1, ν_2, ν_3) [13].

The approaches possible for the solution of the problem is using oscillation interference or the matter effect. Both the solutions are shown in Fig. 1.15. In the first case, the aim is to observe a spectral distortion on medium baseline reactor experiments. For example, JUNO experiment uses this technique. Instead, in the second case, the goal is to measure the sign of Δm^2 using the matter effect: indeed, depending on the mass ordering ν or $\overline{\nu}$ oscillations are enhanced. NOνA, DUNE, HK experiments (will) exploit this approach.

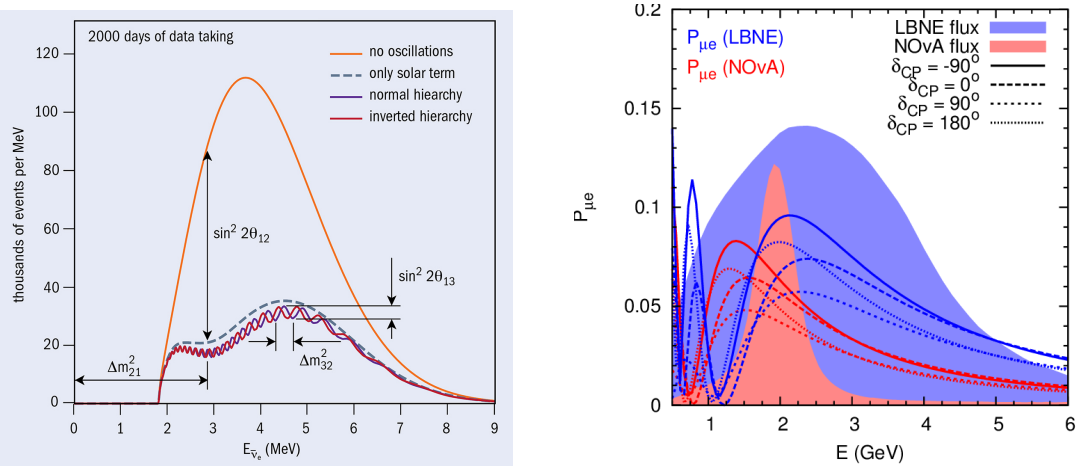

Figure 1.15: On the left, JUNO plans to distinguish the mass ordering through exquisite energy resolution, credit: JUNO. On the right, neutrino oscillation probability $P(\nu_\mu \to \nu_e)$ for various representative values of δ_{CP} and normal ordering, for the NOνA and DUNE baselines [14].

1.5.3 Recent and future experiments

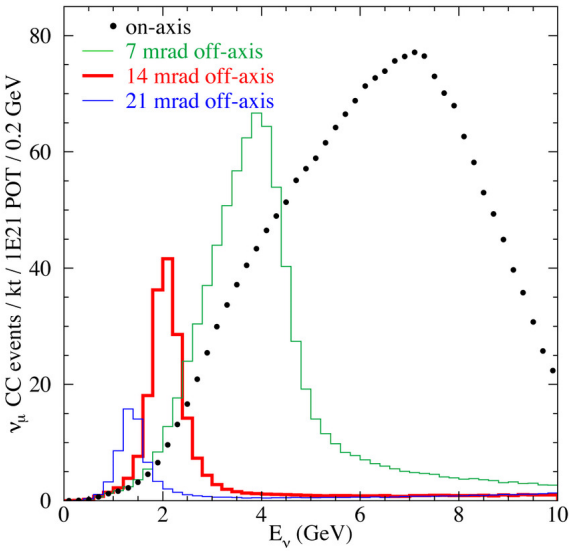

Figure 1.16: The ν_μ CC energy distribution for various off-axis angles for a medium energy tune in NuMI is shown [15].

NOνA and T2K experiments are both off-axis beam experiments, i.e. the beam is off-axis of a small angle with respect the detector. This is made to obtain a well focused neutrino beam, removing the high energy components, as can be observed in Fig. 1.16. In particular, NOνA beam is 14 mrad off-axis, while T2K beam was 43.6 mrad off-axis.

The results for the δ_{CP} value are reported in Fig. 1.17. These experiments were not able to solve the open problems, but were useful to get more precise measurements.

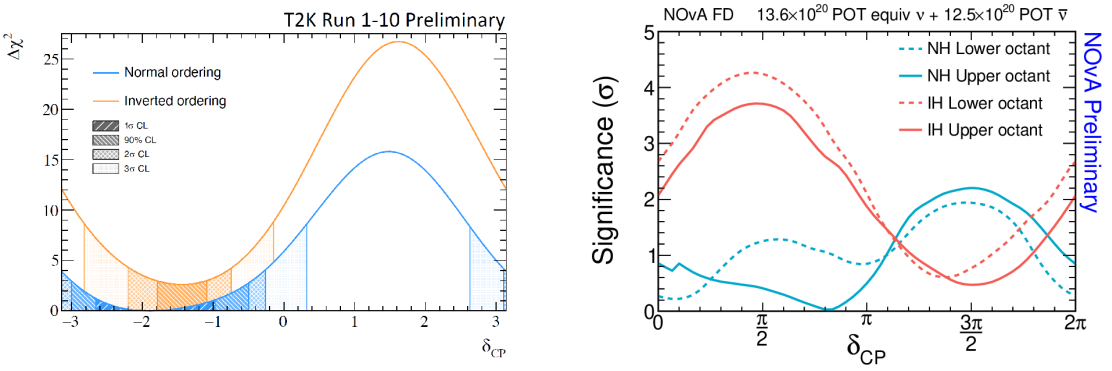

Figure 1.17: The relative preferences for values of δ_{CP} from the most recent oscillation analyses made by T2K on the left and by NOνA on the right [16].

In the future, two experiments are programmed: DUNE (Deep Underground Neutrino Experiment) and HK (Hyper-Kamiokande). DUNE will have the Near Detector at Fermilab and the Far Detector in South Dakota, with a baseline of $\sim$ 1300 km and with a fiducial mass of about 40 kton of LAr. HK will instead be in Japan, near SK location and will use 1 Mton of pure water, with a similar and complementary program w.r.t. DUNE. The significance for both the experiments is shown in Fig. 1.18.

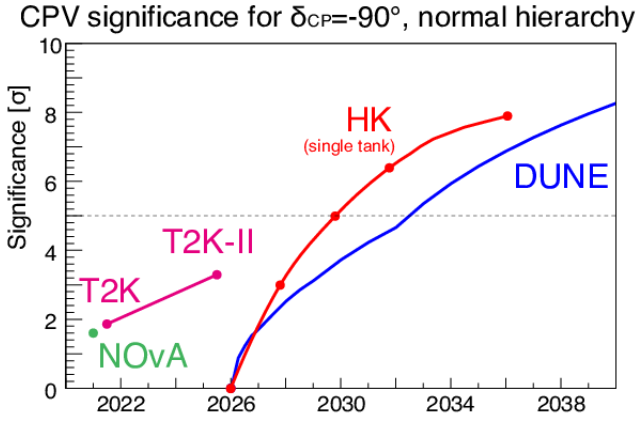

Figure 1.18: The significance for HK and DUNE to measure CP violation for the case where $\delta_{CP} = -\pi/2$. Projections for other experiments are shown for comparison [17].

1.5.4 Majorana mass term

The Dirac field ψ in the Dirac equation $(i\gamma^\mu\partial_\mu - m)\psi = 0$ has four indipendent components. It is possible to perform a chiral decomposition $\psi = \psi_L + \psi_R$. The equations for the chiral components are coupled by the mass

$$i\gamma^\mu\partial_\mu\psi_L = m\psi_R, \tag{1.41}$$
$$i\gamma^\mu\partial_\mu\psi_R = m\psi_L. \tag{1.42}$$

For massless fermions, they are instead decoupled and then can be written as

$$i\gamma^\mu\partial_\mu\psi_L = 0, \tag{1.43}$$
$$i\gamma^\mu\partial_\mu\psi_R = 0, \tag{1.44}$$

which are called Weyl equations. Therefore, a massless fermion can be described using just a single chiral field which has only two indipendent components. These fields are called Weyl spinors.

The possibility to describe a physical particle with a Weyl spinor is possible since parity can be violated. Majorana showed also that a two-component spinor can describe a massive fermion if the two chiral fields are not independent. Neutrinos can then be described by Majorana spinors, with only two indipendent components. The relation that has to hold is $\nu_R = \nu_L^C = C\overline{\nu}_l^T$, where the charge conjugation matrix satisfies $C\gamma_\mu^T C^{-1} = -\gamma_\mu$.

The Majorana equation can then be written as $i\gamma^\mu\partial_\mu\nu_L = m\nu_L^C$, with a Majorana field $\nu = \nu_L + \nu_R = \nu_L + \nu_L^C$ and then $\nu = \nu^C$, which implies the equality of particle and antiparticle. Therefore, only neutral fermion can be Majorana particles. Indeed, for a Majorana field, the electromagnetic current vanishes identically: $\overline{\nu}\gamma^\mu\nu = 0$.

The Majorana mass term can then be written similarly to the Dirac Lagrangian:

$$\mathcal{L}^M = \overline{\nu}_l i\partial\!\!\!/\nu_L - \frac{m}{2}\left(\overline{\nu}_L^C\nu_L + \overline{\nu}_l\nu_L^C\right). \tag{1.45}$$

Since ν_L has a total lepton quantum number $L = +1$ and ν_L^C has $L = -1$, then the total lepton number is not conserved, since the Majorana Lagrangian allows $\Delta L = \pm 2$ transitions. This would imply that neutrinoless double beta decays are allowed.

1.5.5 Sterile neutrinos and seesaw mechanism

The most general mass term is the Dirac-Majorana mass term which can be written as

$$\mathcal{L}^{D+M} = \mathcal{L}^D + \mathcal{L}^L + \mathcal{L}^R, \tag{1.46}$$

where $\mathcal{L}^D = -m_D\overline{\nu}_R\nu_L + h.c.$ is the Dirac mass term, $\mathcal{L}^L = \frac{1}{2}m_L\nu_L^T C^\dagger\nu_L + h.c.$ is the left-handed Majorana mass term, which is forbidden in the SM, $\mathcal{L}^R = \frac{1}{2}m_R\nu_R^T C^\dagger\nu_R + h.c.$, which is allowed in the SM.

It is possible to define the left-handed chiral fields vector N_L and the masses matrix M as

$$N_L = \begin{pmatrix}\nu_L \\ \nu_R^C\end{pmatrix} \quad M = \begin{pmatrix}m_L & m_D \\ m_D & m_R\end{pmatrix}. \tag{1.47}$$

The Dirac-Majorana mass term then becomes

$$\mathcal{L}^{D+M} = \frac{1}{2} N_L^T C^\dagger M N_L + h.c., \tag{1.48}$$

which has the same structure as a Majorana mass term. M can subsequently be diagonalized with real $m_k \geq 0$ using

$$n_L = U^\dagger N_L = \begin{pmatrix} \nu_{1L} \\ \nu_{2L}, \end{pmatrix} \quad U^T M U = \begin{pmatrix} m_1 & 0 \\ 0 & m_2 \end{pmatrix}. \tag{1.49}$$

Accordingly, the Lagrangian becomes

$$\mathcal{L}^{D+M} = \frac{1}{2} \sum_{k=1,2} m_k \nu_{kL}^T C^\dagger \nu_{kL} + h.c. = -\frac{1}{2} \sum_{k=1,2} m_k \overline{\nu}_k \nu_k, \tag{1.50}$$

since $\nu_k = \nu_{kL} + \nu_{kL}^C$. The diagonalization is possible since M is real and symmetric and $U = O\rho$ is used, with

$$O = \begin{pmatrix} \cos\theta & \sin\theta \\ -\sin\theta & \cos\theta \end{pmatrix}, \quad \rho = \begin{pmatrix} \rho_1 & 0 \\ 0 & \rho_2 \end{pmatrix}, \quad \rho_k^2 = \pm 1, \tag{1.51}$$

where $\tan 2\theta = \frac{2m_D}{m_R - m_L}$. The initial diagonalized matrix can be written as

$$O^T M O = \begin{pmatrix} m_1' & 0 \\ 0 & m_2' \end{pmatrix}, \tag{1.52}$$

where

$$m_{2,1}' = \frac{1}{2} \left[m_L + m_R \pm \sqrt{(m_L - m_R)^2 + 4m_D^2} \right], \tag{1.53}$$

and then $m_k = \rho_k^2 m_k'$. There can happen some special cases: maximal mixing if $m_L = m_R$, Dirac limit if $m_L = m_R = 0$, pseudo-Dirac neutrinos if $|m_L|, m_R << m_D$ and seesaw mechanism if $m_L = 0$ and $m_D << m_R$.

In the last case, $m_L = 0$ since $\mathcal{L}^L$ is forbidden in SM, $m_D \lesssim v \sim 100\text{GeV}$ is protected by SM symmetries since it is generated by the Higgs mechanism, instead m_R is not protected by SM symmetries, therefore $m_R \sim M_{GUT} >> v$. Consequently, $m_1' \simeq -\frac{m_D^2}{m_R}$ and $m_2' \simeq m_R$. Accordingly, by choosing $\rho_1^2 = -1$ and $\rho_2^2 = +1$, it is possible to write $m_1 \simeq \frac{m_D^2}{m_R}$ and $m_2 \simeq m_R$. This picture would give a natural explanation of the smallness of neutrino masses, since they would be suppressed by sterile neutrinos masses, as the name of the seesaw mechanism suggests. Furthermore, the mixing angle would also be very small: $\tan 2\theta = 2\,\frac{m_D}{m_R} << 1$. In summary, ν_1 would be composed mainly of active ν_L, while ν_2 would be composed mainly of sterile ν_R.

1.6 Absolute neutrino mass

Thanks to neutrino oscillations, it was possible to measure the squared mass differences with good precision. However, the absolute neutrino masses are still undetermined.

The situation is different depending on whether the correct ordering is the normal or inverted one. In case of normal ordering, $m_2^2 = m_1^2 + \Delta m_{12}^2$ and $m_3^2 = m_1^2 + \Delta m_{13}^2$ would be distinguished, since Δm_{12}^2 and Δm_{13}^2 have different order of magnitude. While, in case of inverted ordering, $m_1^2 = m_3^2 - \Delta m_{13}^2$ and $m_2^2 = m_1^2 + \Delta m_{12}^2 \simeq m_1^2$ would have almost the same value, since $\Delta m_{12}^2 << \Delta m_{13}^2$. Regardless of the correct ordering, at least two neutrino masses must have a value higher than $\sqrt{\Delta m_{12}^2} \simeq 5 \times 10^{-2}$ eV, due to the fact that the differences of the squared masses are known. These observations are outlined in Fig. 1.19.

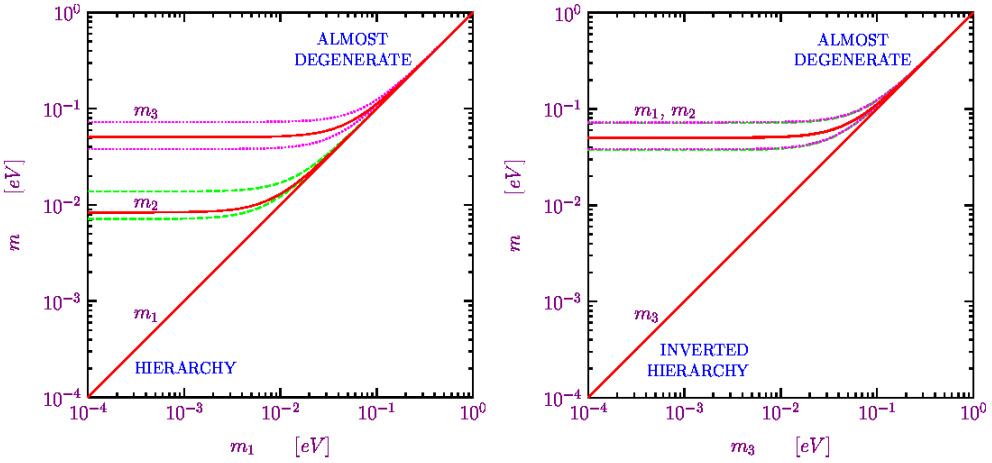

Figure 1.19: Allowed ranges for the neutrino masses as functions of the lightest mass m_1 and m_3 in the normal and inverted three-neutrino scheme, respectively [18].

The methods to access the absolute neutrino mass are three: measurements through decays, neutrino-less double beta decay, cosmology measurements.

1.6.1 Decay measurements

Electron neutrino mass can be measured using the tritium β decay $^3\mathrm{H} \rightarrow {}^3\mathrm{He} + e^- + \overline{\nu}_e$. The Fermi golden rule gives the transition probability for this decay, and its derivative w.r.t. the kinetic energy T is equal to

$$\frac{d\Gamma}{dT} = \frac{(\cos\theta_C\, G_F)^2}{2\pi^3}\, |M|^2\, F(E)\, p\, E\, K^2(T), \tag{1.54}$$

where $K(T)$ is the Kurie function and it can be written as

$$K(T) = \left[(Q-T)\sqrt{(Q-T)^2 - m_{\nu_e}^2}\right]^{1/2}, \tag{1.55}$$

with $Q = M(^3\mathrm{H}) - M(^3\mathrm{He}) - m_e = 18.58\,\mathrm{keV}$. If neutrinos have zero mass, $K(T) = (Q-T)$ is just a straight line, but if $m_{\nu_e} \neq 0$, a deviation is present, which can be used to measure the value of m_{ν_e}. Such deviation can be observed in Fig. 1.20.

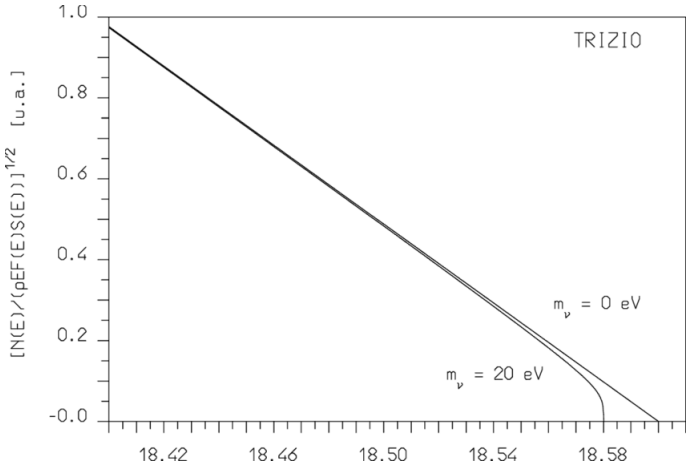

Figure 1.20: Tritium Kurie plot close to the end-point, computed for neutrino masses equal to 0 *and* 20 eV *[19].*

In case of neutrino mixing, the Kurie function becomes

$$K(T) = \left[(Q-T) \sum_k |U_{ek}|^2 \sqrt{(Q-T)^2 - m_k^2} \right]^{1/2} . \tag{1.56}$$

In this case the plot obtained is different, since the parameters are $2N-1$, due to the constrain: $\sum_k |U_{ek}|^2 = 1$. Usually experiments are not so sensitive to neutrino masses since $m_k << Q-T$ and then it is better to consider the effective mass defined as

$$m_\beta^2 = \sum_k |U_{ek}|^2 m_k^2, \tag{1.57}$$

which can be used to rewrite the Kurie function as

$$\begin{aligned} K^2(T) &= (Q-T)^2 \sum_k |U_{ek}|^2 \sqrt{1 - \frac{m_k^2}{(Q-T)^2}} \\ &\simeq (Q-T)^2 \sum_k |U_{ek}|^2 \left[1 - \frac{m_k^2}{2(Q-T)^2} \right] \\ &= (Q-T)^2 \left[1 - \frac{m_\beta^2}{2(Q-T)^2} \right] \\ &\simeq (Q-T) \sqrt{(Q-T)^2 - m_\beta^2}. \end{aligned} \tag{1.58}$$

The modified Kurie plot is shown in Fig. 1.21.

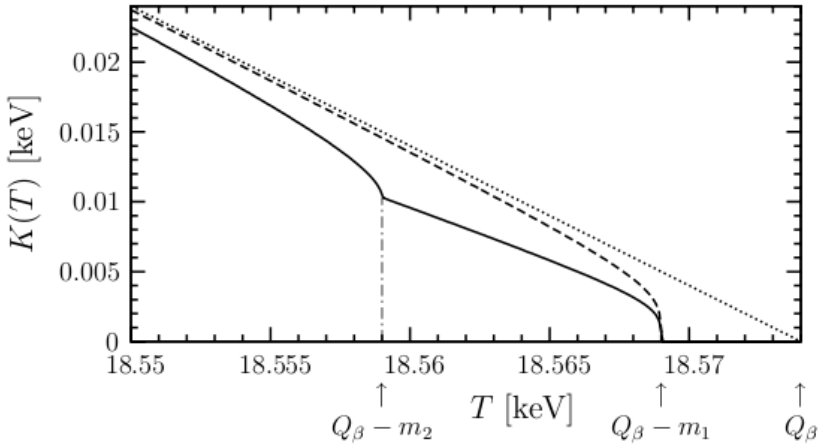

Figure 1.21: Tritium Kurie plot modified by neutrino mixing, provided $m_1 = 5\,\text{eV}$ *and* $m_2 = 15\,\text{eV}$*, with* $\theta = \pi/4$ *[20].*

In the quasi-degenerate case $m_\beta^2 \simeq m_\nu^2$, while in case of inverted ordering $m_\beta^2 \simeq \Delta m_{12}^2 \simeq 7.5 \times 10^{-5}$ eV^2, conversely in case of normal ordering $m_\beta^2 \simeq 8 \times 10^{-5}$ eV^2. In particular, if $m_\beta \lesssim 4 \times 10^{-2}$ eV, the correct ordering would be the normal one. These observations are outlined in Fig. 1.22.

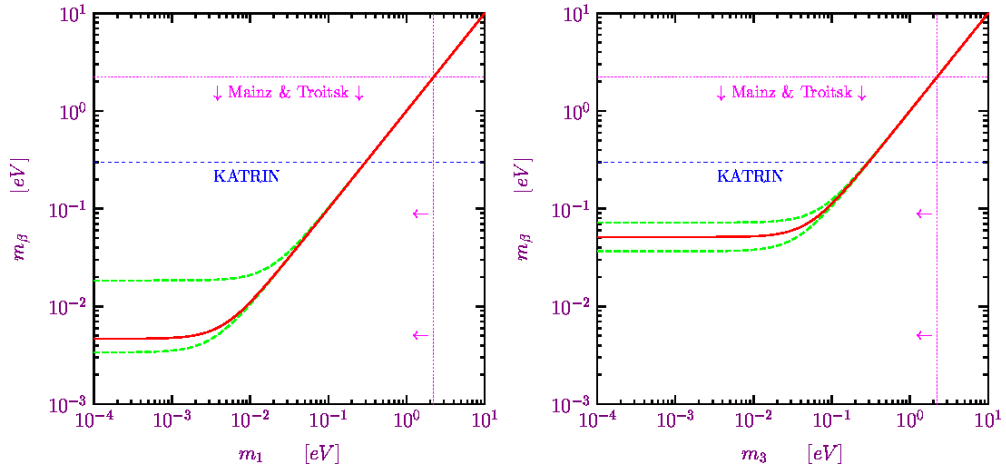

Figure 1.22: Effective neutrino mass m_β *in Tritium beta decay experiments as a function of the lightest mass* m_1 *and* m_3 *in the normal and inverted three-neutrino scheme, respectively [18].*

Experiments need to measure the deviation of the spectrum from the straight line. Therefore it is needed a large number of electrons close to endpoint, a good energy resolution and small energy losses. A recent experiment built to exploit such technique is KATRIN, which used a tritium source and an electron spectrometer. Electrons from beta decays are guided by the magnetic field and the spectrometer perform an adiabatic conversion of the electric field, acting as filter for the electrons. The electron are then counted for different values of the retarding voltage of the spectrometer, in particular around the tritium beta endpoint of 18.58 keV. Currently, the upper limit obtained by KATRIN's measurements is $m_\beta < 0.8$ eV. KATRIN's results are illustrated in Fig. 1.23.

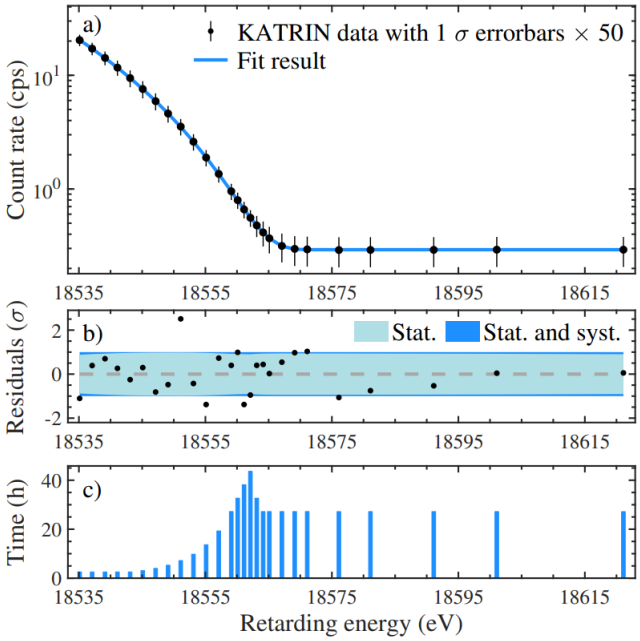

Figure 1.23: In a) the spectrum of electrons over a 90 eV *wide interval from all 274 tritium scans and best-fit model is shown. The integral beta decay spectrum extends up to tritium's endpoint on top of a flat background. Experimental data are displayed with* 1σ *statistical uncertainties enlarged by a factor 50. In b) the residuals relative to the* σ *uncertainty band of the best fit model are shown. In c) the integral measurement time distribution of all 27 HV set points is shown [21].*

1.6.2 Neutrinoless double beta decay

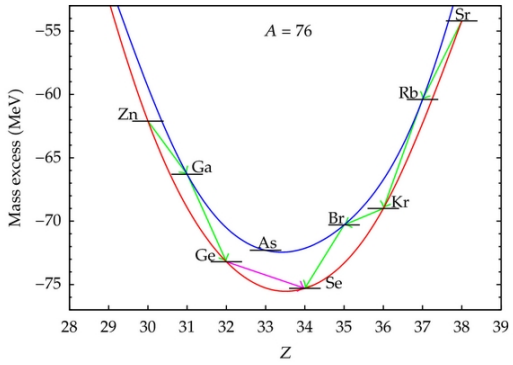

Figure 1.24: Representation of the energies of the $A = 76$ *isobars. The single beta decay between* ^{76}Ge *and* ^{76}Se *is energetically forbidden, hence leaving the double beta as the only decay channel. The two mass parabolas exist because of the pairing interaction that lowers the energy of even Z - even N nuclei with respect to odd Z - odd N nuclei. For odd A nuclei there is a single mass parabola, and all single beta transitions are energetically allowed [22].*

Some nuclei, with even mass number A, cannot undergo β decay, since that would violate the energy conservation principle, but a double β decay could be allowed

$(Z, A) \rightarrow (Z + 2, A) + 2e^- + 2\overline{\nu}_e$, as shown in Fig. 1.24.

Double beta decay rates were studied in detail

$$\Gamma_{2\nu} = \left(T_{1/2,\,2\nu}\right)^{-1} = G_{2\nu}|M_{2\nu}|^2, \tag{1.59}$$

where G is a phase space and M is the nuclear matrix element. Double beta decay is a second order process in perturbation theory and the measured half-lives are in the order of 10^{24} years. Neutrinoless double beta decay is a similar process, but the neutrinos are not present in the final state since they annihilate with each other, as exemplified by the Feynman diagrams in Fig. 1.25.

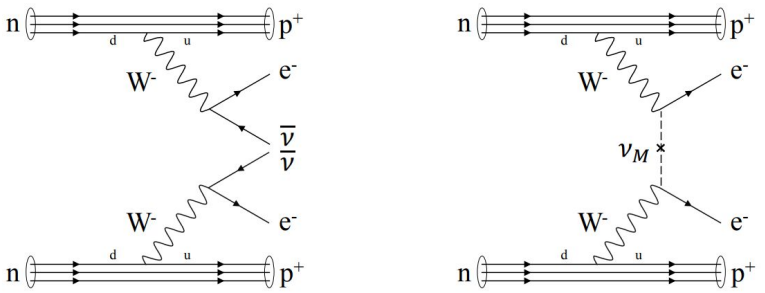

Figure 1.25: Feynman diagrams of the ordinary double beta decay on the left and the neutrinoless double beta decay on the right [23].

In order for this decay to be possible, some requirements have to be satisfied: neutrinos must have mass, neutrinos must be Majorana particles and the lepton number conservation must be violated. The first requirements is satisfied since it is known from oscillations that neutrinos have mass, while the other two are not proven yet, but they are necessary to have an interaction between two neutrinos. In fact the interaction is possible just if one neutrino has a left-handed chiral state and the other has a right-handed chiral state, but both the neutrinos have a left-handed helical state. One can see that observations of neutrinoless double beta decay would be a proof that neutrinos are Majorana particles.

The decay rate of this process would be

$$\Gamma_{0\nu} = \left(T_{1/2,\,0\nu}\right)^{-1} = G_{0\nu}|M_{0\nu}|^2|m_{\beta\beta}|^2, \tag{1.60}$$

with the effective Majorana neutrino mass equal to

$$m_{\beta\beta} = \sum_k |U_{ek}|^2 m_k. \tag{1.61}$$

The corresponding half-life would then be in the order of 10^{27} years. In case the neutrinos are majorana particles, it is not possible to eliminate 5 out of 6 phases of the unitary matrix. Indeed the Majorana mass term

$$\mathcal{L}_M = \frac{1}{2}\sum_{k=1}^{3} m_k \nu_{kL}^T C^\dagger \nu_{kL} \tag{1.62}$$

is not invariant under the global $U(1)$ gauge transformations $\nu_{kL} \to e^{i\phi_k}\nu_{kL}$, and then it is possible just to use the lepton phase transformations $l_\alpha \to e^{i\phi_\alpha} l_\alpha$ to eliminate 3 phases.

Performing these transformations on the weak charged current term it is obtained

$$\begin{aligned} j^{\rho\dagger}_{W,L} &= 2 \sum_{\alpha=e,\mu,\tau} \sum_{k=1}^{3} \bar{l}_{\alpha L} \gamma^\rho U_{\alpha k} \nu_{kL} \\ &= 2 \sum_{\alpha=e,\mu,\tau} \sum_{k=1}^{3} \bar{l}_{\alpha L} e^{-i\phi_\alpha} \gamma^\rho U_{\alpha k} \nu_{kL} \\ &= 2 e^{-i\phi_e} \sum_{\alpha=e,\mu,\tau} \sum_{k=1}^{3} \bar{l}_{\alpha L} e^{-i(\phi_\alpha - \phi_e)} \gamma^\rho U_{\alpha k} \nu_{kL}. \end{aligned} \tag{1.63}$$

It is possible to eliminate 3 phases of the mixing matrix, one overall phase and two phases which can be factorized on the left. Therefore, in the Majorana case there are two additional physical phases w.r.t. the Dirac case, and the mixing matrix becomes $U = U^D D^M$, with U^D the Dirac mixing matrix with just one phase, while

$$D^M = \begin{pmatrix} 1 & 0 & 0 \\ 0 & e^{i\lambda_2} & 0 \\ 0 & 0 & e^{i\lambda_3} \end{pmatrix}. \tag{1.64}$$

The effective Majorana neutrino mass then becomes

$$m_{\beta\beta} = \sum_k |U_{ek}|^2 m_k = |U_{e1}|^2 m_1 + |U_{e2}|^2 e^{i\alpha_2} m_2 + |U_{e3}|^2 e^{i\alpha_3} m_3, \tag{1.65}$$

where $\alpha_2 = 2\lambda_2$ and $\alpha_3 = 2(\lambda_3 - \delta_{CP})$. In the quasi-degenerate case $|m_{\beta\beta}| \simeq m_\nu$, while in case of inverted ordering $|m_{\beta\beta}| \simeq |\Delta m^2_{12}| \simeq 7.5 \times 10^{-5}\text{eV}^2$, conversely in case of normal ordering $|m_{\beta\beta}| \simeq |2.7 + 1.2e^{i\alpha}| \times 10^{-3}\text{eV}^2$. In particular, if $m_\beta \lesssim 10^{-2}$eV, the correct ordering would be the normal one. These observations are outlined in Fig. 1.26.

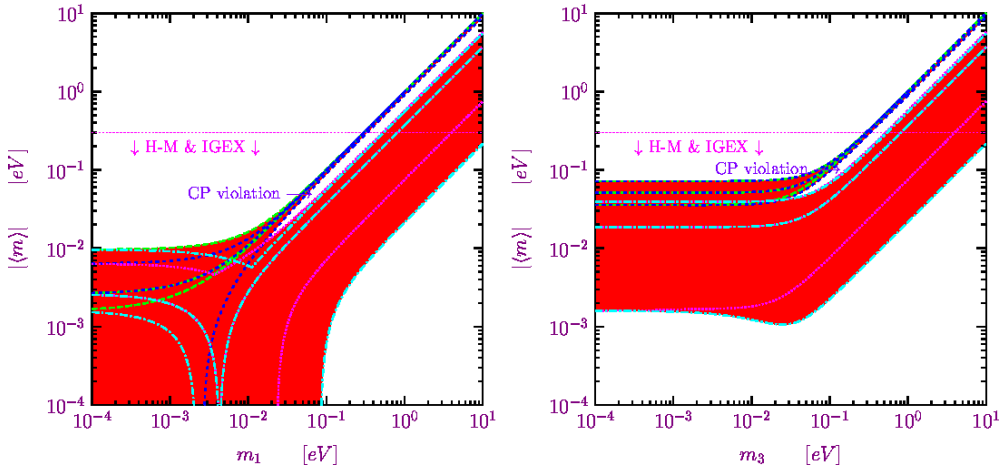

Figure 1.26: Effective Majorana mass $m_{\beta\beta}$ in neutrinoless double beta decay experiments as a function of the lightest mass m_1 and m_3 in the normal and inverted three-neutrino scheme, respectively [18].

Experiments aim to measure the characteristic discrete spectrum, as exemplified in Fig. 1.27. The goal is to estimate the value of the half-life of the $0\nu\beta\beta$ decay, which is proportional to $T_{1/2,\,0\nu} \propto \sqrt{\frac{Mt}{B\Delta E}}$. Therefore, a detector must have large mass, a good energy resolution and an extremely low background.

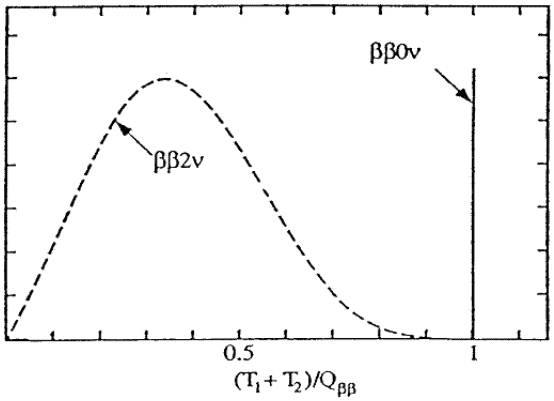

Figure 1.27: Distribution of the sum of the two electron energies for $2\nu\beta\beta$ and $0\nu\beta\beta$.

There are two types of experiments: experiments in which the source is inserted as thin foil inside a tracking detector and the ones in which the detector constitutes also the source. NEMO is an example of the first type of experiments, it used a source of ^{100}Mo that is know to be a $2\nu\beta\beta$ source. The problem of these experiments is that the source material is limited and they have a limited energy resolution. An example of possible tracks is shown in Fig. 1.28.

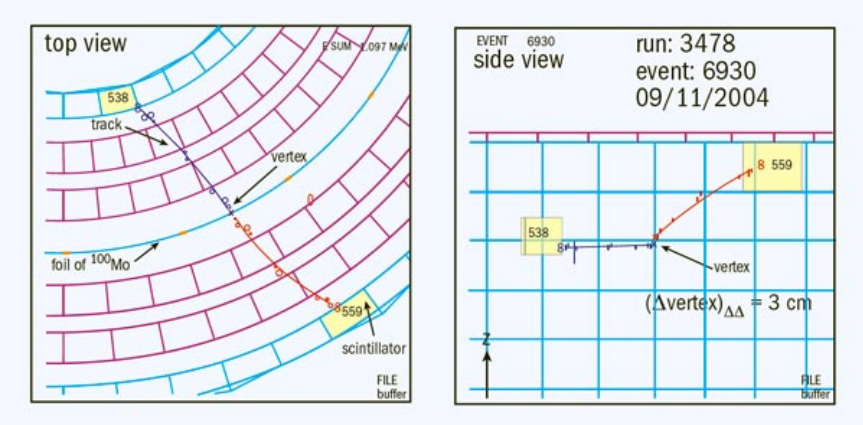

Figure 1.28: Top view and side view of a typical $\beta\beta$ decay event in NEMO-3. The two electrons are emitted from the source foil, the circles correspond to the tracker information, the red curved lines are the fitted tracks and the red rectangles show the hit calorimeter cells, credit NEMO.

Other experiments, which instead exploited the second technique, are CUORE bolometry experiment, HdM, GERDA. All these experiments just gave a lower limit on the half-life of $0\nu\beta\beta$ decay. For example, HdM used germanium and claimed a discovery, but GERDA used the same technique and showed that it was just probably due to some systematic errors. The most recent values are from

KamLAND-Zen collaboration: $T_{1/2,\,0\nu} > 1.1 \times 10^{26}$ years and $m_{\beta\beta} < (0.06 - 0.16)$ eV, the uncertainty on the upper limit for the effective mass is due to nuclear structure effects which cause variations in the nuclear matrix elements.

1.6.3 Cosmology constraints

Neutrino masses different from zero can affect large scale structures in cosmology. These structures are constrained by CMB measurements performed by Planck mission. Massive neutrinos are difficult to cluster because of their relatively high velocities, since they suppress matter fluctuations on scales smaller than their free-streaming scale. From the cosmology constraints, the sum of the neutrino masses has to be smaller than 0.12 eV (95%, Planck TT, TE, EE + low E + lensing + BAO), as displayed in Fig. 1.29.

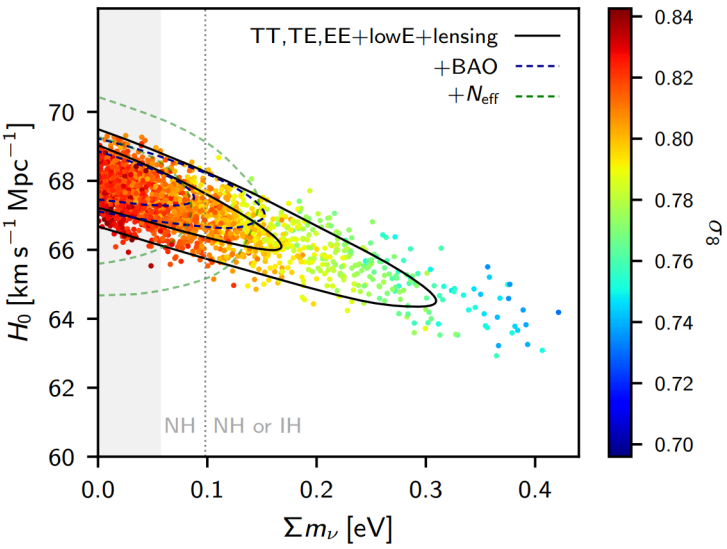

Figure 1.29: Samples from Planck TT, TE, EE + low E chains in the $\sum m_\nu$ - H_0 plane. Solid black contours show the constraints from Planck TT, TE, EE + low E + lensing, while dashed blue lines show the joint constraint from Planck TT, TE, EE + low E + lensing + BAO, and the dashed green lines additionally marginalize over N_{eff}. The grey band on the left shows the region with $\sum m_\nu < 0.056$ eV ruled out by neutrino oscillation experiments. Mass splittings observed in neutrino oscillation experiments also imply that the region left of the dotted vertical line can only be a normal ordering, while the region to the right could be either the normal ordering or an inverted ordering [24].

Baryogenesis through Leptogenesis

Matter dominates over antimatter in the universe, despite standard cosmology predicts that the number of baryons and antibaryons produced in the Big Bag were the same. Modern physics wants to address this apparent contradiction.

Sakharov proposed three conditions which have to be satisfied to produce more matter than antimatter. These conditions are: baryon number violation, C and CP violation, interaction out of thermal equilibrium. Certainly, the first condition is necessary to produce a different number of baryons and antibaryons. C violation is needed, since otherwise interactions which produce more particles than

antiparticles would be compensated by an opposite interaction. CP violation is necessary to produce a different number of left-handed baryons and right-handed anti-baryons, and also of left-handed anti-baryons and right-handed baryons. The last condition is due to the fact that otherwise CPT symmetry would balance the processes that could modify baryons and antibaryons numbers.

CP violation was measured in the quark sector, but it is not sufficient to generate the observed matter-antimatter asymmetry. A possible solution can be considering leptogenesis as a consequence of the seesaw mechanism. In the early universe, H^+ and H^- were physical particles, while today there is only one neutral standard model Higgs particle. In the early universe's conditions, heavy neutrinos could be produced, decaying into Higgs particles. However, phases in the Yukawa coupling matrix would have led to inequality in decay rates: $\Gamma\left(N \to l^- + H^+\right) \neq \Gamma\left(N \to l^+ + H^-\right)$ and $\Gamma\left(N \to v + H^0\right) \neq \Gamma\left(N \to \overline{v} + \overline{H}^0\right)$, causing both C and CP violation.

Even with the lepton number conserved at the beginning of the universe, the considered decays could have produced a lepton number violation. Subsequently, it is possible to consider the standard model sphaleron process, which does not conserved neither the baryon number or the lepton number singularly, but just their difference $B - L$. This process could have started to act after the universe has cooled down at electroweak scale, i.e. 250 GeV. Therefore, starting from an initial state with baryon number conservation and lepton number violation, this process produced a violation also in the baryon number, conserving just $B - L$. Furthermore, it is possible to estimate the value of the coupling y using the seesaw relation for the light neutrino mass:

$$m_\nu \sim \frac{v^2 y^2}{M_N}. \tag{1.66}$$

From this relation, it is obtained a lower limit for the heavy neutrino mass: $M_N \geq 10^9$ GeV [2], considering the measurements of light neutrinos masses and assuming a value $y^2 \sim 10^{-5}$, which would explain the observed cosmic baryon asymmetry.

Chapter 2

DUNE experiment

2.1 DUNE program

The Deep Underground Neutrino Experiment (DUNE) is a long-baseline neutrino oscillation experiment, that together with the Hyper-Kamiokande (HK), will represent the next generation of neutrino experiments [25]. DUNE will consist of two neutrino detectors and will use the neutrino beam with the highest intensity in the world. The Long-Baseline Neutrino Facility will provide the neutrino beamline and the infrastructures for the detectors, which overview can be seen in Fig. 2.1.

The Near Detector will be used to monitor the beam status at the source with high precision and will be placed at the Fermi National Accelerator Laboratory in Batavia, Illinois. While, the Far Detector is much larger w.r.t. the near one and will be positioned deep underground at the Sanford Undergound Research Facility (SURF) in Lead, South Dakota, 1300 km away from the source. The Far Detector is designed to be a massive liquid argon time-projection chamber (LArTPC).

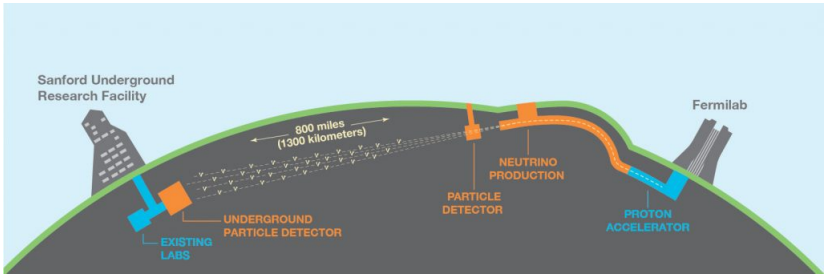

Figure 2.1: Overview of DUNE experiment [25].

DUNE experiment has the goal to address some still open questions of neutrino physics. First, DUNE will try to determine the correct neutrino mass ordering, using the matter effect to find the sign of Δm^2_{13}. Furthermore, the observation of the CP violation and the measure of δ_{CP} are expected. CP violation in leptonic sector is really compelling since it could explain the origin of the matter-antimatter asymmetry in the Universe. In fact, matter dominates over antimatter, despite being equally created in the Big Bang. DUNE will also perform precision measurement of the $\nu_\mu \rightarrow \nu_e$ oscillation parameters, studying also atmospheric neutrinos, in particular trying to solve the octant problem of θ_{23}.

Another questions that DUNE tries to probe is the validity of Grand Unified Theories (GUTs), according to which the fundamental forces were all unified in just one force. Since these theories predict the possibility of proton decay, DUNE will search for these events, improving the lower limit value for the proton's lifetime. Furthermore, DUNE will be capable of measuring neutrino fluxes coming from core collapse supernovae. This will allow the study of the evolution of astrophysical phenomenon. In addition, DUNE will search for active sterile neutrino mixing, light dark mass candidates and heavy neutral leptons.

2.1.1 CP violation measurements and mass ordering determination

As aforementioned, DUNE aims to measure the value of the CP violation phase parameter. This value could help to solve the matter-antimatter asymmetry problem. Another goal is to determine the correct neutrino mass ordering, measuring the difference between neutrinos squared masses through the matter effect [26].

Both the CP violation phase and the matter effect term can be measured considering higher order transition probabilities

$$\begin{aligned} P\left(\overset{(-)}{\nu}_\mu \to \overset{(-)}{\nu}_e\right) \approx & \sin^2\theta_{23}\sin^2 2\theta_{13}\frac{\sin^2(\Delta_{13}-aL)}{(\Delta_{13}-aL)^2}\Delta_{13}^2 \\ & + \sin 2\theta_{23}\sin 2\theta_{13}\sin 2\theta_{12}\frac{\sin(\Delta_{13}-aL)}{\Delta_{13}-aL}\Delta_{13}\frac{\sin(aL)}{aL}\Delta_{12}\cos(\Delta_{13}\pm\delta_{CP}) \\ & + \cos^2\theta_{23}\sin^2 2\theta_{12}\frac{\sin^2(aL)}{(aL)^2}\Delta_{12}^2. \end{aligned} \tag{2.1}$$

Here, $\Delta_{ij} = 1.27\,\Delta m^2_{ij} L/E_\nu$, while a is the matter effect term, defined as

$$a = \pm\frac{G_F N_e}{\sqrt{2}} \approx \pm\frac{1}{3500\,\text{km}}\left(\frac{\rho}{3.0\,\text{g/cm}^3}\right), \tag{2.2}$$

where G_F is the Fermi constant, N_e is the number density of electrons in the Earth's crust. In neutrinos case, both δ_{CP} and a are positive, while in antineutrinos case, they are negative. Even in case $\delta_{CP} = 0$ and thus CP is conserved, the asymmetry in the oscillation of neutrinos and antineutrinos would be measured nevertheless. Indeed, their interactions rate would be different, since electrons are present in the Earth's crust, while positrons not. DUNE will be more sensitive to the matter effect term a than T2K and NOνA, since it enters quadratically in the measured oscillation probability. Both the CP violation and the matter effect can enhance either neutrinos or antineutrinos oscillation probabilities. In Fig. 2.2, the appearance probability at a baseline of 1300 km, as the one of DUNE, in function of neutrino energy is shown for different values of δ_{CP}, for both neutrinos and antineutrinos, in case of true normal ordering.

The physics program of DUNE foresees that after 3.5 years in neutrino-beam mode and 3.5 years in antineutrino-beam mode, the expected number of events will be ~ 1000 $\nu_e/\overline{\nu}_e$ and ~ 10000 $\nu_\mu/\overline{\nu}_\mu$ in 7 years.

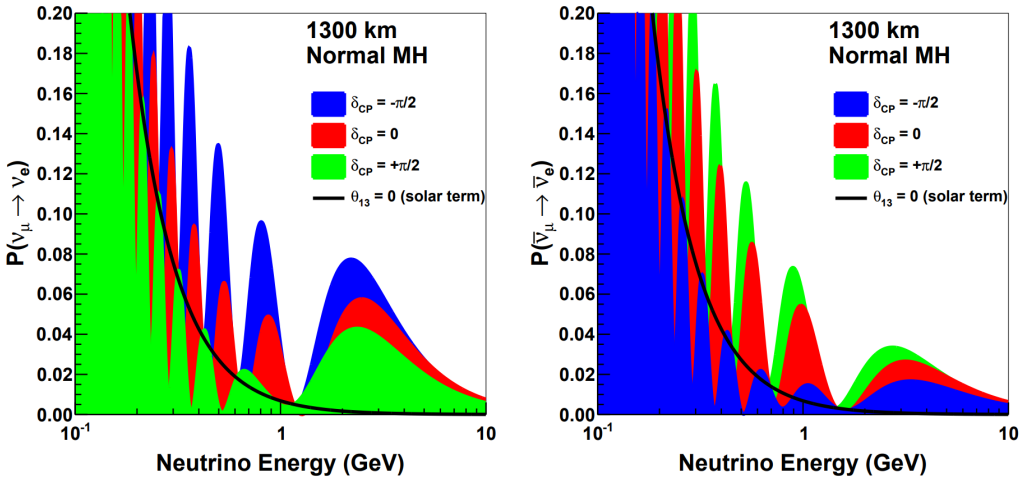

Figure 2.2: Appearance probability at a baseline of 1300 km*, as a function of neutrino energy, for $\delta_{CP} = -\pi/2$ (blue), 0 (red), $\pi/2$ (green), for neutrinos (left) and antineutrinos (right), for normal ordering. The black line shows the oscillation probability if θ_{13} were equal to zero [26].*

As introduced in Sec. 1.5.1, the CP violation parameter enters in the definition of the Jarlskog invariant. Especially, if the standard parametrization of the PMNS is choosen, it can be written as follows:

$$J = \frac{1}{6} \sin 2\theta_{12} \sin 2\theta_{23} \sin 2\theta_{13} \cos\theta_{13} \sin\delta_{CP} \tag{2.3}$$

$$\approx 0.03 \ \sin\delta_{CP}, \tag{2.4}$$

which was obtained by considering the current best-fit values of the mixing angles and assuming the normal ordering. CP violation would be confirmed if the Jarlskog invariant is different from zero and then if $\delta_{CP} \neq 0, \pi$. The obtained value for the neutrino sector Jarlskog invariant, could be higher than the one for the quark sector, which is $J \approx 3 \times 10^{-5}$.

The measure of the CP term is done through the asymmetry term defined as

$$\begin{aligned} \mathcal{A} &= \frac{P(\nu_\mu \to \nu_e) - P(\overline{\nu}_\mu \to \overline{\nu}_e)}{P(\nu_\mu \to \nu_e) + P(\overline{\nu}_\mu \to \overline{\nu}_e)} \\ &\approx \frac{\cos\theta_{23} \sin 2\theta_{12} \sin\delta_{CP}}{\sin\theta_{23} \sin\theta_{13}} \Delta_{12} + \mathcal{A}_{matter} \\ &= \mathcal{A}_\delta + \mathcal{A}_{matter}. \end{aligned} \tag{2.5}$$

The asymmetry term has be written as sum of two asymmetries due to CP violation and matter effects, which behaves respectively as $\mathcal{A}_\delta \sim L/E$ and $\mathcal{A}_{matter} \sim L \times E$.

The degeneracy between the two asymmetries can be resolved for baselines longer than 1200 km. In fact, for an energy range of few GeV, $\mathcal{A}_{matter}$ increases with the baseline L, since the neutrino pass through more matter. The higher the baseline, the higher the sensitivity to the mass ordering. Then, for these baseline values, knowing the value of $|\Delta m^2_{13}|$, $\mathcal{A}_{matter}$ suppresses $\mathcal{A}_\delta$, allowing the distinction between normal and inverted ordering.

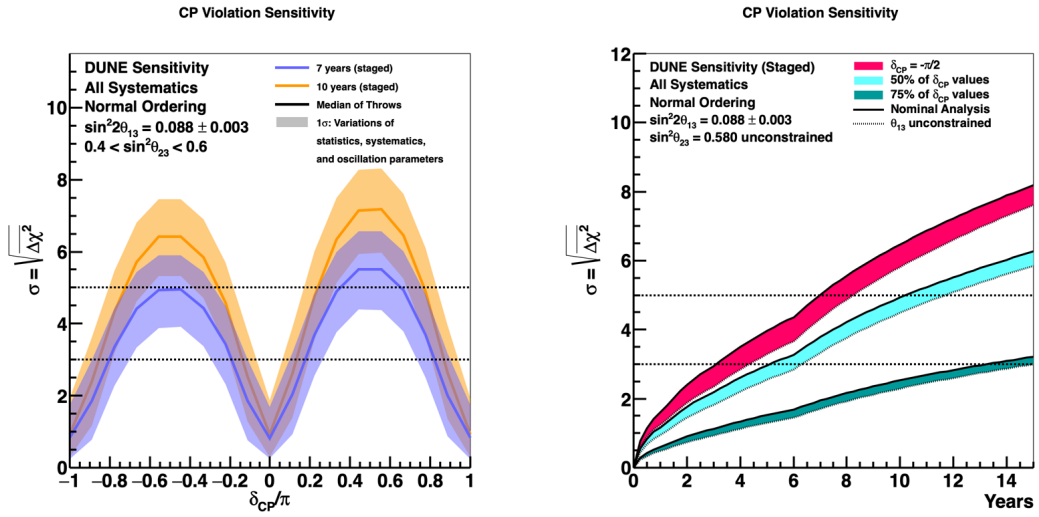

Figure 2.3: On the left, significance of the DUNE determination of CP-violation as a function of the true value of δ_{CP}, for seven (blue) and ten (orange) years of exposure. Normal ordering is assumed. The width of the transparent bands cover 68% of fits. The solid lines represent the median sensitivity. On the right, significance of the DUNE determination of CP-violation for the case when $\delta_{CP} = -\pi/2$, and for 50% and 75% of possible true δ_{CP} values, as a function of time in years. Normal ordering is assumed [26].

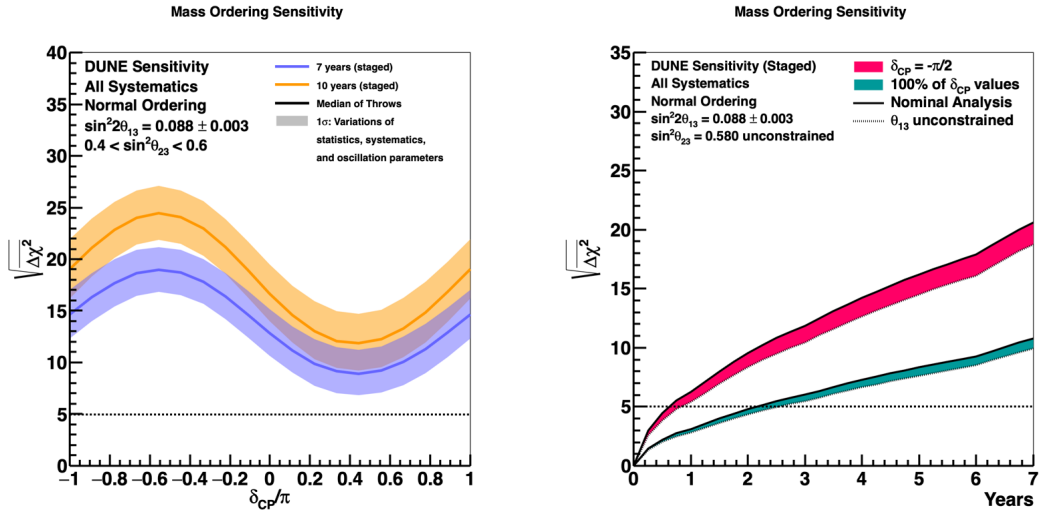

Figure 2.4: On the left, significance of the DUNE determination of the neutrino mass ordering, as a function of the true value of δ_{CP}, for seven (blue) and ten (orange) years of exposure. Normal ordering is assumed. The width of the transparent bands cover 68% of fits. The solid lines represent the median sensitivity. On the right, significance of the DUNE determination of the neutrino mass ordering for the case when $\delta_{CP} = -\pi/2$, and for 100% of possible true δ_{CP} values, as a function of time in years. Normal ordering is assumed [26].

DUNE will be able to determine the neutrino mass ordering and to measure the value of δ_{CP}, since it will have a baseline equal to 1300 km. The significance

of the DUNE determination of CP-violation and of the neutrino mass ordering are shown respectively in Fig. 2.3 and Fig. 2.4, both in function of the true value of δ_{CP} and of time in years, assuming true normal ordering.

2.1.2 Measurement of the octant

Even if DUNE experiment will improve the sensitivity on both $\sin^2\theta_{13}$ and θ_{23}, the octant problem is still open [26]. For example, if $\theta_{23} = 45°$, the mixing between ν_2 and ν_3 would be maximal and ν_μ and ν_τ would have equal contributions from ν_3.

The T2K experiment obtained $\sin^2\theta_{23} = 0.514^{+0.055}_{-0.0056}$ in case of normal ordering, while $\sin^2\theta_{23} = 0.511 \pm 0.055$ in case of inverted ordering, giving therefore the most precise measurement. Measurements of ν_e appearance are sensitive to $\sin^2\theta_{23}$, while the ones of ν_μ disappearance are sensitive to $\sin^2 2\theta_{23}$. Combining both these measurement in a single experiment will allow to determine the value of the θ_{23} octant. Fig. 2.5 shows the sensitivity of DUNE to the determination of the θ_{23} octant as a function of the true value of $\sin^2\theta_{23}$, assuming true normal ordering.

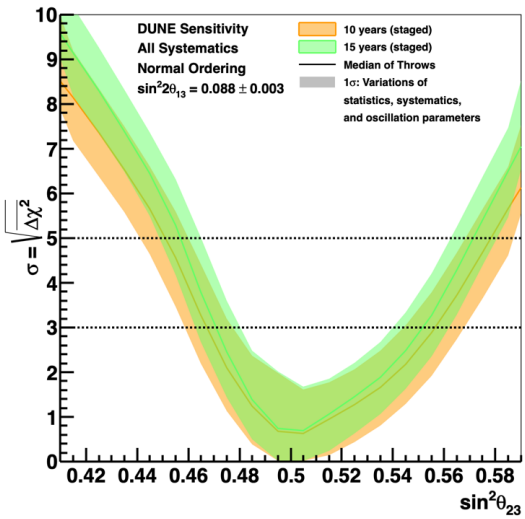

Figure 2.5: Sensitivity to determination of the θ_{23} octant as a function of the true value of $\sin^2\theta_{23}$, for ten (orange) and fifteen (green) years of exposure. Normal ordering is assumed. The width of the transparent bands cover 68% of fits. The solid lines represent the median sensitivity [26].

The mixing angle θ_{13} is instead expected to be measured in few years by reactor experiments with a precision that will be limited by systematic uncertainties. θ_{13} measurements will provide crucial constraints for both the CP violation parameter δ_{CP} and the θ_{23} octant. In addition, DUNE is expected to measure the value of θ_{13} in an independent way w.r.t. reactor experiments, obtaining a similar precision. Reactor experiments measure θ_{13} using electron neutrino disappearance, while DUNE will measure it through electron neutrinos and antineutrinos disappearance. Therefore, DUNE will able to provide an independent constraint on the PMNS neutrino mixing matrix.

2.1.3 Atmospheric neutrinos

DUNE's Far Detector could be exploited to study neutrino oscillations of atmospheric neutrinos, since it has a large mass and it is located deep underground. These kind of measurements would be complementary to the artificial neutrino measurements and it would be possible to measure all the mixing parameters, since the ratio L/E for atmospheric neutrinos can assume a broad range of values [27].

Besides, the sensitivity to mass ordering determination can be described by the square root of the exposure to atmospheric neutrinos. Thus, sensitivity is not limited by the values of the systematic uncertainties. Furthermore, the mass ordering sensitivity using atmospheric neutrinos is practically independent on CP violation, but it depends on the value of $\sin^2 2\theta_{23}$. Hence, atmospheric neutrinos measurements could help to solve the octant problem, putting some additional constraints on θ_{23}.

2.1.4 Proton decay

The proton is a stable particle according to the Standard Model, since it is the lightest baryon and it cannot decay without breaking the baryon number symmetry. On the other hand, some Grand Unified Theories (GUTs) beyond the Standard Model predict the breaking of this symmetry, allowing protons to decay.

DUNE will search for two proton decay modes: $p \to e^+\pi^0$ and $p \to K^+\overline{\nu}$. The former is interesting since it has the highest branching ratio among the predicted decays. The latter can be used specifically in DUNE, since stopping kaons have a higher ionization density than particles with lower masses. Therefore a LArTPC is able to recognize the K^+ track efficiently [27]. Both these decays could happen, but just through new particles beyond the Standard Model, as illustrated in Fig. 2.6.

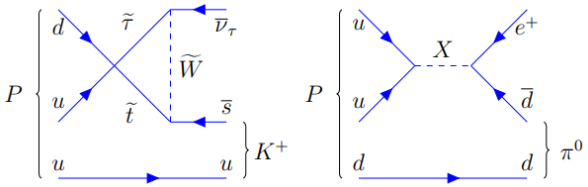

Figure 2.6: Feynman diagrams of proton decay modes according to GUTs.

If proton decay is observed, the lifetime will be measured. While in case of no observations, DUNE will be able to determine just a lower limit for the proton's lifetime. The current limits on proton's lifetime were set by Super–Kamiokande. DUNE's Far Detector will start with an initial fiducial volume of 10 kton and there will be added another 10 kton a year after. With its total fiducial volume, DUNE will improve the current limits by an order of magnitude with 90% C.L., after running for 20 years. Obviously, a larger detector mass would improve the limits even more in the same amount of time.

2.1.5 Supernovae neutrinos

The DUNE experiment will have a wide dynamic range such that it will be sensitive to neutrinos both of high energies on the order of the GeV and just few MeV.

In particular, in the energy regime from around 5 MeV to several tens of MeV, DUNE will be sensitive to the electron neutrino flavor component of the burst of neutrinos from a galactic core-collapse supernova [28].

In fact, in that specific range, the liquid argon present in DUNE' LArTPCs, has a particular sensitivity to the electron neutrino component through the charged current (CC) interaction $\nu_e + {}^{40}\mathrm{Ar} \rightarrow e^- + {}^{40}\mathrm{K}^*$. It is possible to observe a short electron track produced in liquid argon and secondary particles caused by the excited kaon. Elastic scattering between electron neutrino and argon atom is also possible in the mentioned energy regime. In this case an electromagnetic cascade would be observed.

DUNE would be able to contribute to the multi-messenger astronomy, since it would be able to detect supernova neutrinos, together with neutrinos and antineutrinos from other astrophysical sources, e.g. solar and supernova background neutrinos. However, the background and the trigger constitute a challenge, due to the low energy regime of the neutrino events.

Preliminary studies have shown that DUNE's detection efficiency to the entire Milky Way is not limited by the expected background rates due to low energies. In addition there is the possibly of detecting neutrinos from beyond the Milky Way, depending on the neutrino luminosity of the core-collapse supernova. DUNE's energy resolution is expected to be between 10% and 20% in the range between 5 MeV and several tens of MeV.

DUNE is expected to be able to measure the supernova electron neutrino spectral parameters. Furthermore, it will use supernova burst signal to access, for example, to neutrino mass ordering and collective effects. If a measurable supernova event will occur during DUNE experiment's lifetime, it would provide information about the early stages of a core collapse and it could even signal the birth of a black hole.

2.2 DUNE elements

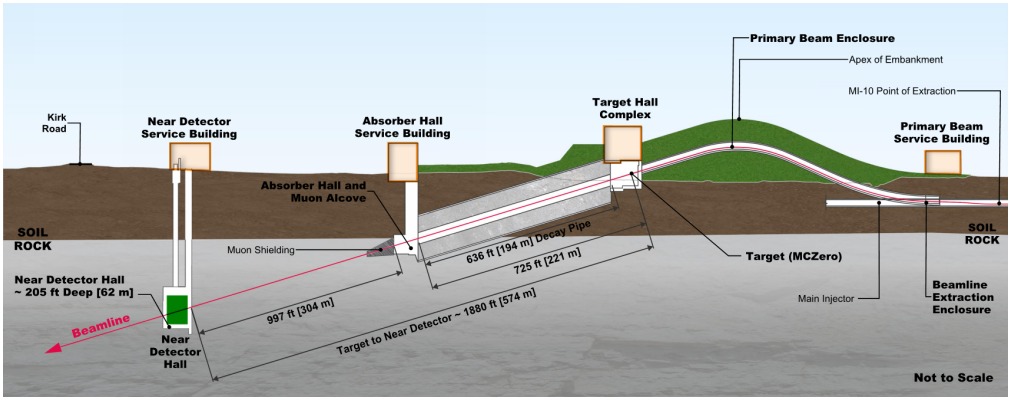

Figure 2.7: Neutrino beamline and DUNE Near Detector hall at Fermilab in Illinois [26].

The Long-Baseline Neutrino Facility (LBNF) will use a high intensity neutrino beam that will travel through both the Near Detector in Illinois, displayed schematically in Fig. 2.7, and the Far Detector in South Dakota.

2.2.1 Neutrino beam

The neutrino beam for the DUNE experiment is produced using a proton beam which collides with a target. The protons have an energy in range between 69 GeV and 120 GeV, while the target is made of graphite and beryllium. In the proton-target interaction, secondary particles are produced, mainly $\pi^{\pm}, K^{\pm}$, which are focused into a decay pipe by two magnetic horns. Inside the pipe, these particles decay mostly into $\mu^{\pm}$ and $\overset{(-)}{\nu}_{\mu}$. At the end of the pipe, an absorber removes the hadrons, leaving just the neutrinos. The magnetic horns can be polarized to focus only negative or positive particles. Therefore, it is possible to obtain a high purity ν_{μ} or $\overline{\nu}_{\mu}$ beam with just a small contamination of the respective anti-neutrino and of $\overset{(-)}{\nu}_{e}$. It is of primary importance to know the beam composition and contamination, since the measurements depend on it. The expected neutrino fluxes at the FD are shown in Fig. 2.8.

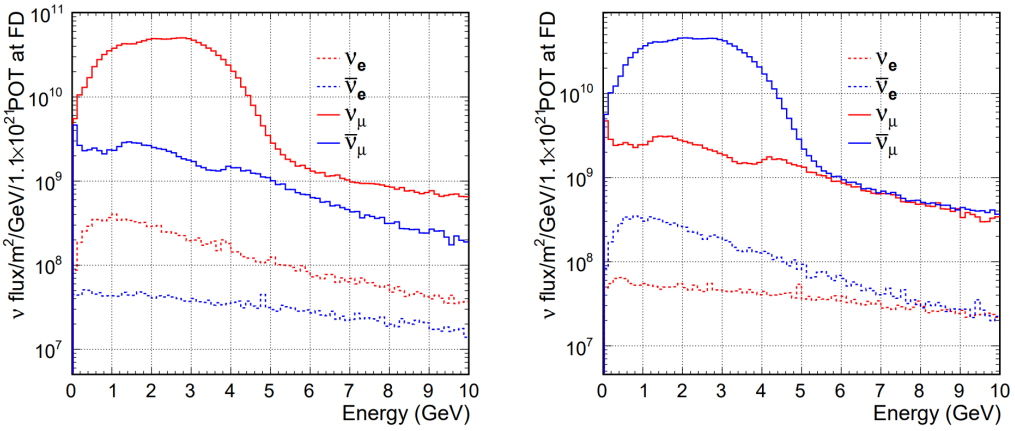

Figure 2.8: Neutrino fluxes at the FD for neutrino mode (left) and antineutrino mode (right) [26].

2.2.2 Far Detector

The DUNE Far Detector will be installed 1500 km underground at the SURF in South Dakota. The Far Detector will initially consist of two Liquid Argon Time Projection Chamber (LArTPC) detector modules with a fiducial volume of 10 kton each. Each of the LArTPCs will be put inside a cryostat that contains a total LAr mass of about 17.5 kton, which will be used as target for neutrino interactions. The scheme of the FD is illustrated in Fig. 2.9. The Single Phase (SP) LArTPC technology will be used. A prototype detector was assembled at CERN, to test the SP technology. This prototype called ProtoDUNE-SP is smaller w.r.t. future DUNE detectors, but use the same components. The conducted tests have shown good performances of such prototype.

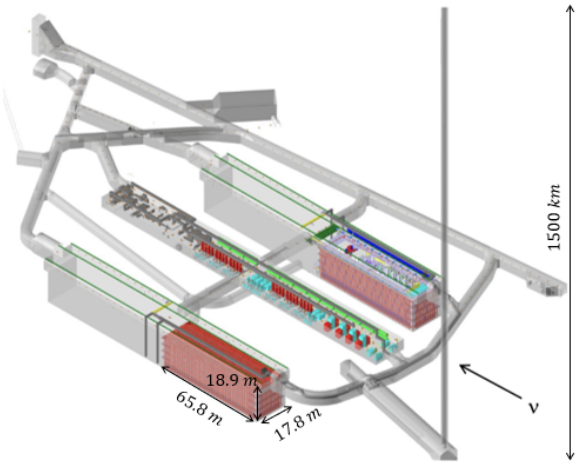

Figure 2.9: Underground caverns for DUNE FD and cryogenics systems at SURF, in South Dakota. The scheme shows the first two Far Detector modules in place [26].

Liquid argon

Liquid argon (LAr) will occupy the detector volume and will constitute the target for neutrino interactions.

The passage of ionizing particles in argon can produce excitation and ionization of atoms. Indeed, if the energy released in the interaction is smaller than the ionization energy, the atom will be excited, while if the energy is high enough, the atom will be ionized. Excited atoms form excited molecular states Ar_2^*. Instead, ionized atoms form excited molecular states Ar_2^+, which eventually recombine with electrons, producing Ar_2^* states, which then decays emitting scintillation light, as it is shown in Fig. 2.10.

The two lowest allowed radiative decays are the ones from the singlet ($^1\Sigma_u^+$) and the triplet ($^3\Sigma_u^+$) states to the ground state ($^1\Sigma_g^+$), which happen with different decay times, with a respective value of $\tau_1 \simeq 5\,\text{ns}$ and $\tau_2 \simeq 1.6\,\mu\text{s}$ [29].

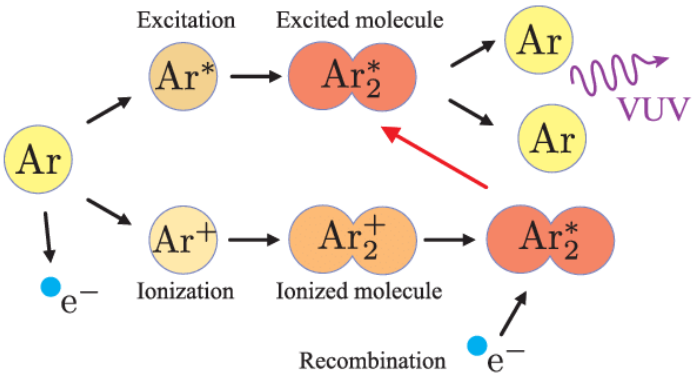

Figure 2.10: Scintillation and ionization in argon [29].

The emission spectrum for those transitions has a narrow peak at 126.8 nm [30], hence photons are produced in the Vacuum Ultra Violet (VUV) band. It is important to consider the wavelength range while designing the detector, since

there are some technical problems, such as the transparency of the scintillator medium to these wavelengths and the sensitivity of the photosensors. Fortunately, reabsorption cannot occur if the argon is pure, because the energy of the single atomic excited state is too high.

Another remark that has to be taken into consideration is the presence of impurities. Impurities can absorb ionization electrons or quench emitted scintillation light. For example, electronegative atoms, such as oxygen, could absorb electrons. That is the reason why the requested impurities are less than 100 parts per trillions, to have an electron lifetime larger than 3 ms at 500 V/cm. Instead, impurities such as nitrogen can quench the emitted scintillation photons. In this case it is requested an impurity smaller than 25 parts per million, to ensure the detection of at least 0.5 photo-electron per MeV for event. Therefore, a purification mechanism to introduce new argon will be implemented.

Photon detection

A photon detection system has to be used to collect the scintillation light emitted at 126.8 nm by charged particles traversing liquid argon (LAr). Since these photons are in the VUV range, it is necessary to use a wavelength shifter, to convert the photons to a different wavelength at which photo-sensors are sensitive. Indeed, available photo-sensors have a low photon detection efficiency for VUV wavelength photons. SiPMs (Silicon Photo-Multipliers) are used as photo-sensor to convert the light into an electric signal. SiPMs were chosen since they can be very small and they allow a good light collection efficiency, without reducing significantly the active volume of LAr. Indeed, photon detection modules are placed in the inactive space between wire planes, to have no impact on fiducial volume.

The ARAPUCA is a light trap which captures wavelength shifted light inside highly reflective boxes. A more advanced device, the X-ARAPUCA, is being considered as one of the possible alternatives for DUNE's photon detection modules. Its working principle is shown in Fig. 2.11. X-ARAPUCA design makes use of total internal reflection to capture wavelength shifted photons to further improve photon detection efficiency [31].

A photon detection module includes four X-ARAPUCA cells. Both ARAPUCA and X-ARAPUCA cells are composed of various layers: a wavelength shifter material, which covers a dichroic filter plate that traps the light. In this way the photon remains inside the cell's volume. Inside the box, the photons are taken to the photo-sensors by a wave lenght shifter light guide, using total internal reflection. The refractive indexes are chosen to minimize the reflections and reduce the probability to loose photons, increasing the photon detection efficiency.

The first X-ARAPUCA prototype has an acceptance window of dimension 8×10 cm^2 made by a dichroic filter with a cutoff of 400 nm. This window is coated with pTP (p-Terphenyl) on the side which is exposed. The prototype's lightguide posses the same dimensions of the window and is made by acrylic doped with TPB (TetraPhenyl-Butadiene), with an emission wavelength spectrum centered around 430 nm. Finally, the bottom layer is constituted by a high-pressure fiberglass laminate called G10. Over this plane, a high reflective foil Enhanced Specular Reflector (ESR) is placed. For what regards the photosensors, there will

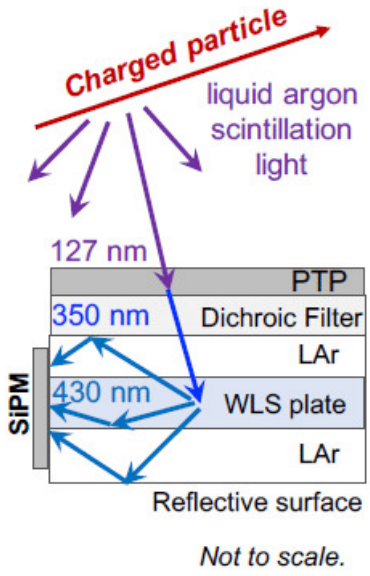

Figure 2.11: Working principle of an X-ARAPUCA cell [32].

be used cryogenic SiPMs, with an active area of $6 \times 6\,\mathrm{mm}^2$ each, as the ones used for the ProtoDUNE detector. Just half of the active area of the SiPMs will collect the photons directly from the acceptance window. The other half will collect photons reflected by the rest of the cell. On the opposite sides of the photon detection module are settled 6 SiPMs each and are mounted on photosensor PCBs (Printed Circuit Boards).

To summarize, each X-ARAPUCA cell will use eight PCBs, therefore there will be 48 SiPMs for each cell and 192 SiPMs for each photon detection module. SiPMs on a PCB are connected in parallel to reduce the number of necessary readout channels, obtaining just four channels for each photon detection module. Approximately 300,000 SiPMs will be used for the DUNE's Far Detector. These SiPMs will be immersed in LAr and will work in a cryogenic environment. Hence, it is of utter importance to test the mechanical and electrical parameters when subjected to these conditions.

Single phase LArTPC

As aforementioned, liquid argon (LAr) atoms can be excited or ionized by charged particles produced by neutrino interactions. In a single phase (SP) time projection chamber (TPC), an electric field is used to drift the free ionized electrons to the anode plates, where the charge is collected [34]. The scheme of a SP module is displayed in Fig. 2.12.

The ionization charges drift horizontally for few meters and the maximum path is 3.5 m. The APA (Anode Planes Assembly) is used to catch the charge produced by ionization drifting in the TPC volume. The anode wall is composed of 50 APAs. Three instrumented and two unistrumented anode layers are present on each side of the APA's metal frame. Three complementary views of the ionization in the

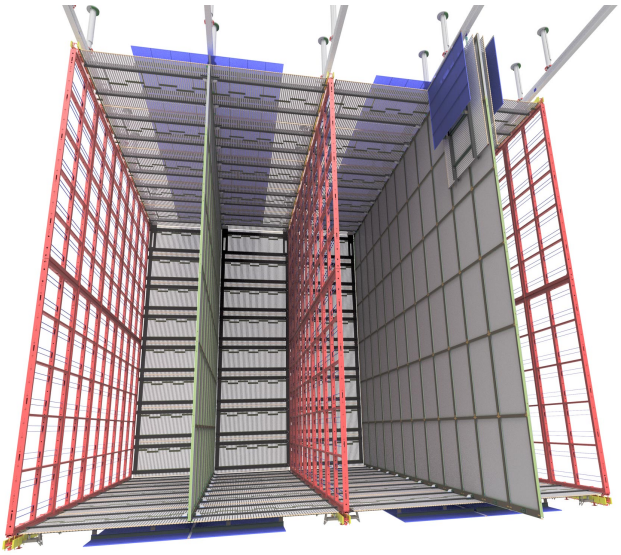

Figure 2.12: Schematic of a 10 kt DUNE FD SP module, showing the alternating anode and cathode planes that divide the LArTPC into four separate drift volumes [26].

TPC are available. These views can be combined to provide the three-dimensional image of the charge distribution. In addition, wrapped anode wires that follow a helical trajectory are present. They allow to reduce dead space between APAs. In fact, they reduce the need to tile electronic readout around the perimeter of the APA. These wires improve also the reconstruction accuracy, since the angle of the wrap is chosen to have an induction plane wire that does not intersect a given collection plane wire more than once. APAs are shown in Fig. 2.13.

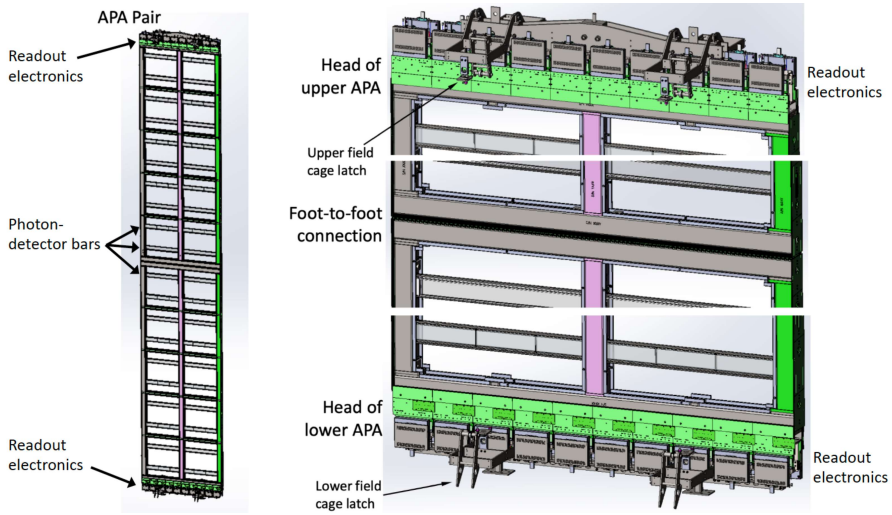

Figure 2.13: On the left, two APAs which form an APA wall. Photon detection X-Arapuca modules are installed across the width of the APAs. On the right, detail of the top and bottom of the APA stack, showing the readout electronics and at the center, where the APAs are connected [33].

The signals on the APA's wires are caught by the cold readout electronics system, placed both at the top and bottom ends of each APA. Thanks to the cryogenic

environment constituted by LAr, the thermal noise is kept very low. Within the cryostat, several stages of signal processing occur, including amplification, pulse shaping, analog-to-digital conversion, control and communication functions. The elaborated signals are then driven outside the cryostat to the DAQ (data acquisition) system.

The electric field used in the TPC volume for ionization charges drift towards the APAs is created by the high voltage (HV) system. This system contains the cathode plane assemblies (CPAs) and field cage elements that are used to reduce gradually the CPA's voltage. Each CPA is operated at a voltage of $-180\,\mathrm{kV}$ and the drift field value is then equal to 500 V/cm. The HV system uses resistive panels for the CPAs to protect the SP module elements, preventing unexpected electrical discharges and therefore avoiding damages that would negatively impact the detector performances.

The SP LArTPC is used for the reconstruction of the topology of neutrino interaction vertices. Two spatial coordinates are determined using the position of the fired wires in the APA, while the third one is obtained measuring the arrival time of the charge. The initial time is when the scintillation light produced by LAr excitation is collected by the photon detection system. Using both the drift velocity and the time difference, it is possible to calculate the third position coordinate. Then, it is possible to isolate CC neutrino interactions and also perform the identification of the neutrino's flavor using pattern recognition algorithms.

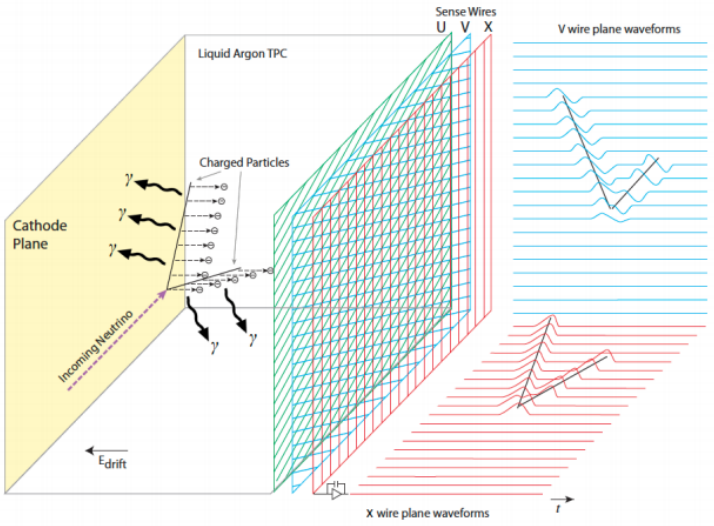

Figure 2.14: General operating principle of the SP LArTPC [26].

ProtoDUNE

A prototype detector has been built at CERN to test the technology presented: ProtoDUNE-SP. This prototype is smaller in size, but use the same technology as the future TPCs. In addition, ProtoDUNE-SP posses the same maximum drift length as the final SP TPC. The prototype is important since it allows to test different technologies. For this purpose, hadron beams and cosmic rays experiments were conduced, and large samples of high-quality data have shown the effectiveness

of the SP Far Detector design.

The photon detection system installed in ProtoDUNE-SP is similar to the future Far Detector design. ARAPUCA modules are used to measure interactions times and to get an independent measurement of the energy deposited in the prototype. This photon detection system has been characterized using the data collected during the first beam run. Others beam run are planned to optimize the detector's response.

2.2.3 Near Detector

DUNE Near Detector will be located 62 m underground, downstream of the neutrino source, at distance of 574 m from the proton target. It will be composed of three detectors: two movable and one fixed in an on-axis position, as is illustrated in Fig. 2.15.

The movable detectors are a LArTPC without magnetic fields and a magnetized Multipurpose Detector (MPD). Le latter is a High Pressure gaseous Ar TPC (HPgTPC), capable of performing tracking with high precision, surrounded by an Electromagnetic Calorimeter (ECAL) and a muon tracker. They can move to reach an off-axis position, to probe different range of the neutrino's energy spectrum.

The third detector is instead on-axis and it is called SAND (System for on-Axis Neutrino Detection). The magnet and the ECAL previously used in the KLOE experiment will be used for SAND, but a second high precision internal tracker will be added.

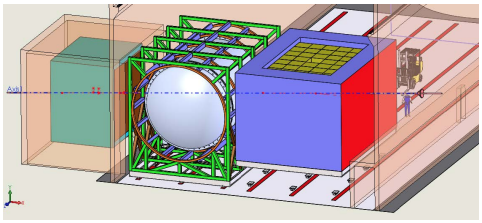

Figure 2.15: DUNE Near Detector. The beam enters from the right and encounters the LArTPC, the MPD, and the SAND on-axis beam monitor [26].

Near Detector's purpose

The Near Detector purpose is to measure the unoscillated neutrinos fluxes at the source, constraining the systematic uncertainties on the measurements of the events in the Far Detector. Both far and Near Detector will measure neutrinos' energy spectrum, using the differential rates of ν_e and ν_μ, given by:

$$\frac{dN^{FD}_{\nu_x}}{dE_{rec}}(E_{rec}) = \mathcal{N}^{FD}\int \Phi^{FD}_{\nu_\mu}(E_\nu) P_{\nu_\mu\to\nu_x}(E_\nu)\sigma^{\mathrm{Ar}}_{\nu_x}(E_\nu) R^{\mathrm{Ar}}_{\nu_x}(E_\nu, E_{rec})\epsilon^{FD}_{\nu_x}(E_\nu, E_{rec})dE_\nu, \tag{2.6}$$

$$\frac{dN^{ND}_{\nu_x}}{dE_{rec}}(E_{rec}) = \mathcal{N}^{ND}\int \Phi^{ND}_{\nu_\mu}(E_\nu)\sigma^{\mathrm{Ar}}_{\nu_x}(E_\nu) R^{\mathrm{Ar}}_{\nu_x}(E_\nu, E_{rec})\epsilon^{ND}_{\nu_x}(E_\nu, E_{rec})dE_\nu, \tag{2.7}$$

in which $\mathcal{N}$ is a normalization factor, E_ν is the true neutrino's energy, while E_{rec} is the reconstructed one. σ_ν is the neutrino interaction cross section, R_ν is the probability for a neutrino to produce a charged particle and ϵ_ν is the detector efficiency.

If both the far and Near Detector have the same target and a similar design, the ratio between the two rates would become really simple. In fact, in this case σ_ν, R_ν and ϵ_ν would be similar and then it would be possible to obtain

$$\frac{dN^{FD}_{\nu_e}}{dN^{ND}_{\nu_\mu}} = \frac{\mathcal{N}^{FD}}{\mathcal{N}^{ND}} \frac{\Phi^{FD}_{\nu_\mu}}{\Phi^{ND}_{\nu_\mu}} \frac{\sigma^{\mathrm{Ar}}_{\nu_e}}{\sigma^{\mathrm{Ar}}_{\nu_e}} P_{\nu_\mu \to \nu_e} = \frac{\mathcal{N}^{FD}}{\mathcal{N}^{ND}} \left(\frac{L^{FD}}{L^{ND}}\right)^2 \frac{\sigma^{\mathrm{Ar}}_{\nu_e}}{\sigma^{\mathrm{Ar}}_{\nu_e}} P_{\nu_\mu \to \nu_e}, \tag{2.8}$$

where two identical detectors were considered, as an approximation. As a consequence of this calculation, the ratio between the fluxes is proportional to the squared ratio of the two baselines, which is known with just 1-2% of uncertainty. On the other hand, uncertainties on neutrino fluxes are higher and are can be due to hadrons produced off the target and to the focusing design, such as horn currents and horn and target positioning.

The expected neutrino flux is obtained simulating the apparatus with Geant4. According to these simulations, the neutrino beam is composed of muon neutrinos for a 92%, while the remaining part is due to muon antineutrinos contamination for a 7% and electron neutrinos and antineutrinos for the remaining 1%. Similar proportions could be found for the antineutrino beam, where muon antineutrino constitutes a 90.4%, while muon neutrinos account for a 8.6%, with the same fraction of electron neutrinos and antineutrinos as the previous case.

Considering the described approximation, it would be possible to constrain precisely the oscillation parameters, but in actuality there are many other effects that have to be considered. It is only possible to measure the convolution of the physical quantities and it is necessary to perform an unfolding to find one of them. Hence, Near Detector's measurements are needed to constrain the ratio between near and far flux, the absolute neutrino flux, the detector efficiency and the neutrino interaction in argon, which cross section appears in the ratio between the fluxes in case of no approximation:

$$\frac{dN^{FD}_{\nu_e}}{dN^{ND}_{\nu_\mu}} = \frac{\int \Phi^{ND}_{\nu_\mu}(E_\nu) P_{\nu_\mu \to \nu_x}(E_\nu) F(E_\nu) \sigma^{\mathrm{Ar}}_{\nu_e}(E_\nu) R^{\mathrm{Ar}}_{\nu_e}(E_\nu, E_{rec}) \epsilon^{FD}_{\nu_e}(E_\nu, E_{rec}) dE_\nu}{\int \Phi^{ND}_{\nu_\mu}(E_\nu) \sigma^{\mathrm{Ar}}_{\nu_\mu}(E_\nu) R^{\mathrm{Ar}}_{\nu_\mu}(E_\nu, E_{rec}) \epsilon^{ND}_{\nu_m u}(E_\nu, E_{rec}) dE_\nu}, \tag{2.9}$$

with $F(E_\nu) = \Phi^{FD}_{\nu_\mu}/\Phi^{ND}_{\nu_\mu}$. Since the aim of DUNE is to reconstruct neutrino's events, it is important to understand in details neutrino interactions in argon. They can be modelled considering a neutrino that collides with nucleons, then scattering can occur and the nucleons can produce mesons. Subsequently, these particles can interact with other nucleons while travelling in argon. The interactions of these secondary particles contributes the most to the systematic uncertainties on the interactions.

DUNE is interested especially in the energy range between 0.5 GeV and 10 GeV, to cover the regions were quasi-elastic scattering (QE), resonance production (RES) and deep inelastic scattering (DIS) can happen. SAND detector in particular has the role of constraining these kinds of neutrino's interactions in argon. Indeed, even

a small change of the relative uncertainties can have substantial repercussions on the sensitivity to different parameters of interest, increasing the total exposure needed to achieve a 5σ significance and claim therefore a discovery.

Movable detectors

As aforementioned, the DUNE's ND is composed of three detectors: ND-LAr, ND-GAr and SAND. The first two can be moved off the beam axis, while SAND is placed on-axis [35]. The ND hall showing both the on-axis and off-axis positions is displayed in Fig. 2.16.

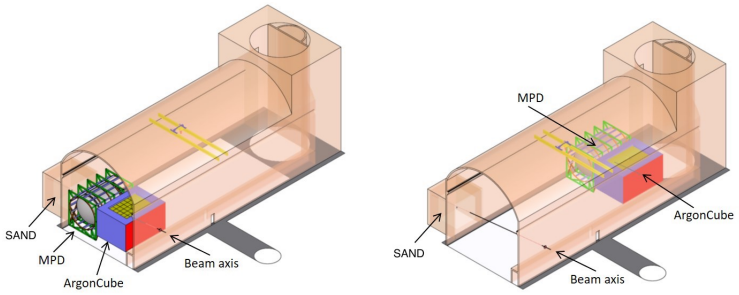

Figure 2.16: DUNE ND hall shown with component detectors all in the on-axis configuration (left) and with the LArTPC and MPD in an off-axis configuration (right). The on-axis monitor SAND is shown in position on the beam axis [26].

The ND-LAr detector is a LArTPC based on the ArgonCube technology: it will consist of a matrix of optically isolated TPCs which are read out individually. This technique is adopted to avoid event pile-up due to the high neutrino flux near the source. This detector is designed to be a 5×7 matrix of TPCs, each with optical readout to measure the timing to associate tracks and events for different modules. The positive aspect of the use of this technique is that the volumes of the TPCs are small and therefore the drift distances are short. In addition, a highly segmented readout system allows a three-dimensional reconstruction of particle's tracks and vertices.

ND-LAr's dimensions are $5 \times 5 \times 3\ \mathrm{m}^3$ and its fiducial volume is 67 ton. It is optimized to provide high statistics (10^8 ν_μ CC events/year on axis) and to contain the hadronic events. ND-LAr has low acceptance for muons with energy above approximately 0.7 GeV/c, which are not confined. Therefore, a magnetic spectrometer is required downstream of ND-LAr to measure muon's momentum and charge, which are necessary to reconstruct the neutrino energy. ND-GAr detector is designed to perform these measurements.

The ND-GAr detector (or Multipurpose Detector, MPD) consists of a high pressure gaseous argon TPC surrounded by an electromagnetic calorimeter (ECAL), immersed in a magnetic field of magnitude 0.5 T, as well as an external muon detection system. ND-GAr is designed to have a fiducial volume of 1 ton and will be able to collect approximately 1.6×10^6 CC-ν_μ events/year on-axis. The high pressure gaseous argon TPC is kept at a pressure of 10 atm, providing a low density medium with an excellent tracking resolution that will allow to measure the momenta of muons downstream of the ND-LAr.

Both ND-LAr and ND-GAr can move in positions off the beam axis to perform precision measurements, called DUNE-PRISMs (Precision Reaction-Independent Spectrum Measurements). Increasing the off-axis angle, the incident neutrino flux spectrum becomes narrower and the mean energy decreases. Even if the number of events is reduced, the energy resolution is higher. The measurements made for different off-axis angles allow to obtain the neutrino flux and the interaction cross section. In addition, they allow to perform the energy calibration, measuring the response of the detector.

2.2.4 SAND

The last part of the Near Detector is called SAND (System for on-Axis Neutrino Detection). This detector will monitor fluxes of neutrinos on the beam axis, which allows a high sensitivity to variations in the neutrino beam. SAND measurements of the neutrino flux will be complementary to the ones performed by the ND-LAr. In addition, it will be important to determine changes in the beam, especially when the other detectors are positioned off-axis. If some changes are detected, the beam is adjusted accordingly. Furthermore, by having different nuclear targets, the internal tracker will be extremely useful to develop nuclear effect models and containing nuclear interaction models uncertainties.

The design of SAND is based on the magnet and the ECAL of the KLOE experiment. SAND will be able to provide an independent measurement of the interaction rate and energy spectra of the ν_μ, $\overline{\nu}_\mu$, ν_e, $\overline{\nu}_e$ beam components. These measurements are necessary to have redundancy in the extrapolation of neutrino's and anti-neutrino's fluxes in the Far Detector. Furthermore, SAND will study the neutrino's nuclear interactions to constrain systematic uncertainties due to nuclear effects and it will monitor possible on-axis beam changes as aforementioned.

The magnet and the calorimeter

The magnet and the ECAL of SAND were part of the KLOE detector, a cylindrical collider detector used in the past to study Φ meson production at the INFN-LNF laboratories [35]. Both KLOE magnet and ECAL are shown in Fig. 2.17.

The superconducting coil produces a 0.6 T magnetic field over a volume with length 4.3 m and diameter 4.8 m. The coil is located inside a cryostat which in turn is inside the return yoke. The cold mass is approximately 8.5 ton and the mass of the KLOE return yoke is 475 ton.

The KLOE's ECAL is a sampling calorimeter composed of lead and scintillating fiber. Scintillating fibers allow a good light transmission over several meters, a timing accuracy in the order of sub-ns and a good hermeticity. The cylindrical barrel calorimeter is positioned inside the KLOE magnet, close to the coil cryostat. Furthermore, two additional calorimeters are placed at the endcaps to ensure hermeticity. Indeed, thanks to the overlap of barrel and endcaps, the calorimeter has no inactive gap between those components. The barrel consists of 24 modules, and each one is 4.3 m long and 23 cm thick, with a trapezoidal cross-section, which bases are 52 cm and 59 cm long. Each end-cap consists of 32 vertical modules, whose length ranges between 0.7 m and 3.9 m, while their thickness is 23 cm. Their

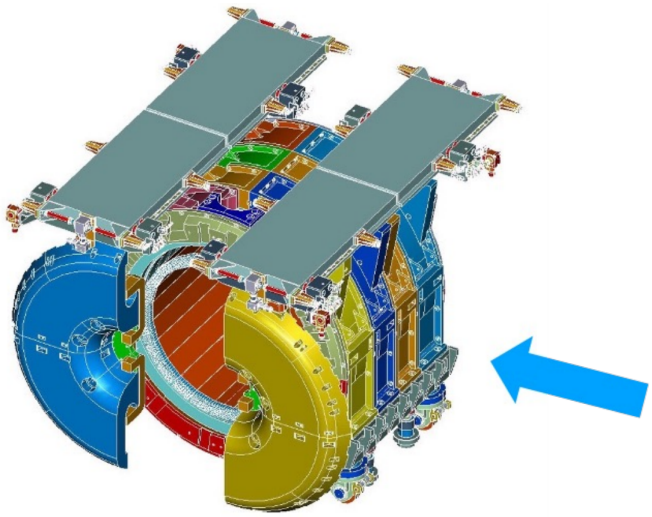

Figure 2.17: KLOE magnet and ECAL. The neutrino beam direction at DUNE is shown by the arrow.

cross-section is rectangular, of variable width. The calorimeter weight is about 100 ton. The scheme is displayed in Fig. 2.18.

All ECAL modules are stacks of 200 grooved, 0.5 mm thick, lead foils alternating with 200 layers of cladded 1 mm diameter scintillating fibers. The average density is 5 g/cm^3, while the radiation length is approximately 1.5 cm. In total, the thickness of the calorimeter is approximately 15 radiation lengths. Light guides, with an overall efficiency of approximately 80%, matching the module square end-faces to circular photo-cathodes are employed to read both ends of each module. The readout system uses 4880 phototubes and it is segmented, dividing the calorimeter into 5 planes in depth. This segmentation gives a readout resolution of 1.3 cm. A particle crossing the calorimeter deposits energy in at least five readout regions or cells. During the commissioning and running phases of KLOE, the energy and time resolution of the calorimeter were evaluated to be equal respectively to $\sigma(E)/E = 5\%/\sqrt{E(\mathrm{GeV})}$ and $\sigma(t) = 54/\sqrt{E(\mathrm{GeV})}$ ps.

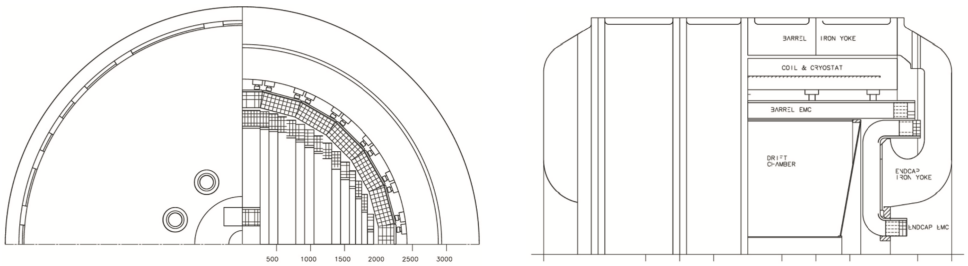

Figure 2.18: On the left, trapezoidal section of the barrels with lead scintillating fiber inside. On the right, vertical end-cap modules. Units are expressed in mm [35].

The inner tracker

The chosen design for the inner tracker of SAND consists into Straw Tube Tracker (STT) modules filling the inside volume of the ECAL, as well as a small upstream

region instrumented with a LAr active target [35].

STTs will be used to achieve a control of the configuration, chemical composition and mass of neutrino targets, similar to the one obtained in electron scattering experiments. An STT is composed of low-mass tungsten straws with an outer diameter of 5 mm. Each module of an STT is composed of a double layer of tubes staggered by a half-diameter. Two modules are assembled together, one vertically and one horizontally. The section of an STT module is illustrated in Fig. 2.19. The tubes are filled with a mixture of 70% Xe and 30% CO_2 at 1.9 atm. The single hit space resolution is designed to be less than 200 µm.

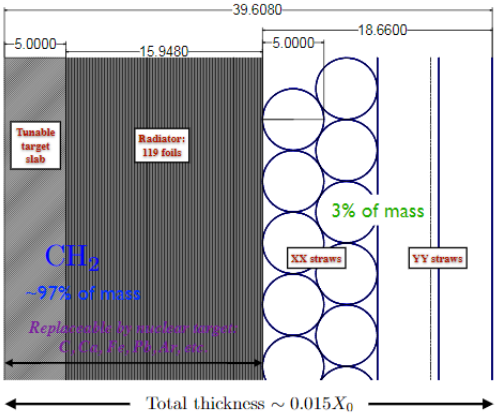

Figure 2.19: Section of an STT module, length are in mm.

Before each double module, a radiator made of 150 polypropylene $(C_3H_6)_n$ foils is used for the e/π differentiation exploiting the transition radiation emission. In addition, a polypropylene target slab is positioned after the STTs layers to achieve the desired target mass and detector density.

Both the radiator and the polypropylene slab can be removed and replaced with different nuclear targets. These targets are made by plates with tunable thickness in order to provide the same fraction of radiation length as the configuration with the radiator. Two of the most important materials that could be used as target are graphite and calcium. The first one is used to perform background measurements while a Ca target, having a similar atomic weight as argon, allows a complete characterization of the nucleus with mass number 40.

The STT design features the use of hydrocarbon targets, with a different mass number w.r.t. the argon, which can provide information to develop nuclear effects models, to verify the interaction model and to measure systematic uncertainties. In particular, thin target layers of passive material with high chemical purity are placed between the straw layers, to distribute the target mass all over the volume. 4.7 t of polypropylene foils will be used in 78 modules, together with 504 kg of graphite. The average density is 0.18 g/cm^3, corresponding to a thickness of 1.33 radiation lengths. It is important to choose the passive target materials as well as the vertex, angular, momentum and timing resolutions to correctly associate neutrino interaction to a target element. The total number of straws in the STT is over 2×10^5 and the number of channels is the same.

GRAIN active LAr target

A LAr mass target of approximately 1 ton will be placed in the upstream region of the SAND magnetized volume. This detector is called GRAIN (GRanular Argon for Interactions of Neutrinos) and will be used to study neutrino interaction topology in LAr, to measure the LAr-neutrino cross-section and to reduce the systematic errors. GRAIN positioning is shown in Fig. 2.20.

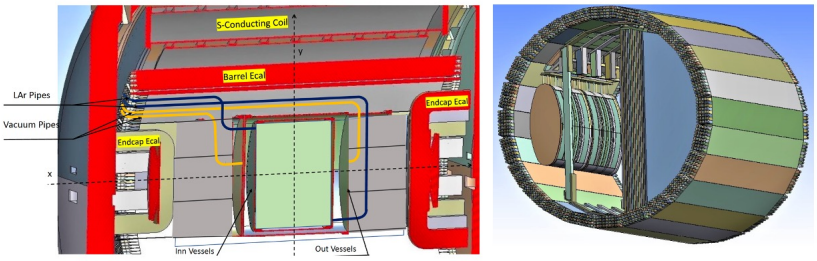

Figure 2.20: View of the inner volume of SAND, showing the position of GRAIN. Inside the KLOE calorimeter an STT module is shown, on the right, together with the GRAIN cryostat.

As aforementioned, the measure of the neutrino event rate is the convolution of many factors, including the neutrino-nucleon interaction cross section. LAr is therefore used at both the near and Far Detector to have the same nuclear target and thus cancel the effects of nuclear smearing, reducing the uncertainties given by the theoretical models.

However, a comparison between the two detectors spectra is difficult. Indeed, the large difference between the angular acceptance of the near and far detectors makes the observed spectra different. In addition, the Near Detector suffers from pile-up events due to the high intensity of the beam. The idea is to constrain the Near Detector measurements using information on flux, cross section, energy reconstruction and detector effects. GRAIN will provide a measurement of the neutrino spectrum, as well as of its flavor and it will be used to study in deep the neutrino-Argon cross section. Moreover, since ND-LAr and ND-GAr detectors will move off-axis for about half of the operation time, GRAIN will constitute a complementary Ar target permanently located on-axis.

GRAIN's thickness along the beam direction will be small, just one radiation length, to reduce energy loss, showering and multiple scattering, since the outgoing particles will have to be analysed by the downstream STT system. The cryostat walls will be made of C composite material reinforced by internal thin aluminium foils.

Chapter 3

GRAIN detector

3.1 Principle of coded aperture imaging in GRAIN

At the time of this work, the GRAIN design is still in the optimization stage. It will be an innovative LAr detector that can reconstruct neutrino interactions using scintillation light to image particle tracks. It will be instrumented with an optical detection system to collect Vacuum Ultra-Violet (VUV) scintillation light at 127 nm on finely segmented focal planes. Two VUV imaging systems are under study: one is based on lenses, while the other is based on coded aperture masks, to create a multi pinhole camera. However, the two technologies have complementary characteristics and, therefore, it is possible that the final design will embed both lenses and masks.

The reasons why a traditional LArTPC is not suited for SAND are the electron drift time in the order of ms, too slow to cope with the high event rate at the ND, and the required placement of the target inside the magnetized volume. At the Far Detector, the scintillation light has its wavelength shifted and it is used to perform low energy physics measurements and charge-light calorimetry. The FD will have a time response in the order of some milliseconds due to the drift velocities of the electrons in a large volume. This response is acceptable considering the low event rate and the large size of the volume. On the other hand, a similar time response would cause a pileup of the events in the SAND LAr volume and, thus, a much faster detector response is needed.

The scintillation properties of liquid argon allow to perform both calorimetric and spatial measurements by means of an optical detection system capable of collecting the VUV scintillation emission. For electrons or Minimum Ionizing Particles (MIPs), Liquid argon emits about 40,000 photons/MeV of deposited energy [36], with a peak intensity near 128 nm. In addition, the Rayleigh scattering length is about 99 cm at this wavelength, while the light attenuation length is approximately 66 cm [37]. Thus, LAr is transparent to its own light and it is suitable to perform imaging, since it is possible to obtain a response time of few nanoseconds while maintaining a high spatial resolution, through the use of an appropriate optical system. Such an optical system must collect enough light and the photo-sensors must be segmented in order to be capable of providing an adequate resolution. However, there are some issues: traditional lenses and mirrors are inefficient for

transmission of VUV light; the readout electronics must be able to operate in cryogenic conditions and with single-photon detection capabilities; it is required a large field of view to focus as many tracks as possible, since the distance of event tracks can be of few meters.

A possible solution would be to use the coded aperture mask technique, which is already used in X-ray and γ-ray astronomy. In such an optical detection system, the scintillation light signal would be filtered by coded aperture masks, slabs of opaque material with a certain number of holes, placed on the sides of the cryostat in front of a photo-sensor. The advantage of using coded aperture masks is that they can provide a high Photon Detection Efficiency (PDE).

The idea is to reconstruct the track of charged particles events in the LAr volume by collecting the scintillation light produced by their passages. The light hits the mask and produces a pattern of lights and shadows on the photosensors. Then, it is possible to use an algorithm to reconstruct where the light production occurred, decoding the different patterns depending on the direction of the light with respect to the mask. The obtained signals would be 2D images detected by multiple masks coupled with photosensors. These images could then be combined in a stereo view, obtaining a 3D reconstruction of an event using just the scintillation light.

In GRAIN, matrices of Silicon Photomultipliers (SiPMs) will be used as photosensors. SiPMs offer the advantage of robustness, a strong reduction of the dark noise at low temperatures and a high definition, since they can possess a lot of channels. Furthermore, they are sensitive even to single photons and they are immune to magnetic fields.

3.1.1 Pinhole cameras

An imaging system must correlate events with a site of emission since an image is a mapping of some distribution over space. Arguably, the simplest imaging device is the pinhole camera, which is depicted in Fig. 3.1.

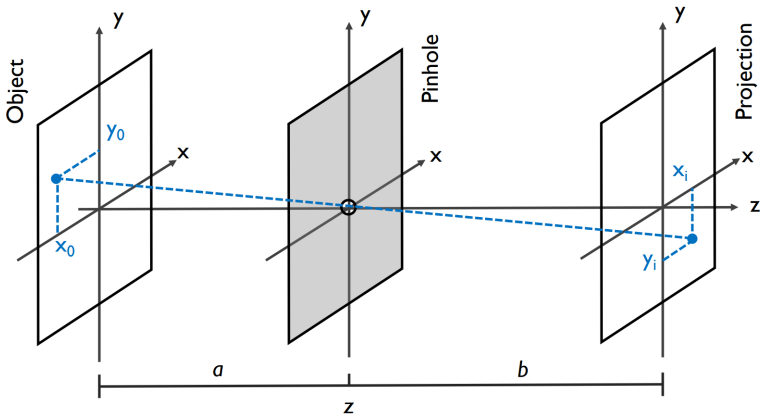

Figure 3.1: Pinhole camera geometry [38].

A pinhole camera consists of nothing more than a slab of material that is radiation-opaque and into which a very small hole has been pierced [38]. Each event

comes from the object through the pinhole following a straight line, therefore each point of the detector represents a point of the source. In particular, the detector will record an inverted image of the object.

From the one-to-one correspondence established between object and detector, it follows the photon distribution recorded at the detector of a pinhole camera. The photon distribution at a generic detector position $R(x_i, y_i)$, must be due only to the point source at (x_0, y_0). Therefore, $R(x_i, y_i)$ has to be proportional to the point source's irradiance $O(x_0, y_0)$:

$$R(x_i, y_i) \propto O(x_0, y_0). \tag{3.1}$$

It is then possible to define the vectors: $\vec{r_i} = (x_i, y_i)$ and $\vec{r_0} = (x_0, y_0)$, which are related by:

$$\vec{r_0} = -\frac{a}{b}\vec{r_i}, \tag{3.2}$$

because the ray that goes from $\vec{r_0}$ to $\vec{r_i}$ must pass through the pinhole. In this formula, a is the distance from the pinhole plane to the object plane, while b is the distance between the pinhole plane and the detector plane. Using the last equation, it is then possible to write:

$$R(\vec{r_i}) \propto O\left(-\frac{a}{b}\vec{r_i}\right). \tag{3.3}$$

This equation proves that the image on the detector is a copy of the original object, even if it is inverted, due to the minus sign, and it is rescaled by a factor a/b. In this expression, a and b can be any positive number: if $a > b$, the pinhole plane is closer to the detector plan than to the object plane, and the object appears smaller, while if $a < b$, the object appears bigger. The ratio of the projected object size to the original is called rescaling coefficient and it represents also the magnification coefficient m_p of the pinhole camera:

$$\frac{h_i}{h_0} = \frac{b}{a} = m_p. \tag{3.4}$$

If $h_i = d_d$, where d_d is the size of the detector, it is is possible to obtain the Field of View (FoV), which is the set of points in the plane of the object that can be measured:

$$FoV = \frac{d_d}{m_p}. \tag{3.5}$$

If the pinhole is ideal, the resolution is infinite. However if the pinhole has a finite width w_m, as shown in Fig. 3.2 each point of the source projects an image of size w_d:

$$w_d = \frac{a+b}{a} w_m = (1 + m_p) w_m. \tag{3.6}$$

Then, the resolution l of the system can be defined as the minimum distance between two points in the plane of the object such that their projections are separated in the image:

$$l \geq \frac{a}{b} w_d = \left(1 + \frac{1}{m_p}\right) w_m, \tag{3.7}$$

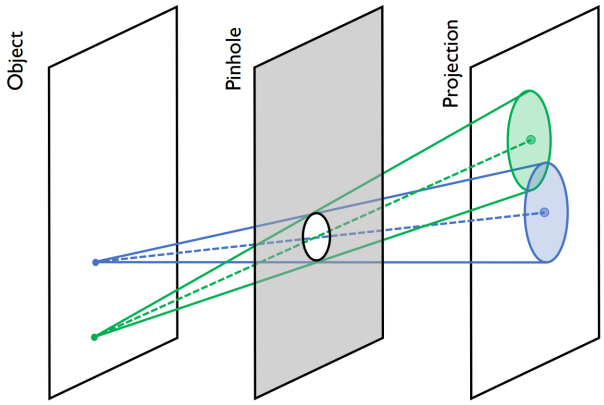

Figure 3.2: Illustration of the resolution degradation that results from enlarging a perfect pinhole for more throughput. The projections in the ideal pinhole scenario are shown by dotted lines and by points [38].

in which, obviously, low values of l indicate a good resolution, which is limited by the size of the pinhole w_m. One can see that the resolution improves if the magnification increases, while the field of view gets smaller.

The ratio between the field of view and the resolution can be used as a figure of merit for an imaging system, which should have the largest FoV and the best resolution:

$$\frac{FoV}{l} = \frac{d_d}{(1+m_p)w_m}. \tag{3.8}$$

In the limit $m_p = 0$, the ratio assumes its maximum value of d_d/w_m.

A perfect pinhole with an ideal resolution would be useless, since a null aperture area implies a null photon flow through the hole as well. Therefore, the pinhole's size must strike a balance between the demand of high resolution and high detection efficiency. To get over this problem, the coded aperture mask method was created.

3.1.2 Coded aperture masks

The goal of coded apertures is to have a high throughput while achieving the resolution of a tiny pinhole. The essential idea is to open numerous little pinholes rather than a single large one in order to overcome the low passing photon flux. The physical realization of a pinholes arrangement in a specially chosen pattern is called mask. A coded aperture camera is composed of a mask coupled to a detector.

In case of a point-like source, a single pinhole which counts s photons would have a Signal-to-Noise Ratio (SNR) equal to $SNR = \sqrt{s}$. While in case of a coded aperture mask with N holes, each of the same size as the single one, the same s photons would be counted independently N times, bringing $SNR = \sqrt{Ns}$. Therefore a coded aperture masks has better SNR with respect a single pinhole, by a factor $\sqrt{N}$.

Encoding the signal

Coded aperture imaging can be thought of a process made of encoding and decoding. The encoding consists in the projection through the mask of the object onto the detector. Furthermore, it is possible to calculate the projection from the aperture and the object with just geometric optics [38].

The photon distribution R due to the point source at position $\vec{r}_0$ and measured at the detector at position $\vec{r}_i$ has to be proportional to the irradiance $O(\vec{r}_0)$, modulated by a factor A, which is called transmission of the mask, which has to be evaluated at the point of intersection with the ray going from $\vec{r}_0$ to $\vec{r}_i$:

$$R(\vec{r}_i) \propto O(\vec{r}_0)\, A\left(\vec{r}_0 + \frac{\vec{r}_i - \vec{r}_0}{z} a\right), \tag{3.9}$$

where a is the distance between the object plane and the mask plane, while z is the distance between the object plane and the detector plane. In order to make the model simpler, it is possible to consider A a two-valued function. In particular, by considering a mask as a grid of square holes and opaque elements alternated, it is possible to represent A with a matrix with just 1s (holes) and 0s (opaque elements).

The total recorded photon distribution on the detector can simply be obtained by integrating over the object plane, considering in this way all the point sources which are part of the object:

$$R(\vec{r}_i) \propto \iint_{\vec{r}_0} O(\vec{r}_0)\, A\left(\vec{r}_0 + \frac{\vec{r}_i - \vec{r}_0}{z} a\right)\, d^2\vec{r}_0. \tag{3.10}$$

It is assumed that the detector response is linear: the simultaneous exposition to several sources is equal to the sum of the responses obtained from the sources taken one at a time.

Then, using $z = a + b$, where b is the distance between the mask plane and the detector plane, and defining $\vec{r}_0^{\,i} = -(b/a)\vec{r}_0$, which is the point of the detector aligned with $\vec{r}_0$ and the mask center, it is possible to write:

$$R(\vec{r}_i) \propto \iint_{\vec{r}_0^{\,i}} O\left(-\frac{a}{b}\vec{r}_0^{\,i}\right)\, A\left(\frac{a}{z}(\vec{r}_i - \vec{r}_0^{\,i})\right)\, d^2\vec{r}_0^{\,i}. \tag{3.11}$$

Afterwards, O', which is the scaled and inverted version of O, and A', which is the scaled version of A, are defined as follow:

$$O'(\vec{r}) \equiv O\left(-\frac{a}{b}\vec{r}\right), \qquad A'(\vec{r}) \equiv A\left(\frac{a}{z}\vec{r}\right). \tag{3.12}$$

Using the new definitions, it is possible to write:

$$R(\vec{r}_i) \propto \iint_{\vec{r}_0^{\,i}} O'\left(\vec{r}_0^{\,i}\right)\, A'\left(\vec{r}_i - \vec{r}_0^{\,i}\right)\, d^2\vec{r}_0^{\,i} = O' * A', \tag{3.13}$$

which shows that the projection is described by the convolution of the pinhole image of the object O' with the projection of the mask pattern A'. This equation

can be interpreted physically by considering the projection on the detector as the sum of magnified mask patterns, which are shifted according to the position $\vec{r}_0$ of the point source, which casts the shadow, and are weighted according to its irradiance.

Decoding the signal

Since each point of the source is present in the projection because it deposits a shadow of the mask on the detector, it is possible to use the correlation method of decoding to find mask patterns in the projection [38]. The reconstructed object $\hat{O}$ is defined as $\hat{O} \equiv R \times G$, where G is a decoding array called kernel, while $\times$ represents the correlation operator, defined as:

$$H(\vec{y}) = F(\vec{x}) \times G(\vec{x}) = \iint F(\vec{x})G(\vec{y}+\vec{x})d^2\vec{x}. \tag{3.14}$$

The expression for R previously found, with the introduction of some noise N which adds to the recorded data in a real case, is $R(\vec{r}_i) \propto O' * A' + N$. This expression can be substituted inside the relation for $\hat{O}$, obtaining:

$$\begin{aligned} \hat{O} &= (O' * A' + N) \times G \\ &= (O' * A') \times G + N \times G \\ &= O' * (A' \times G) + N \times G. \end{aligned} \tag{3.15}$$

However, if $A' \times G = \delta$, the last equation simply becomes:

$$\hat{O} = O' + N \times G, \tag{3.16}$$

where the noise term $N \times G$ represents a constant background to the image, since it is a convolution of a constant with a function.

In short, the correlation takes the decoding pattern G, shifts it, multiplies it point by point with the data R and then adds all products by integration. The result is the brightness of the image at a certain reconstruction point. Then, the image is completed by repeating the procedure for all the shifts.

The condition $A \times G = \delta$ means that the correlation tries all possible shifts and indicates the one matching the shift of the mask projection with a bright spot. Since this shift depends on the position of the source, such location is indicated by the bright spot.

To sum up, the reconstruction finds a recognized pattern in a signal. In communication theory, this procedure is called *matched filtering*, and it is the best method to find a known signal in the background when the SNR tends to be zero. The design of the coded aperture is limited to patterns with a particularly specific feature and this represents a disadvantage. Fortunately, these patterns are frequent and there are several families of them that can be found in literature.

The deconvolution mechanism described so far is the traditional method for the reconstruction of images, however the light that will be collected by GRAIN is too scarce to allow a good reconstruction. GRAIN will therefore use another algorithm for the 3D reconstruction of neutrino interactions.

3D reconstruction

A single camera can only provide two-dimensional images by using the reconstruction method which consists of encoding and decoding an image of an object. Therefore, it can be suited for applications where depth information is irrelevant, such as X-ray and γ-ray astronomy and medical or industrial imaging. In case a three-dimensional reconstruction of the source is needed, as for the GRAIN detector, images taken by numerous cameras placed in various positions have to be combined in order to create a stereo view of the event. This technology is still under study and its potential is now constrained by the challenge of creating a combined reconstruction algorithm that can operate with the limited detector efficiency currently available.

The algorithm that will consist in a weighted back propagation method to form a 3D image directly, and was inspired by SPECT (Single Photon Emission Computerized Tomography) pinhole techniques. A camera in GRAIN will be constituted of a SiPM matrix placed in front a coded aperture mask. After the passage of charged particles inside the liquid argon volume, the amount of incident photon hits is measured for each sensor pixel in a camera. Each hit is then propagated back into the LAr volume through every hole in the mask, with an appropriate weight assigned to voxels (the equivalent of pixels for a 3D space), in which the volume is subdivided. Indeed, there are pixel-hole combinations that are more probable than others, therefore a different weight, which depends on the solid angle, is attached to each of them. A probability amplitude in the segmented reconstruction volume is calculated by adding these weights. In this way, combining all the information, a 3D map of the voxels which have an higher probability to have generated photons is obtained. A scheme of the working principle of the algorithm is shown in Fig. 3.3.

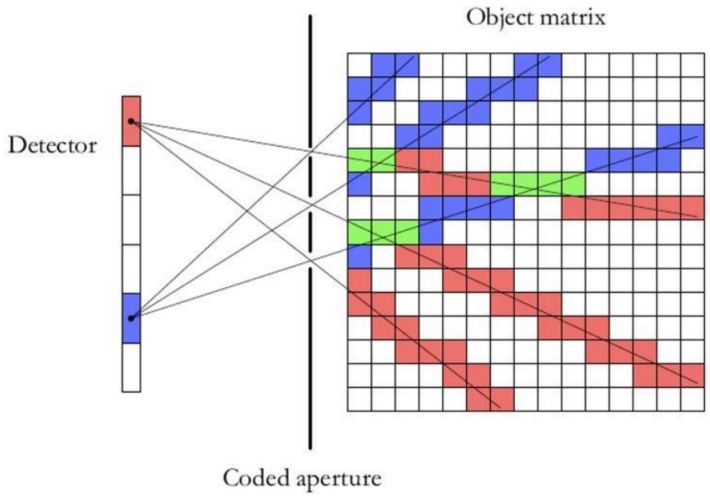

Figure 3.3: Scheme of the 3D reconstruction algorithm that will be used in GRAIN.

There are several challenges that have to be addressed. First, there are many mask holes and voxels, respectively 1024 and 4000, therefore the computing time is

high and it requires GPU acceleration. Furthermore, it is possible that a neutrino interaction produces a charged particle between the mask and the SiPM matrix, disabling that camera during an event, since a pattern of lights and shadows will not form. If this happens, that camera cannot be used for the reconstruction. Another issue is that is important to distinguish signals from the background in a clear way. The problem is that the probability related to a signal is slightly higher of the probability of the background. In addition, after having reconstructed the most probable voxels where the photons were produced, it is necessary also to implement an algorithm to reconstruct a track of the particles.

Mask patterns

The future plan is to cover the inner walls of the LAr volume of GRAIN with coded aperture cameras, which consist in masks coupled with SiPMs placed beyond them. Especially, the masks will be MURAs (Modified Uniformly Redundant Arrays) [39], which represent a particular family of mask patterns. It is possible to generate square MURA masks with a prime number of pixels p, which is called rank of the mask. An example of MURA patterns is shown in Fig. 3.4.

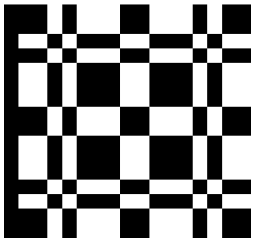

Figure 3.4: Squared MURA aperture pattern for $p = 17$. Holes are represented by black pixels, while the opaque elements are represented by the white pixels.

A crucial characteristic of MURAs is the throughput of the aperture, which is always approximately 50% of the total number of elements. The quantity of open components for a squared mask with sides of p pixels is equal to:

$$N_{open} = \frac{p^2 - 1}{2} = \frac{N_{total} - 1}{2}. \tag{3.17}$$

Two distinct periodic mosaic patterns with side dimensions of $2p - 1$ and $2p$ are being investigated for the use in GRAIN detector, where p is the rank of the MURA. The periodicity is important since it increases the field of view of an imaging system.

3.2 Simulations

A toy Monte Carlo simulation has been developed in order to quantitatively examine the coded mask system so far described and to gain a more accurate understanding of the performance of the coded masks [40].

It is necessary to use more than one coded small-order mask to effectively handle the problem of spatial localization of the source. Two parallel coded systems using the same focal plane make up the simplest mask setup that is possible to consider.

It is important to decode the light signal encoded by the masks, therefore, simulations were run with various parameters (mask rank, pixel sizes, mask-source and mask-detector distances). For example, at the corners of a square on the x, z plane, the simulation of four point-source has been performed, which is shown in Fig. 3.5.

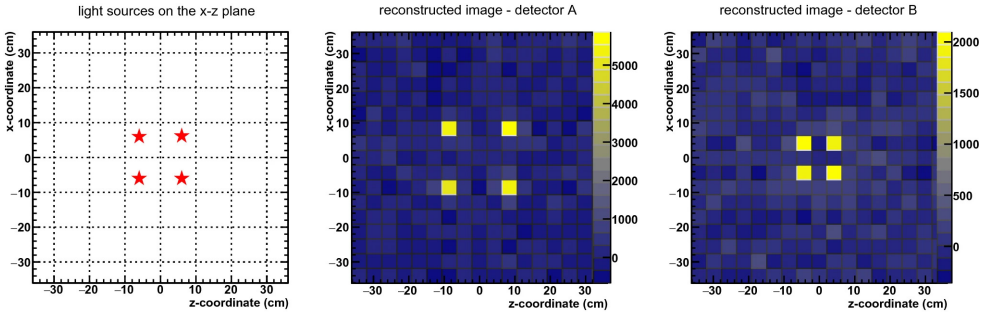

Figure 3.5: Simulation of four light-points. In the x-z perspective, the left frame corresponds to the actual sources. The reconstructed signal is represented by two distinct detectors in the other two frames. The sources are closer to detector A (center frame) than detector B (right frame) [40].

Another example of simulation is displayed in Fig. 3.6, left frame. Here, the tracks generated by a simulated neutrino interaction are shown in the x-z view. Obviously the tracks do not lay on a single plane. The light signal emitted by the tracks is collected and reconstructed by two parallel masks sharing the same focal plane.

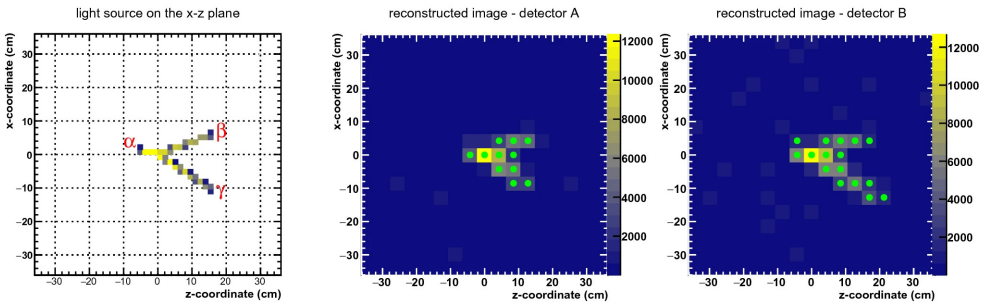

Figure 3.6: A neutrino interaction simulation is shown in the left frame. The three tracks are not situated on a single plane. The reconstructed image is visible in the x-z perspective in the central and right frames. The pixels chosen as the signal are identified by the green dots that are overlaid [40].

In addition, the signal due to a linear light-track has been simulated and then analyzed by means of three detectors. The resulting images are illustrated in Fig. 3.7 with a linear fit superimposed on the selected pixels, represented as black dots.

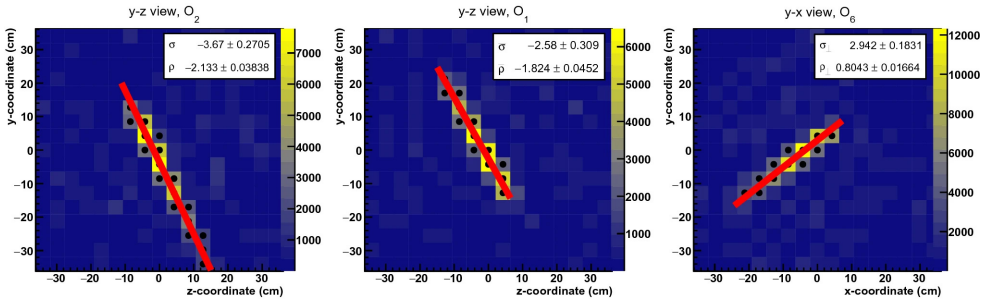

Figure 3.7: The linear track's reconstruction using data from three separate detectors is shown. The pixels (black dots) chosen in accordance with the initial signal recognition technique are fitted linearly. The original track has been recreated in three dimensions using the fit parameters displayed in the frames [40].

3.3 GRAIN early design

GRAIN design is still in the early phases of its development. The inner volume of the cryostat, will have a width (along the x axis) of 150 cm, with elliptical sides (along the y-z plane) of 147.6 cm in height and 47.5 cm in length, respectively along the y and z axes. A scheme of GRAIN can be seen in Fig. 3.8.

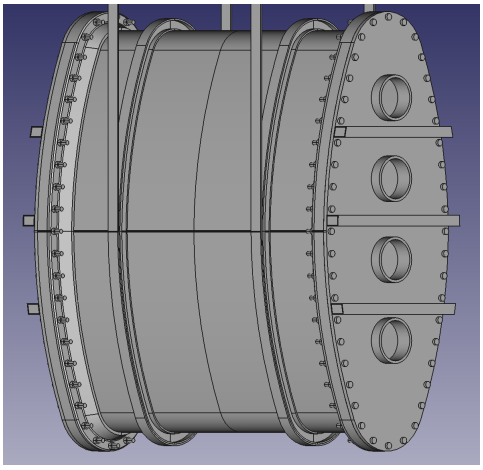

Figure 3.8: GRAIN vessel. The inner part will be filled of liquid argon, while the outer part will be filled with air to thermally insulate the inner volume.

The imaging system is still in the design phase, both using lenses and masks. Below, some preliminary numbers of how it will be structured are shown. The imaging system will be composed of 76 coded aperture cameras, 8 on both the elliptical sides and 60 on the curved surface. Such number is the maximum that can be achieved considering the dimension of the detector. The mask patterns will be 33×33 odd-dimension mosaic masks. The sides of the mask pixels will be 2.33 mm long, with a 0.2 mm edge between each pixel. Thus, the total length will account to 94 mm. Masks will be obtained from a 0.1 mm thick steel sheet. The distance between mask and detector plane will be 20 mm to allow complementary depths of field.

The detector will be a 32×32 SiPMs matrix with a pixel size of 3 mm, separated by a 0.2 mm spacing, for a total detector side length of 51.2 mm. The total volume of LAr will be 9.1×10^5 cm^3. However, a fiducial volume of 4.9×10^5 cm^3 will be chosen to exclude possible artefacts which can form close to the camera. The GRAIN early design is shown schematically in Fig. 3.9.

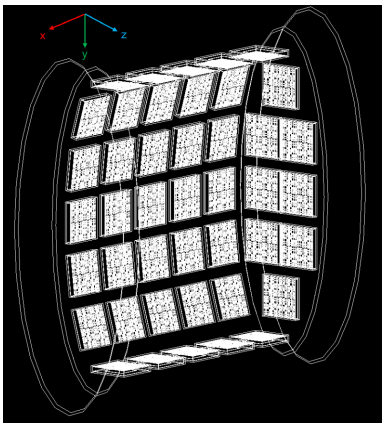

Figure 3.9: GRAIN geometry. Cameras are disposed in a way that maximizes their number. The neutrino beam direction is along the positive z-axis. The two front sides were cut to allow a better view.

Electronics that could enable imaging in GRAIN are being studied and tested. Indeed, the required cryogenic temperature poses a real challenge as it modifies the properties and parameters of the readout electronics within the LAr volume. For this reason, the ALCOR (A Low-power Circuit for Optical sensor Readout) mixed-signal ASIC prototype optimized for the readout of SiPMs at cryogenic temperatures is being considered and its usage is under study. GRAIN's back-end electronics will instead be implemented in FPGAs (Virtex-7 VC707) outside the cryogenic environment.

3.4 SiPM photosensors

A photosensor is a device that can detect ionizing radiation by providing an output signal having a current intensity or potential difference proportional to the intensity of the detected radiation.

There are several types of photosensors and one of them is the SiPM (Silicon Photomultiplier). A SiPM can be viewed as a set of binary cells that provide information about the intensity of incident light by counting the number of cells hit. They have an excellent ability to count photons, and their use has several advantages over PMTs. In fact, SiPMs have higher quantum efficiency than PMTs over a wide wavelength range. In addition, the working principle of SiPMs is based on the transition of electrons from the valence band to the conduction band, a process that generally requires less energy than extracting electrons from the photocathode of PMTs. Furthermore, SiPMs are immune to intense magnetic fields and they can therefore replace PMTs in applications where the latter cannot be used because they require shielding from magnetic fields. SiPMs are compact with a high

channel density and are economical. In fact, since silicon is a key material in the construction of components and circuits, technological advances mean that SiPMs will cost less and they can be mass produced. Another characteristic of SiPMs is that both the gain and the number of cells affected by secondary avalanches depend significantly on the temperature.

3.4.1 Avalanche multiplication

When a p-type doped region and an n-type doped region are in contact in the same semiconductor, a region deprived of free charge carriers is formed, which is called *depletion region*. In fact, because of the strong gradient due to the different doping type, the majority charge carriers undergo diffusion into the adjacent semiconductor. Thus electron-hole recombination processes begin, leaving uncompensated ions, which generate an intense electric field such that they oppose further migration of charge carriers beyond the junction.

By studying the I-V characteristic of a p-n junction, shown in Fig. 3.10, it is observed that by increasing the applied reverse bias voltage, a value is reached for which the reverse current increases extremely rapidly.

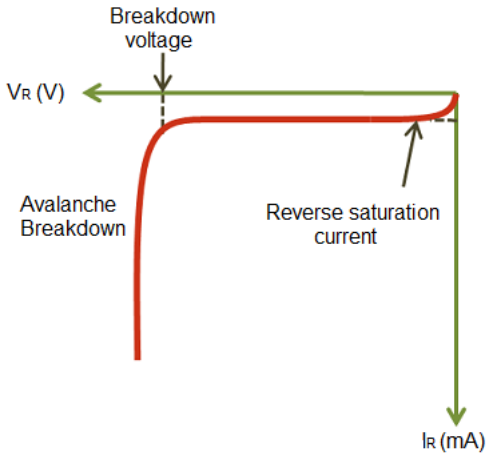

Figure 3.10: I-V characteristic of a diode, reverse bias zone. It can be seen that above the breakdown voltage value the current increases rapidly.

The voltage at which this phenomenon occurs is called the inverse *breakdown* voltage (V_{bd}), since dielectric breakdown occurs. The voltage remains practically constant at V_{bd}, while the reverse current increases very rapidly. A device working at voltages above its breakdown voltage, works in Geiger mode, in analogy to the ionization discharge observed in a Geiger-Müller tube. The exact value of the breakdown voltage can be obtained from the graph of the square root of the current as a function of the voltage, as in the example in Fig. 3.11. In fact, a definition of V_{bd} is the voltage value of the intersection point between the two lines that are obtained by performing a fit of the constant part and of the linear part of the graph [41].

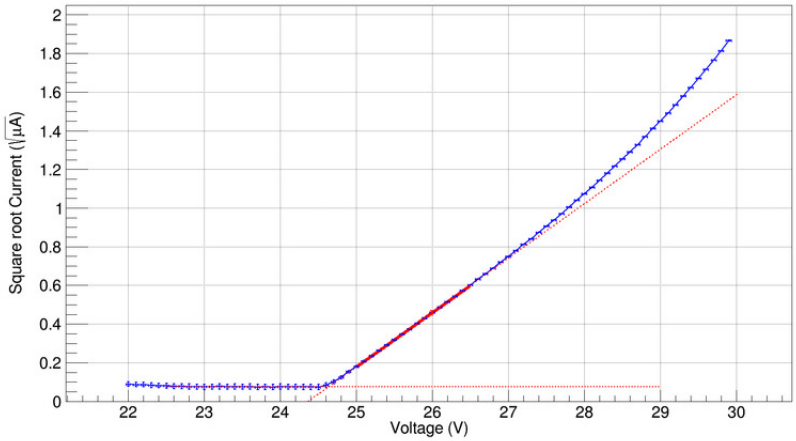

Figure 3.11: Root of inverse voltage as a function of voltage. From this graph, it is possible to derive the exact value for the breakdown voltage. In fact, V_{bd} is equal to the voltage value of the point of intersection between the two lines that are obtained by performing a fit of the constant part and of the linear part of the graph [42].

If the junction is low-doped, dielectric breakdown occurs through a mechanism called avalanche multiplication. The minority carriers are accelerated by the electric field present in the depletion region, which is sufficiently intense to provide the carriers, between two consecutive impacts, with enough kinetic energy to break a covalent bond. This process is called impact ionization. Each new carrier produced in this way takes part in the mechanism with the production of other carriers in a multiplicative process, which is therefore called avalanche effect.

In a SiPM, the breakdown voltage is the minimum voltage that must be applied to have a discharge after absorption of a photon. V_{bd} depends on the electric field inside the SiPM, which in turn depends on the doping and thickness of the regions of the SiPM. The bias voltage (V_{bias}) at which SiPMs operate is a few volts higher than V_{bd}. The difference between V_{bias} and V_{bd} is called *overvoltage* (ΔV).

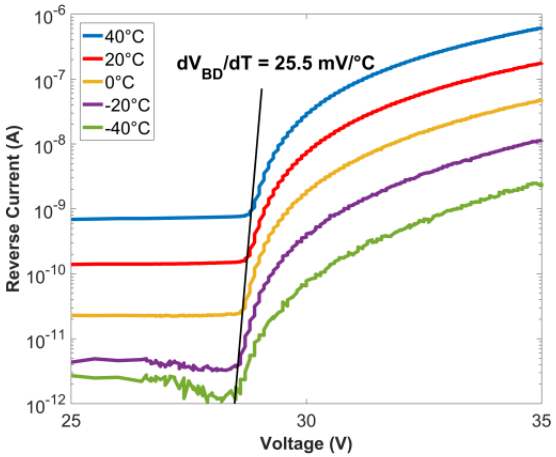

Figure 3.12: I-V characteristics for different temperature values between $-40\,^{\circ}\mathrm{C}$ and $40\,^{\circ}\mathrm{C}$. It can be seen that the breakdown voltage increases with increasing temperature.

As can be seen in Fig. 3.12, as the temperature increases, V_{bd} also increases. This occurs because of the change in charge carrier mobility and ionization rate. In fact, as temperature increases, the frequency of collisions against lattice ions increases, the average free path decreases, and the average kinetic energy acquired between two collisions decreases. The dependence of V_{bd} on temperature can be considered linear to a first approximation.

3.4.2 SiPM working principle

The working principle of SiPMs is based on the p-n junction of silicon. However, the structure is more elaborate than the simple junction. In fact, it is built on a thin layer (3-5 µm) of low-doped π-type silicon created on a highly doped p+-type layer. The junction is achieved by creating an n+ zone on the surface region of the substrate. Furthermore, a second p-type region is placed below the n+ region to fix to the desired value the breakdown voltage [43]. The final structure, starting from the top, thus turns out to be n+/p/π/p+, as observed in Fig. 3.13.

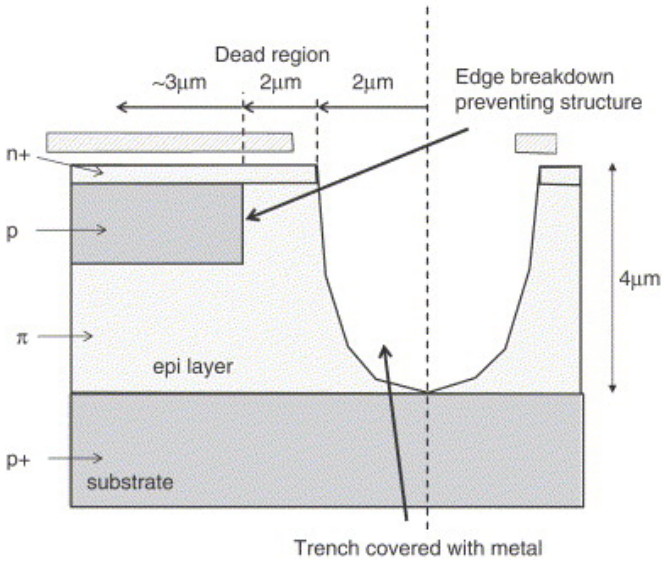

Figure 3.13: Diagram of the doping region near the edge [43].

One of the simplest types of solid-state photodetectors consists of SPADs (Single Photon Avalanche Diodes), which are photodiodes that operate in the Geiger regime to obtain gains on the order of 10^6.

When a sufficiently high electric field, at least 5×10^5 V/m, is generated within the silicon depletion region, a single absorbed photon can trigger an ionization cascade. However, in order to detect subsequent photons, each avalanche discharge is interrupted by a *quenching* resistor placed in series with the diode, limiting the current drawn during the breakdown. This reduces the reverse voltage applied to the diode to a value less than its breakdown voltage, thus stopping the avalanche. The diode then returns to its bias voltage and is available to detect subsequent photons. A typical pulse produced at the output of a photodiode is shown in Fig. 3.14.

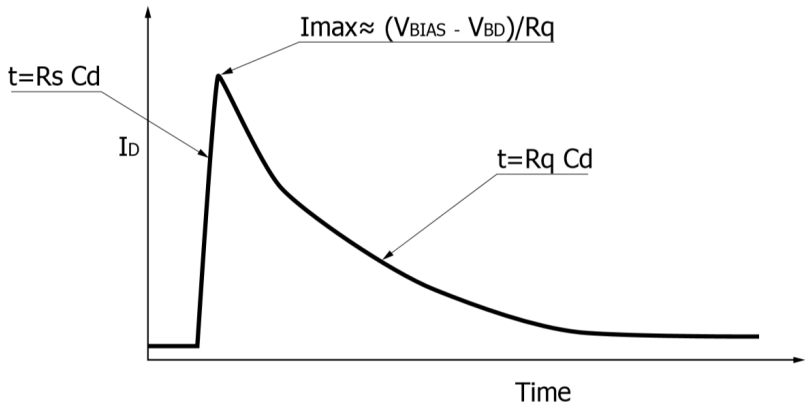

Figure 3.14: Typical output pulse of a SPAD photodiode [45].

As can be seen from the output signal of a Geiger-mode SPAD at the time an avalanche discharge occurs, a peak marked by an extremely short rise time τ_s and a much longer fall time τ_c is observed.

The equivalent circuit of an avalanche photodiode in series with an quenching resistor is shown in Fig. 3.15. The closing of the switch corresponds to a photon triggering an avalanche multiplication process.

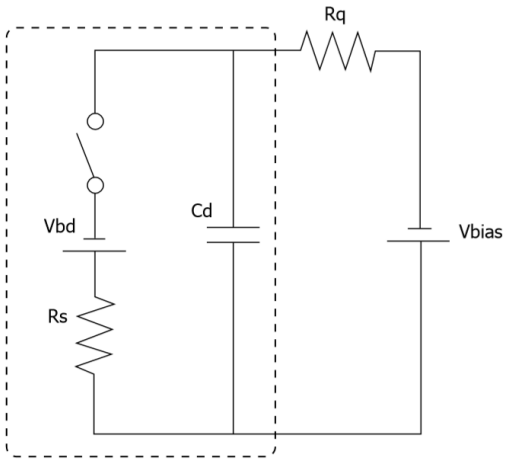

Figure 3.15: Equivalent circuit of a SPAD in series with a quenching resistor [45].

Initially the capacitor C_d, representing the capacitance of the junction, is at a voltage V_{bias}. In this situation, the switch is open and no current is circulating in the circuit. When the switch is closed, the capacitor begins to discharge through the resistor R_d. The value of R_d is equal to that of the effective resistance of the diode in conduction, i.e. with a voltage applied to the ends greater than V_{bd}. The time required for discharge is, therefore,

$$\tau_s = R_d \cdot C_d. \tag{3.18}$$

As the voltage applied to C_d decreases, the current flowing through the quenching

resistor R_q tends to the asymptotic value of [43]:

$$I_d = \frac{V_{bias} - V_{bd}}{R_q + R_s}. \tag{3.19}$$

If the value of R_q is high enough, the avalanche multiplication process is stopped. This is equivalent to reopening the switch in the circuit, resulting in charging the capacitor C_d to the voltage V_{bias}. The time required for charging is, therefore,

$$\tau_c = R_q \cdot C_d. \tag{3.20}$$

What has been discussed so far is equivalent to a SiPM consisting of a single microcell. In fact, SiPMs consist of an array of independent microcells connected in parallel. Each cell consists of a SPAD photodiode, with a common output, in series with a quenching resistor, as depicted schematically in Fig. 3.16.

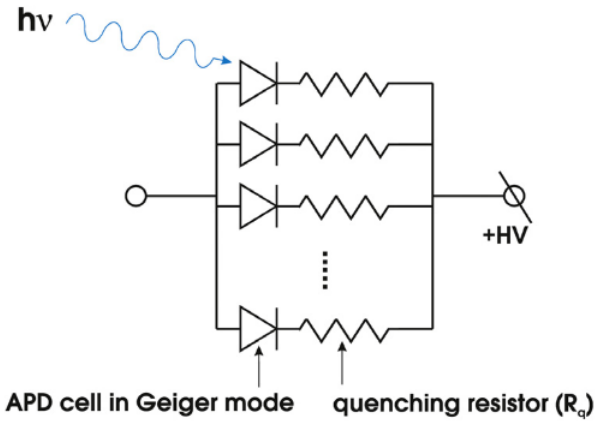

Figure 3.16: SiPM circuit diagram. A SiPM consists of photodiodes, in series with resistors, placed in parallel [46].

The rise time of a SiPM is determined by the rise time of the avalanche formation, while the recovery time of the sensor, which is equal to the time in which the pulse decays, is determined by the charging time of the microcells.

Since the capacity of the microcell depends on its area, the recovery time varies with the size of the microcell. In fact, the recovery time increases as the microcell side of the SiPM increases. The recovery time depends also on the value of the quenching resistance, which increases by decreasing the temperature. The microcells can still activate during the recovery time before the overvoltage has returned to its nominal value, but the gain (defined in Sec. 3.4.4) will be reduced in proportion to the reduction in overvoltage.

The sensor outputs a photocurrent, and the total charge Q generated by an event is given by

$$Q = N_{fired} \cdot G \cdot e, \tag{3.21}$$

where N_{fired} is the number of activated microcells, G is the gain and e is the electron charge. The total charge is also equal to the integral of the photocurrent pulse [41].

3.4.3 Photon counting

The photoelectric spectrum of a SiPM consisting of a large number of pulses is shown in Fig. 3.17. In fact, each input corresponds to the digitally converted released charge measured by integrating the peaks of the electric current during a predefined time interval. Each spike corresponds to a different number of microcells in the SiPM affected at the same time. The peaks are sharply separated, and the probability of their occurrence depends to the first order on changes in light intensity. Looking at the histogram, it can be seen that the first peak corresponds to having no photons detected. In addition, the width of the first peak indicates the noise value of the system, since it represents random fluctuations in the output signal in the absence of stimuli. The histogram represented has the first peak width $\sigma_0 = 29 \pm 1$ counts of ADC. The second peak represents the event in which only one photoelectron is absorbed and it is instead $\sigma_1 = 38.1 \pm 0.4$ counts of ADC wide. So, the second peak is much wider than the first one. In fact, although the homogeneity of the SiPM cell response is high, the more cells that are hit the wider the peaks increase with the square root of the number of cells hit, thus going to limit the maximum number of resolvable peaks [47].

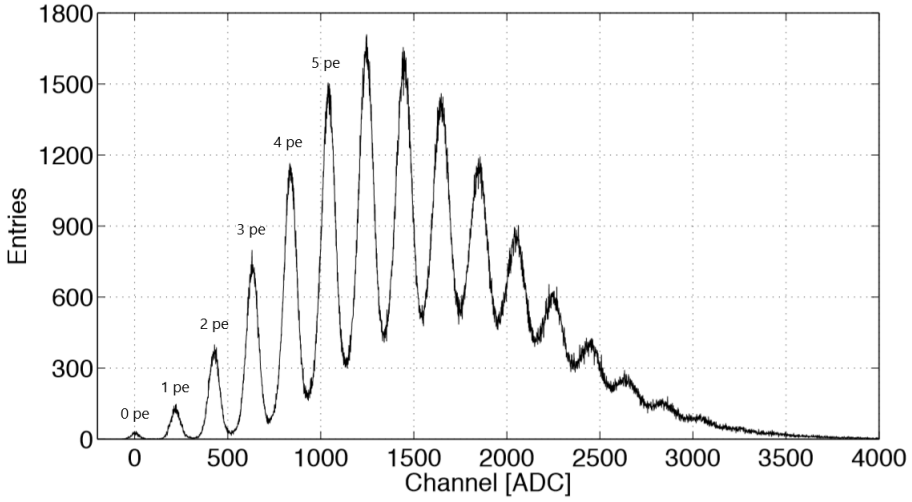

Figure 3.17: Photoelectric spectrum of a Hamamatsu MPPC S10362-11-100C obtained by using an LED as a light source at the bias voltage of 70.3 V *and temperature of* 25 °C*. Each peak corresponds to a certain number of photoelectrons [47].*

3.4.4 Gain

The gain of a SiPM is defined as the amount of charge generated when a photon is revealed and depends on the overvoltage and the size of the individual cells in the SiPM, as is shown in the example in Fig. 3.18. Whenever an avalanche is generated from an absorbed photon in the active volume, each cell emits quantized and uniform charge.

The gain of a single cell of a SiPM is calculated as the ratio of the charge

generated by the activated cell to the charge of the electron and is thus given by

$$G = \frac{C \cdot \Delta V}{e}, \tag{3.22}$$

where C is the capacitance of the diode, $\Delta V = V_{bias} - V_{bd}$ is the overvoltage, finally e is the elemental charge.

Thus, the gain of a single cell increases linearly proportional to ΔV. In general, V_{bd} depends on temperature and consequently the gain also depends on it [47].

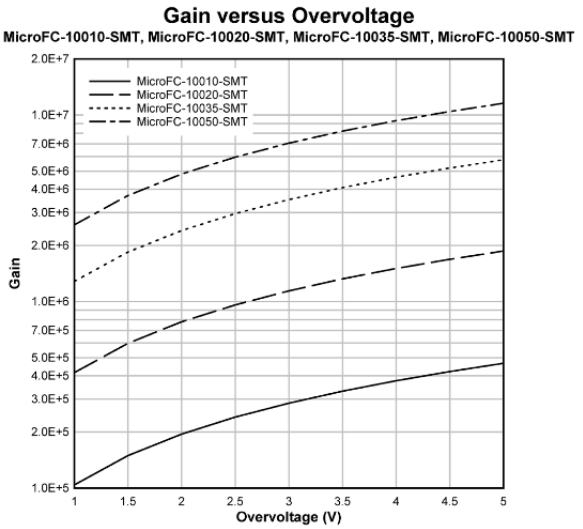

*Figure 3.18: Gain as a function of overvoltage for different microcell sizes (*10 μm, 20 μm, 35 μm *and* 50 μm*) [48].*

The gain of a SiPM is given by the distance between the abscissae of two consecutive peaks in the photoelectric spectrum. Thus, in practice one way to calculate it is to average the distance between the abscissa of consecutive peaks.

3.4.5 Breakdown voltage and gain dependencies on temperature

At cryogenic temperatures, SiPMs have different performances in terms of breakdown voltage, gain, noise and pulse shape. Several studies have been conducted in this regard and, for example, it is possible to compare some models of SiPM manufactured by AdvanSiD, SensL and Hamamatsu [53]. Temperatures from 87 K up to 300 K were scanned. Focusing in particular on the temperature of liquid argon (87 K) and liquid xenon (165 K), since they are scintillating materials which are used in several physics experiments.

All the tested SiPM models show a reduction of the breakdown voltage by lowering the temperature, as shown in Fig. 3.19, but with different coefficients. It can be seen that that the breakdown voltage temperature coefficient decrease less at lower temperatures than at higher temperatures [53].

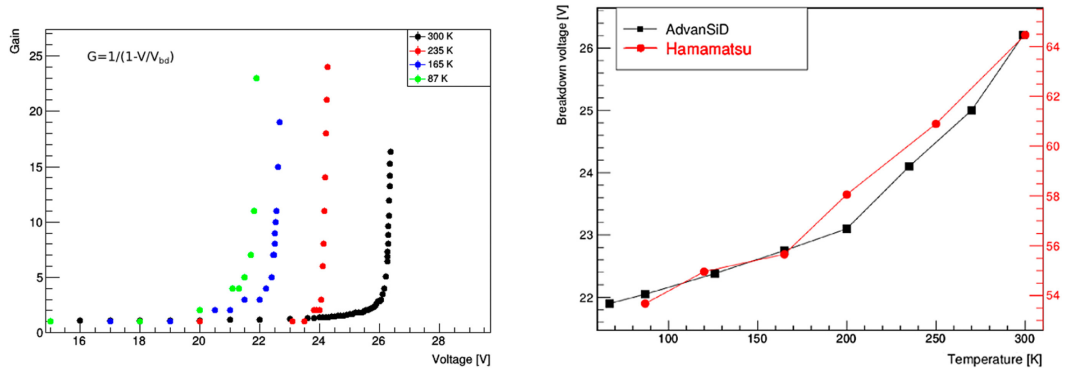

Figure 3.19: Left, I–V curves at different temperatures for AdvanSiD NUV model. Right, breakdown voltages as a function of the temperature for AdvanSiD (black squared) and Hamamatsu (red circles) models [53].

The charge distribution spectrum and the gain measurements are displayed in Fig. 3.20 The distance between two consecutive peaks of the charge distribution provides the gain of a device. One that the variation of the gain at cryogenic temperature with respect the value measured at room temperature is below 7%.

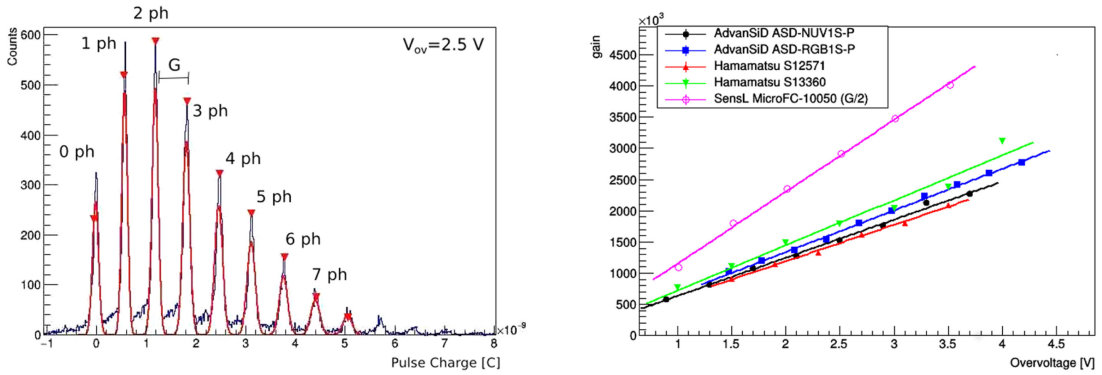

Figure 3.20: Left, charge distribution of a SiPM. Right, gain measured for each device as a function of overvoltage at 87 K [53].

3.4.6 Photon detection efficiency

An important parameter is the efficiency with which photons with a given wavelength are detected. For a SiPM, the Photon Detection Efficiency (PDE) can be expressed as [41]

$$PDE(\lambda, V) = \eta(\lambda) \cdot \epsilon(V) \cdot FF, \tag{3.23}$$

where $\eta(\lambda)$ is the quantum efficiency of the silicon, i.e. the probability of generation of an electron-hole pair as a result of an incident photon, $\epsilon(V)$ is the probability of an avalanche starting, and FF is the fill factor, i.e., the ratio of the light-sensitive area to the total area of the device. FF is less than 1 because of the space between the individual cells of the SiPM, but it is generally greater than 0.7-0.8.

Since $\eta(\lambda)$ is constant for a given wavelength of a light source and FF is constant for a given SiPM, it is concluded that the PDE of a single device depends only on

$\epsilon(V)$ and is thus a function of the overvoltage V. An example of the dependence of the PDE of a SiPM on wavelength and overvoltage is shown in Fig. 3.21.

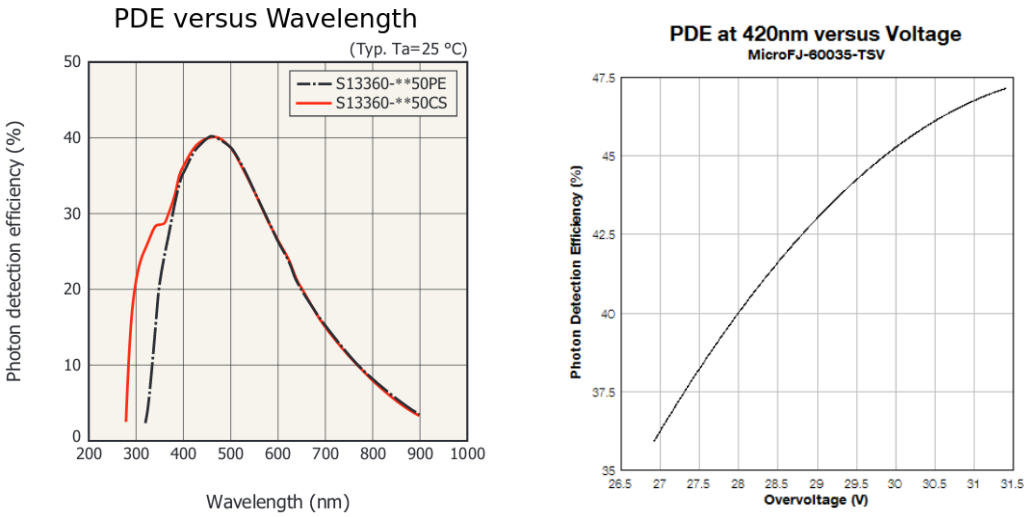

Figure 3.21: Left, PDE as a function of wavelength for a SiPM with cells of 50 μm *[50]. Right, PDE as a function of overvoltage for a SiPM of* 6 mm *with cells of* 35 μm *[41].*

Quantum efficiency

Quantum efficiency represents the probability for a photon to generate an electron-hole pair in the active region of the device. It is given by the product of the transmittance of the dielectric layer on the silicon surface and the internal quantum efficiency. Both terms depend on the wavelength. The first term can be maximized by adding an anti-reflective coating, while the second term represents the probability for a photon that has passed through the dielectric layer to generate an electron-hole pair in the active region. In an n+/p/p+ diode, the active layer is approximately bounded at the top by the ungated n+ layer, while at the bottom it is bounded by the p+ layer used for ohmic contact or, in the case of overlapping substrates, by the highly doped substrate. In fact, when a pair is generated in those regions, there is a high probability that an electron and a gap will recombine due to Auger or Shockley-Read-Hall (SRH) processes [43].

Trigger probability

When charge carriers travel through the high electric field region, they have a finite probability of generating an avalanche. In the case of a photon generation event, two charge carriers traveling in the opposite direction are created. Taking both contributions into account, the total trigger probability is given by [43]

$$P_t = P_e + P_h - P_e \cdot P_h, \tag{3.24}$$

where P_e and P_h are, respectively, the probability for electrons and the probability for holes to cause the breakdown.

The physical meaning of this equation can be understood if we consider an n+/p junction with a region of a constant high electric field. Looking at the probability

trend as a function of depth depicted in Fig. 3.22, it can be seen that if a pair is generated in the left part of the region where the electric field is intense, the electron is directly collected on the n+ electrode and does not contribute to the trigger probability. Instead, the gap must pass through the entire region that has the intense field and thus its probability of trigger is maximal and $P_t = P_{hM}$. In case of photon generation in the right side, the situation is symmetric and only electrons contribute to the probability of trigger, so $P_t = P_{eM}$. In the central region, the value of P_t is instead between P_{eM} and P_{hM}.

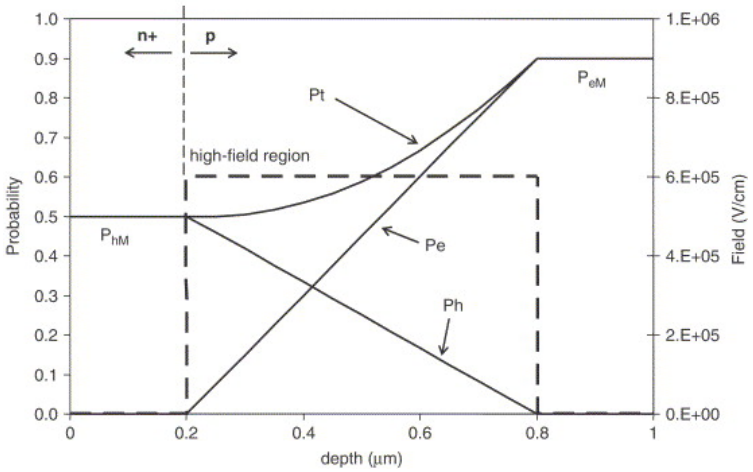

Figure 3.22: Probability of triggering an avalanche as a function of the depth at which a photon is generated [43].

In order to maximize the probability of trigger, it is necessary for photon generation to occur at the p-side of the junction so that electrons pass through the region with high electric field. In addition, the V_{bias} must be high.

Geometric efficiency

The ratio of active area to total device area is a critical issue in SiPMs. Each SiPM cell is surrounded by a region that is not sensitive to light signals formed by the structure that partially optically isolates the cells. Considering that the area of a cell can be very small, even a few μm of nonsensitive region around the cell can have a very detrimental effect on geometric efficiency.

3.4.7 Noise

The performance of SiPMs is determined by detection efficiency and noise, originating from charge carriers, not generated by photons, that produce a discharge called secondary avalanche. These secondary discharges are mainly due to three phenomena: *dark counts*, *optical cross-talk* and after-pulses. These phenomena occur stochastically and introduce fluctuations in the measurement processes.

Dark Counts

The signals are not only produced by photon-generated charge carriers, but also by thermally generated charge carriers. The signals produced by the latter are called dark pulses because these discharges occur randomly and independently of illumination. The dark pulses are observed together with the normal signals, but they cannot be distinguished from them by their shape and thus cause errors in detection. The dark pulses constitute the cause of primary noise, since the avalanche discharges are not due to photons actually absorbed by the sensor.

The number of dark pulses observed is called the dark count rate, defined as the number of signals that are generated in the absence of a light source and exceed the threshold of 0.5 photoelectrons. Since the dark pulses are produced by thermally generated charges, the dark count rate varies with the temperature of the SiPM. The dark count rate shows the following behavior [52]:

$$N_{0.5} \propto T^{\frac{3}{2}} \exp\left(\frac{E_g}{2kT}\right), \tag{3.25}$$

where T is the absolute temperature expressed in K and E_g is the energy of *gap*, of value about 1.1 eV for pure silicon. When the gain is fixed at a constant value, the dark count depends linearly on the temperature.

The rate of thermal generation and recombination of charge carriers in the forbidden band can be described by the Shockley-Read-Hall (SRH) equation [51]:

$$G = \frac{n_i^2 - pn}{\tau_{e0}\left(p + n_i \exp\left(-\frac{E_t - E_0}{kT}\right)\right) + \tau_{h0}\left(n + n_i \exp\left(\frac{E_t - E_0}{kT}\right)\right)}. \tag{3.26}$$

Generation and recombination processes occur when in a semiconductor the product pn differs from its equilibrium value n_i^2. In the equation, n_i is the intrinsic concentration of carriers in the semiconductor, E_0 is the Fermi level of the material, E_t is the energy level of the capture center, and τ_{e0} and τ_{h0} are the recombination times for electrons and holes, respectively, defined as:

$$\tau_{i0} = \frac{1}{v_{th}\sigma_i N_t}, \qquad i = n, p; \tag{3.27}$$

where σ_i is the capture cross section for electrons ($i = n$) or holes ($i = p$), N_t is the concentration of capture centers, and v_{th} is the thermal velocity given by

$$v_{th} = \sqrt{\frac{3kT}{m^*}}, \tag{3.28}$$

with m^* effective mass of the electron or gap. In the depletion region, p and n are very low and the generation rate can be approximated by:

$$G = \frac{n_i}{\tau_{e0} \exp\left(-\frac{E_t - E_0}{kT}\right) + \tau_{h0} \exp\left(\frac{E_t - E_0}{kT}\right)} = \frac{n_i}{\tau_{g0}}, \tag{3.29}$$

where τ_{g0} is called the generation time and describes the rate of electron-hole pair formation in the depletion region. If E_t is approximately equal to E_0, then the

generation time is of the same order of magnitude as the recombination times. In contrast, if E_t is very different from E_0, τ_{g0} can be much larger than τ_{e0} and τ_{h0} [51].

Besides being due to charge carriers that are thermally generated, the background noise in SiPMs may also be due to charge carriers generated by tunneling effect. The generation of electron-hole pairs depends on the voltage applied to the SiPM. As the voltage increases, the electric field strength increases and, as a result, the tunnel effect is more likely to occur; therefore, the frequency of generation increases. The dark count rate increases linearly with the overvoltage, as shown in the example in 3.23. The dark count can be considered statistically independent.

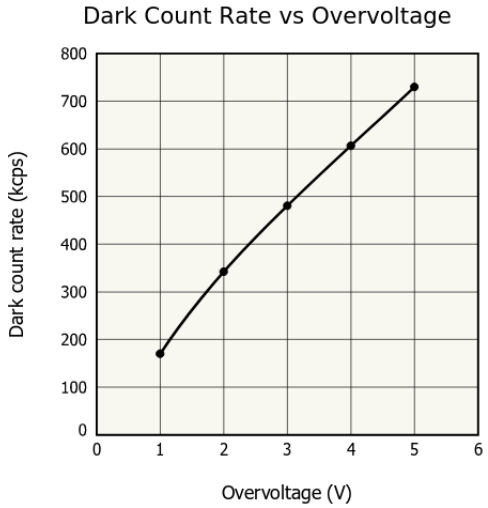

Figure 3.23: Dark count rate as a function of overvoltage for a SiPM of 3 mm *with cells of* 50 μm *[50].*

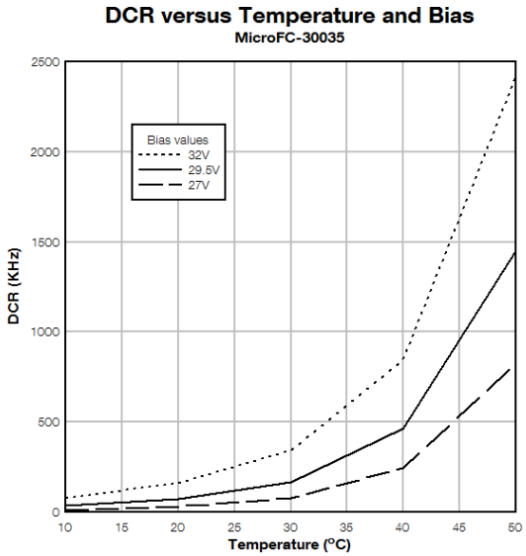

Figure 3.24: Dark count rate of a SiPM as a function of temperature for different values of bias voltage [48].

Different noise sources result in different temperature dependencies. In fact, as shown in Fig. 3.24, three zones with different temperature dependencies of the dark count rate can be distinguished based on the main contribution made to the noise. At low temperatures the noise is mainly due to the tunneling effect, then a zone can be distinguished in which SRH generation processes dominate, while for higher temperatures diffusion prevails.

The DCR further decrease for cryogenic temperatures, as it is shown in Fig. 3.25.

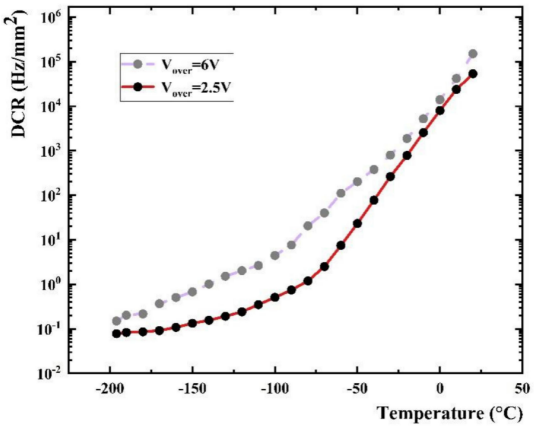

Figure 3.25: DCR vs temperature, for the overvoltage values of 2.5 V *and* 6 V *[49].*

Furthermore, large differences can be seen in the noise at 87 K depending on the SiPM model. The Dark Count Rate (DCR) was measured both at room temperature and at a cryogenic temperature in function of the overvoltage, as shown in Fig. 3.26. At 87 K, the DCR is reduced for the AdvanSiD RGB, while AdvanSiD NUV and Hamamatsu models show high DCR by rising the overvoltage. This effect is due to an increase of correlated noise [53].

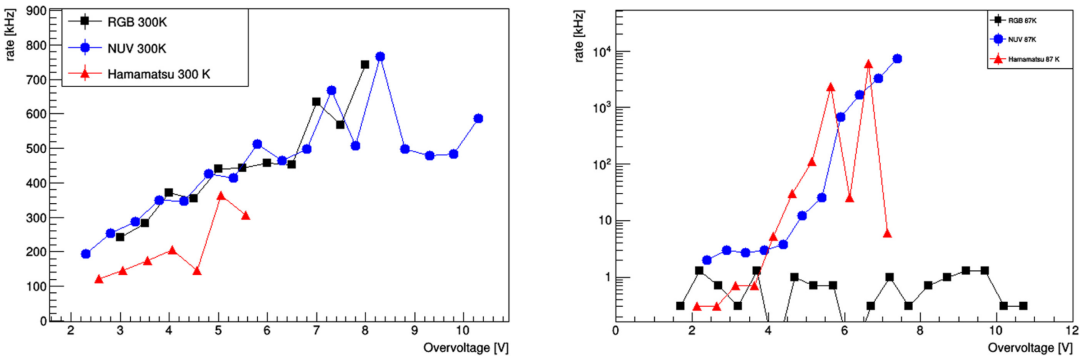

Figure 3.26: DCR of the different models both at 300 K (left) and at 87 K (right) [53].

Optical Cross-Talk

Pulses corresponding to two or more photoelectrons may be observed when photons generated during an avalanche activate secondary discharges that may involve the

same or neighboring cells. If the phenomenon involves neighboring cells, then it is named Optical Cross-Talk (OCT). The signal corresponding to OCTs cannot be distinguished from the signal of the initial photon, which leads to a greater uncertainty regarding the photon count of the SiPM, since it is impossible to know how many cells are activated by this effect. The probability of having OCT is therefore an important parameter of a SiPM and must be minimized. OCTs are one cause of correlated noise, since secondary discharges are related to a primary event, which can be either real or noise. OCTs can manifest in three different ways. The first possibility is that they occur directly, when an emitted photon generates a charge carrier in the active region of a nearby cell. Then, a secondary avalanche is produced coincident with the first one. OCTs can also occur late, when the photon is absorbed by the non-depletion region. In this case, a charge carrier capable of reaching the active scattering region is generated, but because of the slowness of the process, the secondary avalanche will lag behind the first one. The last way OCTs occur is externally, when the emitted photon tries to exit the device, but is reflected by structures placed on it.

The number of OCTs depends mainly on the size of the cells, the voltage applied to the cells, and the gain. The probability of having OCT can be measured as the ratio of the number of signals generated in the dark that exceed the threshold of 1.5 photoelectrons to the threshold of 0.5 photoelectrons [52]

$$OCT = \frac{N_{1.5}}{N_{0.5}}. \tag{3.30}$$

Small cells have greater OCT than large cells. In fact, if the cells are large, photons must travel longer average distances to reach neighboring cells and cause secondary avalanches. In Fig. 3.27 is shown an example of the dependence of the probability of having OCT as a function of SiPM gain for three sensors of different sizes. In modern SiPMs, gaps are placed between cells to have electrical and optical isolation, at least partially.

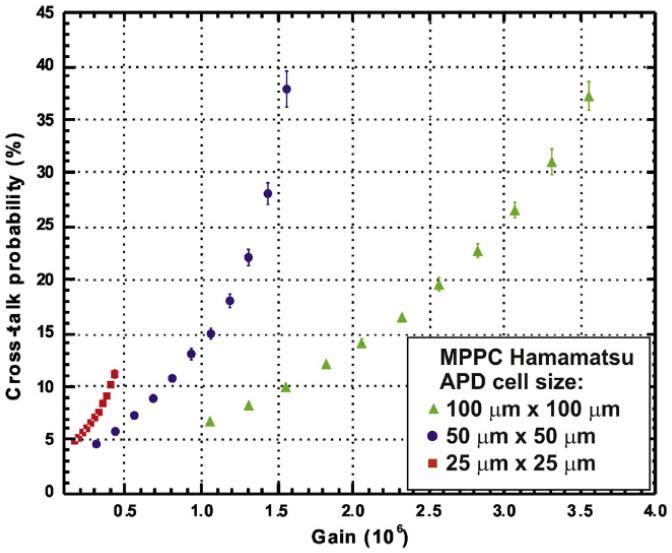

Figure 3.27: OCT probability as a function of SiPM gain for 3 different sensor types [46].

After-Pulses

The charge carriers of an initial avalanche can become trapped by silicon impurities. After a delay time of the order of a few nanoseconds it may happen that these trapped charges are released and generate secondary avalanches in the same cell. Avalanches generated in such a manner are named after-pulses. An example of signals due to after-pulses is shown in Fig. 3.28. The after-pulses, together with the OCTs, cause the correlated noise, although the secondary discharges due to the OCTs involve adjacent cells, while those due to the after-pulses involve the same cell where the primary discharge occurred. If the after-pulses have a short delay time, shorter than the cell recovery time, then they produce negligible effects on the measurements since they are triggered when the SiPM cells are not fully charged. In contrast, after-pulses with delay time greater than the cell recovery time affect the measured values. The after-pulses depend on the sensor technology and it is crucial to take them into account in experiments related to photon correlation since their presence can alter the measurements [52].

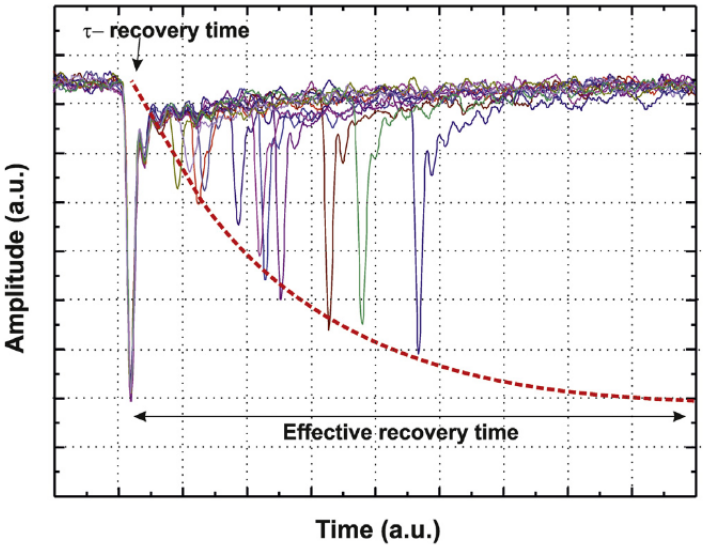

Figure 3.28: After-pulses with different delay times [46].

3.4.8 SiPM response

If the number of incident photons is much less than the number of cells, the response of the SiPM is linear. This means that the number of activated cells is proportional to the number of incident photons, as is shown in Fig. 3.29. The range of light intensity values within which the response of the SiPM is linear is called the dynamic range of the SiPM. An increase in incident intensity corresponds to an increase in output current.

The dynamic range of the SiPM is a function of the number of cells in it and the PDE, thus the overvoltage and the wavelength of the incident radiation [52]. If the number of incident photons increases, it may happen that two or more photons are absorbed by the same SiPM cell. This is because the greater the intensity of the incident light, the greater the probability that a second photon will be absorbed by

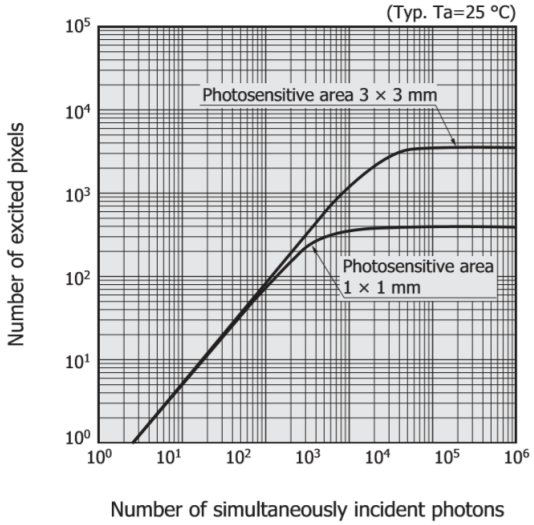

Figure 3.29: Number of activated cells as a function of the number of simultaneously incident photons in logarithmic scale. The dynamic range for simultaneously incident photons can be observed. The pitch of the cells is equal to $50\,\mu$m *[52].*

a cell before it terminates the avalanche process already in progress. Even if two or more photons are absorbed by the same cell, after an avalanche discharge has occurred, it is not possible for another one to occur in the same cell until the bias voltage is reestablished by the quenching resistor. If the next photon is revealed before the cell has fully recharged, there will be an output pulse with amplitude that varies according to the charge level, so it may be much smaller. Overlapping output pulses lead to errors in photon counting and worsen the linearity of the output signal as the number of incident photons increases. Thus, in case where the number of incident photons is comparable to the number of cells or greater, a nonlinear response will result.

If the photons are considered to be well distributed among the cells, it becomes possible to describe the behavior of the SiPM with a Poisson distribution. In fact, by defining the mean value of the distribution as

$$\lambda = \frac{N_{photon}}{N_{total}} \cdot PDE, \tag{3.31}$$

where N_{photon} is the number of incident photons, which is multiplied by the PDE (Photon Detection Efficiency), while N_{total} is the number of cells in the SiPM; the probability of having n interactions in a cell can be calculated as

$$P(n) = \frac{e^{-\lambda}\lambda^n}{n!}. \tag{3.32}$$

Therefore, the number of fired cells N_{fired} is

$$N_{fired} = N_{total}(1 - P(0)) = N_{total}(1 - e^{-\lambda}), \tag{3.33}$$

where $P(0)$ is the probability of no interactions. The number of fired cells can then be rewritten as

$$N_{fired} = N_{total} \cdot \left(1 - \exp\left(-\frac{PDE \cdot N_{photon}}{N_{total}}\right)\right), \tag{3.34}$$

For the dynamic range, however, it is possible to approximate this expression and obtain

$$N_{fired} = N_{photon} \cdot PDE. \tag{3.35}$$

3.5 ALCOR ASIC

Signals from the SiPMs in cryogenic environments need to be amplified and read out. In the GRAIN detector, a mixed-signal ASIC will be used. However, such ASIC must be able to read numerous SiPMs' channels at cryogenic temperatures, but not many of them have these characteristics. This is the reason why it is being investigated the possible use of the ALCOR (A Low Power Chip for Optical sensors Readout) ASIC [54], which is capable of reading out SiPMs at cryogenic temperatures, while presenting some limitations, in particular the small number of channels per link.

The ALCOR is a low-power, mixed-signal ASIC implemented in 110 nm CMOS technology, which integrates 32 independent pixels, arranged in a 4×8 matrix. Each pixel includes signal amplification circuitry, discriminators and quad-buffered analogue interpolation TDCs with a time binning down to 25-50 ps. The chip time-based readout supports both time of arrival and Time-over-Threshold (ToT) measurements, with a fully digital output.

3.5.1 ALCOR ASIC's architecture

ALCOR is a mixed-signal ASIC optimized for the readout of SiPMs at cryogenic temperatures. The 32 pixels of ALCOR have dimension of about 500 µm × 500 µm, while the full chip area is 4.95 mm × 3.78 mm.

The 32 pixels are grouped into 4 sectors, each with 2 columns. The pixels in each sector share the same Bias Configuration Registers (BCR), which define the analog bias references of the pixels, and the End of Column Configuration Register (ECCR), which defines some operating parameters. Each pixel has four dedicated Pixel Configuration Registers (PCR) to define pixel operation and settings. The pixel architecture is shown in Fig. 3.30.

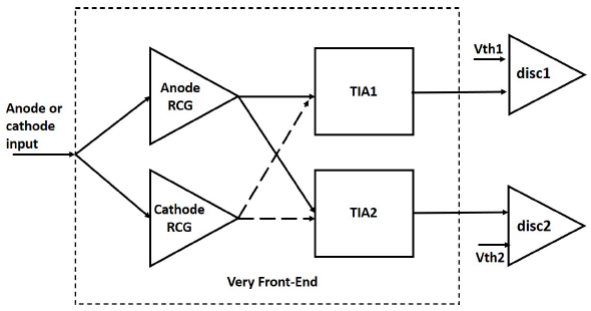

Figure 3.30: Pixel architecture.

Each pixel is equipped with a low-impedance dual-polarity front-end based on a Regulated Common-Gate (RCG) structure that allows it to read SiPM anode

or cathode signals. The amplified signal is sent to two independent branches with programmable gain, each of which is coupled to a leading-edge discriminator with configurable threshold. The two discriminators are used for timing measurements, to reject pulses of low amplitude and to trigger the readout of event data. The coarse timestamp is derived from a 15-bit clock counter (160-320 MHz), while the fine timestamp information is generated using low-power TDCs based on analog interpolation. Each pixel includes four TDCs to increase the count rate capability and de-randomize the incoming photo-electrons. Data payload generated for each event is collected by the End of Column block and transmitted off-chip using 4 LVDS transmitters, one for each sector.

3.5.2 Front end

Complementary RCG (Regulated Common-Gate) circuits designed for SiPM readout make up the chip's analogue front-end. Two independent branches receive the signal from either the anode or cathode RCG, and a common source TIA (Transimpedance Amplifier) is used to transform the amplified current into a voltage signal. Each branch's TIA output stage features a 2-bit register for independently setting the gain. As a result, each branch has four gain settings accessible.

The common gate current, gain settings, and process variances all have an impact on the front-end output baseline. A standard deviation of the baseline voltage of 60 mV is expected, according to Monte Carlo simulations used to examine the change of the process parameters. To deal with this variation and mismatches between different pixels (mostly caused by the absolute value of the output resistor, $R_L = 2.7$ kΩ), a fine current is controlled by a pixel-level 3-bit DAC. With this DAC, the baseline can be changed between 150 and 200 mV.

3.5.3 Pixel operation modes

Five operation modes are available: OFF, LET (Linear Edge Trigger), two types of ToT (Time-over-Threshold) and SR (Slew Rate), which are described schematically in Fig. 3.31.

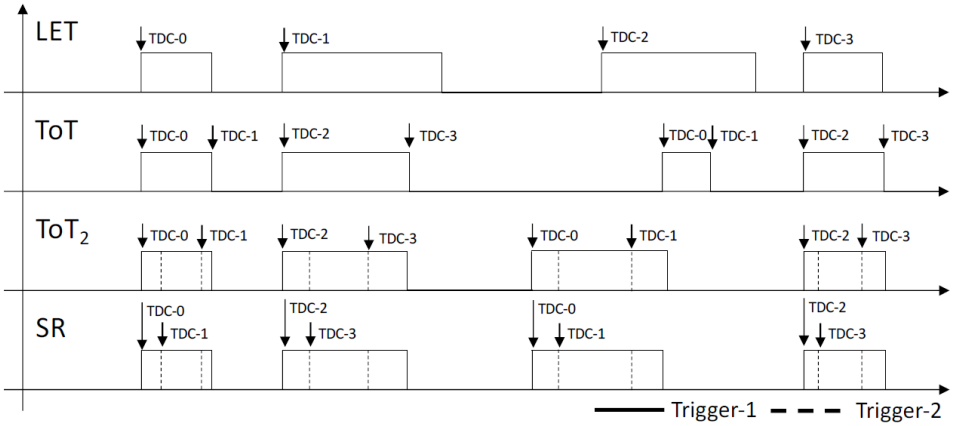

Figure 3.31: ALCOR operation modes.

OFF allows the transmission of data, but stops their production. In LET mode, a time-tag is generated on the rising edge of the trigger. Instead, in ToT mode a time-tag is generated on both the rising and falling edges of the trigger, and the ToT is equal to their time difference. The other ToT mode is similar to the first one, but it can work with two different triggers. Last, in SR mode a time-tag is generated on the first rising edge of the trigger and on the rising edge of the second trigger.

3.5.4 TDC operation

The coarse timestamp is generated from a 15-bit binary counter on-pixel and it is saved, according to the pixel operation mode, at the rising or falling edge of one of the Trg1 or Trg2 trigger signals. The system clock frequency imposes a limit on the coarse timestamp resolution. The fine time measurement makes it possible to improve the time resolution offered by the coarse counter measurement. Indeed, the time that passes between the coarse counter trigger and one of the following clock edges is measured with a time resolution of 25–50 ps.

There can be two possible case of fine time measurements, which are illustrated in Fig. 3.32.

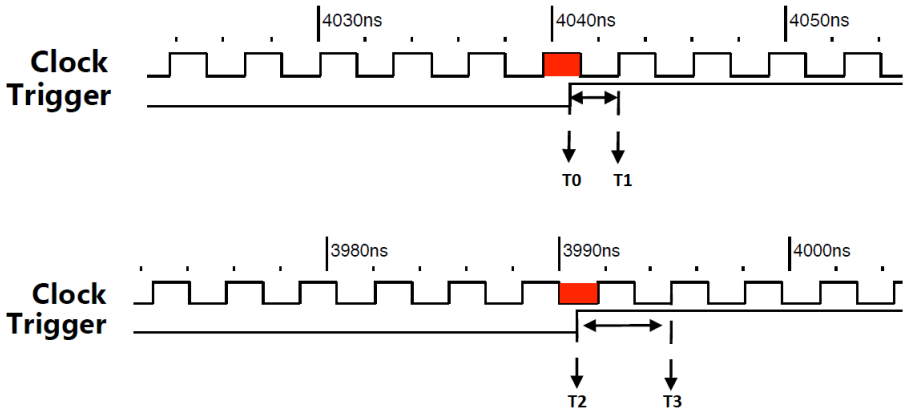

Figure 3.32: Two possible fine time measurements.

In case the trigger occurs before the clock trailing edge, the fine time measurement is assessed between the trigger time of arrival (T0) and the first subsequent clock rising edge (T1). The total timestamp will be calculated in this instance by deducting the fine time measurement from the coarse timestamp. While, in case the trigger comes after the clock trailing edge, the fine time measurement is assessed between the trigger time of arrival (T2) and the second subsequent clock rising edge (T3). The fine time measurement is being intentionally increased by one clock period in this instance, so the total timestamp will be computed as in the prior case but with the addition of one clock period.

The fine timestamp data is generated using low-power TDCs and it is based on analog interpolation, which principle of operation is displayed in Fig. 3.33.

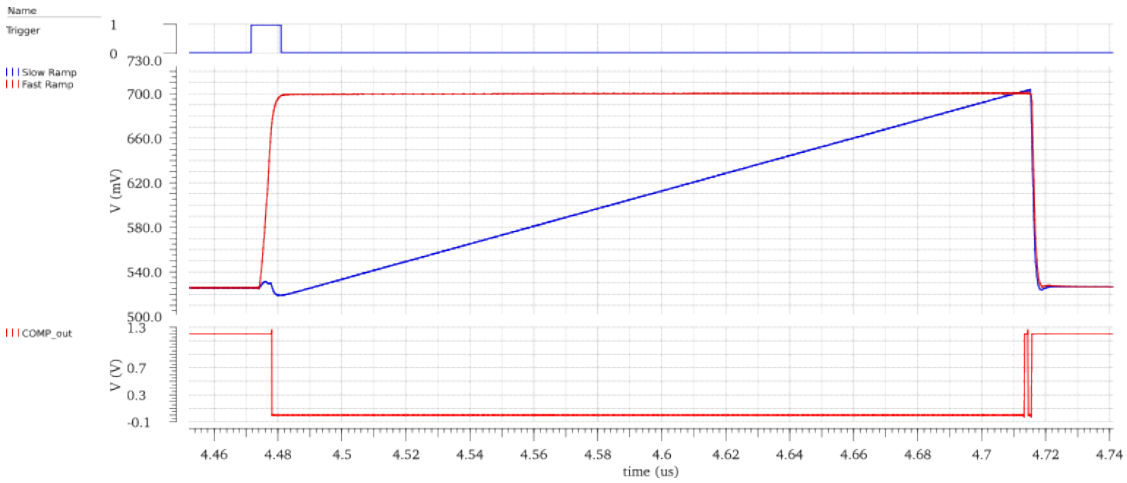

Figure 3.33: TDC principle of operation.

The circuit produces two distinct ramps by using two constant currents to recharge two identical capacitors. A fast ramp is generated using a large current. Its duration is managed by the pixel digital logic and is equal to the fine time measurement (T1 - T0). Once the recharge is finished, the voltage in the capacitor is proportional to the time that has to be measured. Subsequently, a slow ramp is generated by a smaller current, which is utilized to recharge the other capacitor until its voltage is equal to that of the first capacitor. When the two voltages are equal, a latched comparator records the time instant. Hence, the clock cycles that the slow ramp needs to reach the fast ramp correspond to the digitized fine time measurement.

A register with 8 bits is enough to represent this digital value. However, operation at a cryogenic temperature or other inconsistencies could result in an offset. In order to deal with this situation, an additional bit can be added by using the Safe Bit setting.

Time measurement

The data from both coarse counter and fine counter are combined for each event to compute a complete timestamp with 25-50 ps as time resolution.

The TDC time bin is evaluated as

$$LSB = \frac{\tau_{clk}}{T_{max} - T_{min}}, \tag{3.36}$$

where T_{min} and T_{max} are the TDC fine counter minimum and maximum values, extracted from calibration. τ_{clk} is the system clock period.

The event timestamp is then computed as

$$T = \begin{cases} (T_{coarse} \cdot \tau_{clk}) - (T_{fine} - T_{min}) \cdot LSB, & \text{if } T_{fine} \leq T_{cut}, \\ (T_{coarse} \cdot \tau_{clk}) - (T_{fine} - T_{min}) \cdot LSB + \tau_{clk}, & \text{if } T_{fine} > T_{cut}, \end{cases} \tag{3.37}$$

where T_{coarse} is the value of the 15-bit coarse counter, T_{fine} is the value of the 9-bit fine counter and $T_{cut} = (T_{max} - T_{min})/2$ is a parameter used to establish if the asynchronous event was triggered during the active or inactive phase of the clock.

3.5.5 Data format

Data words are encoded by the ALCOR ASIC according to a specific format. The data stream includes also comma words, which are 8b/10b embedded symbols and they provide additional information.

Through the ECCR dedicated bit, the insertion of status words in data outputs can be disabled. Additionally, the End of Column can operate in raw data mode, in which only data are transmitted to the serializer, without any header, frame count, status or CRC values.

Event words

Depending on the operation mode chosen, the chip generates a 32-bit data word for each event triggered by the discriminators. The pixel generates an event word containing the position tag (identified by a Column ID and a Pixel ID), the TDC ID which carried out the fine time measurement and the timestamp, represented by a Coarse counter and a Fine counter.

The position tag also specifies the SiPM from which the event has been detected because each pixel can read just one SiPM sensor. The 2 bits that are used for the ID of the TDC which generated the fine time identify the edge (rising/falling) of the trigger when the pixel operates in TOT/TOT2 mode, or the trigger (Trg1/Trg2) when in SR mode.

Frame words

Event words are arranged into frames together with other special words, to avoid uncertainties in the time reconstruction. A frame corresponds to a full cycle of the coarse counter, i.e. 215 clock cycles (102.4 µs). This corresponds to a frame rate of approximately 9.77 kHz.

A frame header word (0x1C1C1C1C) and a 16-bit frame number word are used to identify each frame. The coarse counter rollover header word (0x5C5C5C5C) signals the end of each frame and is followed by other special words (status words, CRC). A new frame can then be transmitted.

CRC

A 32-bit Cyclic Redundancy Check (CRC) code is appended to each frame to confirm the data's integrity after the serial link. A CRC header word (0x9C9C9C9C) always comes before the CRC word.

The CRC is the reminder of the polynomial long division between the message and a generator polynomial. The polynomial form used has an hex value of 0x82608EDB and it is the CRC32 used in Ethernet communications. The data integrity is verified by a receiver applying the same algorithm to the message and the received CRC code. In case of no errors, the result of the computed CRC should be 0. The End of Column circuit updates the CRC code with every transmitted data and comma words. However, the only exception is the idle comma, since is inserted after the output FIFO. The CRC code is initialized at 0xFFFFFFFF at the beginning of a transmission when a new computation starts.

Status words

The End of Column controller can add to each frame extra data regarding the number of lost events, including data from the pixels and the EoC FIFOs. Each sector has a total of 9 status words: one for each of the 8 pixels that make up each of the two columns and one for the End of Column. They are always preceded by a Status header word (0x7C7C7C7C).

3.5.6 Test pulse

Each pixel has a test pulse injection circuit that enables the injection of a user-defined charge at the input of the pixel front-end. Therefore, it is possible to evaluate the response of the pixel even when it is not connected to any sensors. This circuit only works with front-end devices with negative polarity and injects a charge equal to

$$Q_{inj} = I_{cal} \cdot \Delta T, \tag{3.38}$$

where I_{cal} is the current generated in the EoC bias region and is defined by four bias configuration registers, while ΔT is the duration of the external digital test-pulse.

Chapter 4

Development of a data acquisition system for a GRAIN demonstrator

As explained in Chap. 3, GRAIN will use an innovative imaging technique to exploit the scintillation light emitted by liquid argon at 127 nm when charged particles pass through it. The challenges of the 3D reconstruction of the scintillation light using an optical system made of coded aperture masks and SiPMs were described as well. However, there are further issues linked to the readout of the SiPM matrices inside the liquid argon volume of GRAIN. Therefore, the electronics that could allow imaging in GRAIN is being investigated. For example, the possibility of using of the ALCOR, mixed-signal ASIC optimized for the readout of SiPMs at cryogenic temperatures is being considered. Independently from the chosen ASIC, the back-end electronics will instead be implemented in FPGAs outside the cryogenic environment.

Given the difficulties introduced by the innovative technique and due to the fact that the ALCOR, one of the first cryogenic ASIC prototypes, is still under study, it was necessary to proceed one step at a time. First, in order to demonstrate the feasibility of acquisitions in liquid argon, a key step was to build a prototype of the data acquisition system. Obviously, it will not be possible to use such a prototype in GRAIN due to the limitations presented, which will be discussed in Sec. 5.4.

The first prototype consists of a SiPM matrix (16×16), connected to a custom PCB board on which a single ALCOR chip has been mounted (it can accommodate up to 8 of them). This board communicates via FMC cable with a Virtex-7 VC707 FPGA on which a firmware was loaded to perform the DAQ. The readout system chain for the demonstrator is shown in Fig. 4.1.

A `C++` software has been developed to interface with the FPGA using the computer. The software exploits the IPbus protocol to configure the ALCOR registers and to read the data that are produced. Using the software, I performed some operations, such the synchronization of the links and scans of the parameters of the ASIC, to find the one that could produce a clean signal.

Subsequently, I measured the I-V characteristics of the SiPMs of the matrix, finding the breakdown voltage, to fix a working point for the voltage. Some measurements were then carried out using test pulses, first at room temperature, and then at cryogenic temperatures, by immersing the ASIC together with the photosensor inside a liquid nitrogen Dewar at 77 K. The tests allowed to verify that the

communication between FPGA and ASIC and that the digital part of the ASIC worked just fine, both at room and at cryogenic temperature.

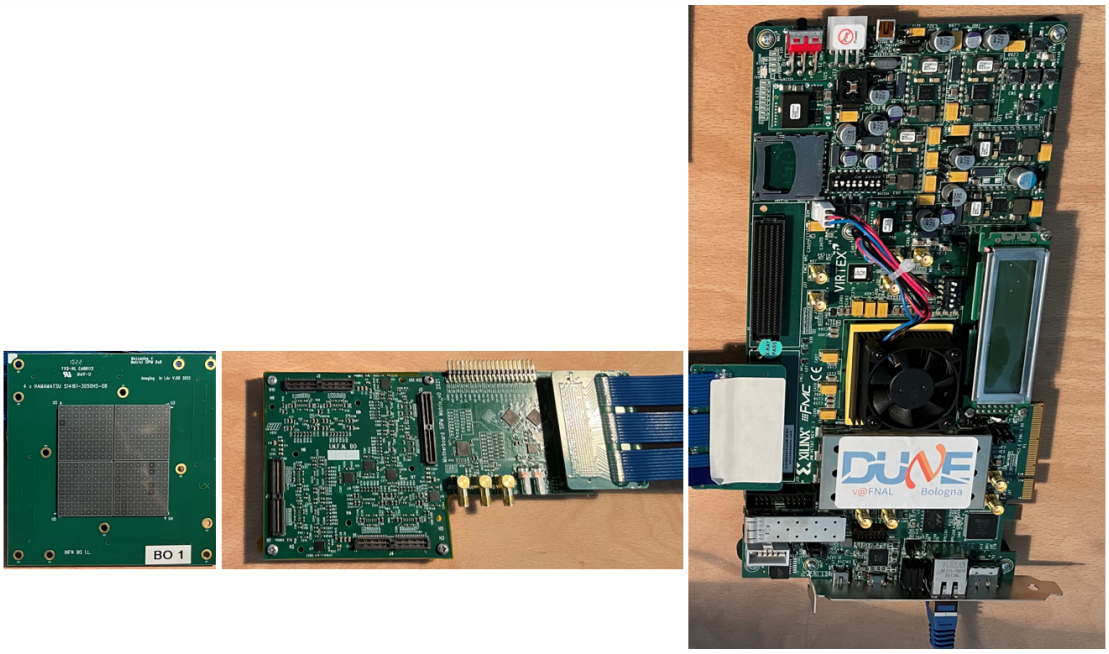

Figure 4.1: Readout system chain composed of a SiPM matrix, an ALCOR ASIC mounted on a PCB board and an FPGA, which communicates with a computer through the Ethernet connection.

The DAQ firmware needs to provide a reliable method of communicating with the ALCOR ASIC, which amplifies and digitizes the signals received by the SiPMs. In order to do so, it is necessary to read data from all the ALCOR's links and process them. It is possible to configure the ALCOR in such a way that it produces data frame, were data words are encapsulated in a specific scheme, with the addition of useful words, called comma words, which allow the user to know exactly the status of the stream and what words will arrive next.

4.1 Serial links

Data from the ASIC are transmitted sequentially, using serial communication to send data one bit at a time. To reconstruct correctly the words transmitted serially, a LVDS SerDes (Serializer-Deserializer) was implemented in the DAQ firmware. A SerDes is a serial transceiver that, on the transmitter side, converts parallel data into a serial data stream, and on the reception side, converts the serial data back to parallel.

A tap process is then used to establish the boundaries of different words and each channel is managed independently from the others. The alignment of the words is performed exploiting specific reserved words of the 8b/10b line code, which are called comma words. They present special sequences of 0s and 1s, which cannot be found in the data words. In particular, the alignment comma word (3c) can be sent continuously by the ALCOR ASIC to align the data stream. In

this case, the firmware receives the same sequence of 0s and 1s and is able to understand the point of the bit stream where it is reading. Then, it is possible to find the transition between two different words, which is of utter importance to interpret correctly the data words.

After the alignment, the words are decoded thanks to a 8b/10b decoder and can then be sent to the DAQ part of the firmware, that will process them and it will maintain just the important information. Furthermore, it is present a spy process that can be used to inspect the words both before and after the decoding. It is also possible to ignore the idle and alignment comma words, in order to be able to read just data words. This process proved very useful during the debugging phase.

Before a real ALCOR ASIC was available and it was mounted on the PCB, it was necessary to test the DAQ firmware during its development, to make sure that the SerDes and the decoding mechanism worked as expected. Therefore, I developed a VHDL emulator of the digital part of the ALCOR, which allowed the validation of the DAQ firmware.

4.2 ALCOR ASIC emulator

The ALCOR ASIC has 32 channels working independently and connected to an End of Column (EoC) controller. This design was chosen to minimize the buffer occupancy. The EoC controller performs the scan of the column in order to read only pixels which have valid stored data.

I realized a VHDL project that emulates the behaviour of an EoC of the ALCOR ASIC. The digital part of the chip consists of the pixel logic, the End of Column controller, the Double Data Rate (DDR) shift register (serial data output) and the Configuration interface (SPI interface) [55].

The data transmission is performed by a Double Data Rate shift register working at the clock frequency of 320 MHz. The provided clock should be very clean with a random jitter value of few ps RMS.

The emulator allowed me to verify the correct functioning of the initial firmware before the real ASIC itself became available. In addition, I contributed to the development of test benches in order to test the correct working of both the emulator firmware and the DAQ firmware.

4.2.1 Digital architecture

The project is divided into different entities and corresponding test benches, the main ones are: a byte serializer connected with an encoder 8b/10b, a bit serializer and a DDR output register, which all together form the End of Column (EoC). In the end, an IPbus manager entity is present to implement the mechanism which allows an user to give input data from a software application.

The main clocks that are used are a 320 MHz clock and a clock five time slower. The faster clock is the bit-clock, since the transmission of single bits is synchronous with this clock, while the slower one is called word-clock, since it is synchronous with the transmission of 8-bit and 10-bit words.

Byte serializer and encoder 8b/10b

The entity byte serializer and encoder 8b/10b emulates the encoding and the transmission of the input words. The input words have 32 bits, with attached a comma bit to distinguish between data words and comma words, i.e. control words which provide additional information on the status of the transmission. Moreover, another category of words, called status words, was introduced in the emulation to distinguish between real data words and further status words indicating the number of data losses for each channel.

This entity works with just the word-clock with period of 15.625 ns. Inside, the entity slices the 32-bit word into four 8-bit words and behaves like a parallel in parallel out shift register, giving an 8-bit word as partial output each clock cycle.

Subsequently, it encodes these 8-bit words, starting from the least significant 8 bits, into 10-bit words using an 8b/10b encoder, which follows the encoding conventions shown in Fig. 4.2. The final outputs are then encoded 10-bit words and four clock cycles are used to slice and encoding each 32-bit word.

Rules for Running Disparity

Previous RD	Disparity of code word	Disparity chosen	Next RD
−1	0	0	−1
−1	±2	+2	+1
+1	0	0	+1
+1	±2	−2	−1

3b/4b code

input		RD = −1	RD = +1	input		RD = −1	RD = +1
	HGF	fghj			HGF	fghj	
D.x.0	000	1011	0100	K.x.0	000	1011	0100
D.x.1	001	1001		K.x.1 ‡	001	0110	1001
D.x.2	010	0101		K.x.2 ‡	001	1010	0101
D.x.3	011	1100	0011	K.x.3	011	1100	0011
D.x.4	100	1101	0010	K.x.4	100	1101	0010
D.x.5	101	1010		K.x.5 ‡	001	0101	1010
D.x.6	110	0110		K.x.6 ‡	001	1001	0110
D.x.P7 †	111	1110	0001				
D.x.A7 †	111	0111	1000	K.x.7 † ‡	111	0111	1000

5B/6B code

input		RD = −1	RD = +1	input		RD = −1	RD = +1
	EDCBA	abcdei			EDCBA	abcdei	
D.00	00000	100111	011000	D.16	10000	011011	100100
D.01	00001	011101	100010	D.17	10001	100011	
D.02	00010	101101	010010	D.18	10010	010011	
D.03	00011	110001		D.19	10011	110010	
D.04	00100	110101	001010	D.20	10100	001011	
D.05	00101	101001		D.21	10101	101010	
D.06	00110	011001		D.22	10110	011010	
D.07	00111	111000	000111	D.23 †	10111	111010	000101
D.08	01000	111001	000110	D.24	11000	110011	001100
D.09	01001	100101		D.25	11001	100110	
D.10	01010	010101		D.26	11010	010110	
D.11	01011	110100		D.27 †	11011	110110	001001
D.12	01100	001101		D.28	11100	001110	
D.13	01101	101100		D.29 †	11101	101110	010001
D.14	01110	011100		D.30 †	11110	011110	100001
D.15	01111	010111	101000	D.31	11111	101011	010100
				K.28	11100	001111	110000

Figure 4.2: 8b/10b encoding conventions.

Bit serializer

After the encoder, a bit serializer, parallel in serial out shift register, is present. It works with two clocks, both the bit-clock, with period 3.125 ns, and the word-clock. It takes as input a 10-bit word and gives as output one bit of the input word at each bit-clock's edge, starting from the least significant bit.

In order to produce an output on both the edge of the bit-clock, a Xilinx's primitive ODDR (Output Double Data Rate Output Register) is used.

Then, a 10-bit word will be read in 5 complete bit-clock cycles, since the output is produced at each clock edge.

DDR shift register

The DDR (Double Data Rate) shift register puts together the byte serializer and encoder 8b/10b with the bit serializer. Accordingly, it takes as input a 32-bit word

and gives as output one bit of the sliced and encoded input word, starting from the least significant bit, as displayed in Fig. 4.3.

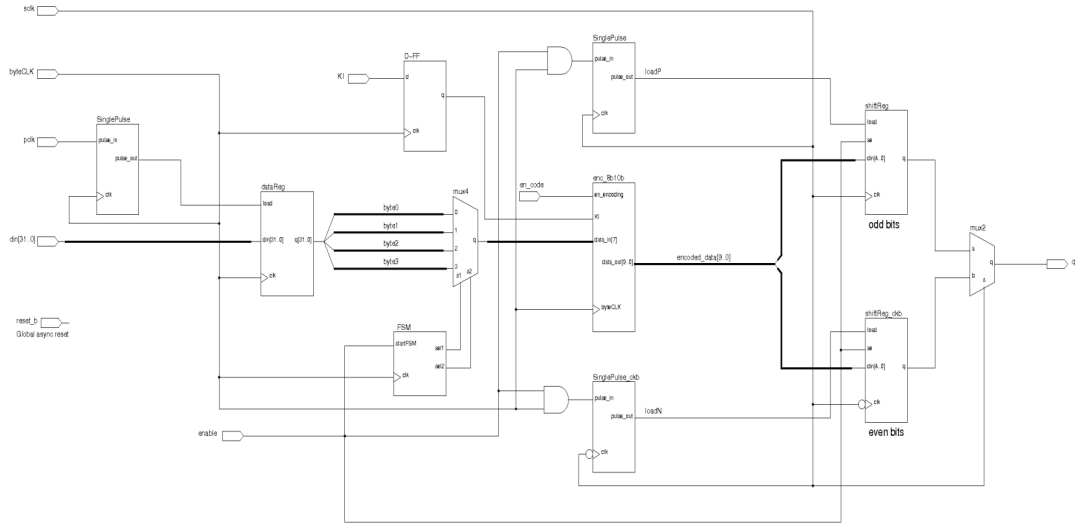

Figure 4.3: DDR register block diagram.

CDC (Clock Domain Crossing) entities are used for the synchronization of signals synchronous with different clocks, in particular for the reset and for the byte serializer output, which represents also the bit serializer input. In fact, the byte serializer output is synchronous with the word-clock, while the bit serializer input is synchronous with the bit-clock.

End of Column

The EoC (End of Column) is the top part of the emulator, it receives as input a 32-bit word from one of the 32 channels of the chip, put these data inside FIFOs, which are then passed as input of the DDR shift register, as shown in the block diagram in Fig. 4.4. However, just 8 channels are used in the case of the present emulator, since the same structure is repeated identically four times.

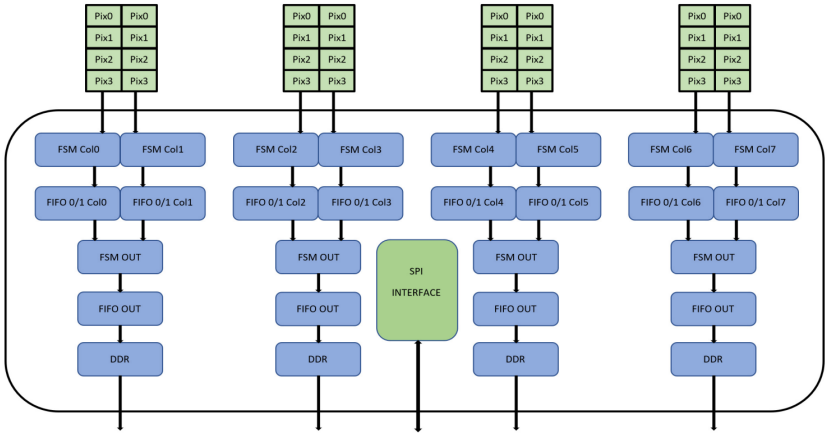

Figure 4.4: EoC block diagram.

Event Word data are encoded according to the 32-bit format displayed in Tab. 4.1.

Column ID	Pixel ID	TDC ID	Coarse counter	Fine counter
31 : 29	28 : 26	25 : 24	23 : 9	8 : 0

Table 4.1: Event words encoding.

The data stream can also contain status words which structure is shown in Tab. 4.2 and in Tab. 4.3.

Col ID	Pixel ID	Lost events	TDC0	TDC1	TDC2	TDC3	SEU
31 : 29	28 : 26	25 : 20	19 : 16	15 : 12	11 : 8	7 : 4	3 : 0

Table 4.2: Pixel status words encoding.

EoC out FIFO loss	EoC in FIFO loss	Event counts
31 : 24	23 : 16	15 : 0

Table 4.3: EoC status words encoding.

The EoC uses the information given by a control bit attached to each word to distinguish between comma, status and event words. Event words are then divided by different channel and put inside FIFOs.

There are not just event words: a mechanism is implemented to send alignment commas when requested, which are useful since they contain a fixed pattern of 0s and 1s, and, for this reason, they allow the data stream receiver to recognize the particular sequence and therefore identify the word boundaries. In addition, another mechanism sends idle commas when no new data are available. Event words are sent as input for the DDR register only if both these mechanisms are turned off.

For what concerns the event words data, I realized a Python script to generate an external file which simulates realistic data. It generates words according to the data frame produced by the ALCOR. Using a random number generator function, I made signals as the one expected from a SiPM, about 50 ns long, with the addition of a random parameter which could assume a maximum value equal to 500 ns. Furthermore, I had to consider the fact that a falling edge will arrive after the rising edge on the same channel. However, there can be different rising edges from different channels that arrive at the same time, so the association of an event can be complex. Some events were also generated close in time, to check the use of the FIFO, to store data even if they are not immediately read. Another thing to consider, was that the EoC is divided into 4 group of 8 channels each, so is probable

that an event on a channel will trigger events also in the adjacent channels. Finally, due to the dead time of the channels, is not possible to have two events on the same channel with a separation smaller than 150 ns. The file containing the simulated data frame was used for both the simulation and the implementation.

The test bench adds, then, the required comma words, which are illustrated in Tab. 4.4, both before and after the data words, following the expected data frame shown in Tab. 4.5.

Code	Hex	Use	Notes
28.0	1c	Frame header	New coarse counter frame
28.1	3c	Align comma	Forced from SPI configuration
28.2	5c	Rollover header	Coarse counter rollover
28.3	7c	Status header	Next words are status
28.4	9c	CRC header	Next word is CRC
28.5	bc	Idle comma	EoC ouput FIFO is empty
28.6	dc	Not used	Not used
28.7	fc	Do not use	Can interfere with align comma

Table 4.4: Comma words.

Position	Data
1	K28.0 (Frame header)
2	Frame number (16 bit)
3	Event words Column 0
..	Event words Column 1
n	K28.2 (Coarse Counter Rollover header)
$n+1$	K28.3 (Status header)
$n+2$	Status words Column 0 (x4)
$n+6$	Status words Column 1 (x4)
$n+10$	End of Column status word
$n+11$	K28.4 (Checksum header)
$n+12$	CRC value
$n+13$	K28.0 (New Frame header)

Table 4.5: Data stream with event words.

Random jitter with maximum value of 50 ps (as per specifications [54]) was added to each clock in the test bench to make the simulation more realistic.

For what regards the implementation of the project in a FPGA, I developed a `C++` software that contains different functions and uses the IPbus protocol to read or write the FPGA registers. Beyond the function that setup the clocks, I created some functions for the control of the EoC. In particular, one function produces internally a complete data frame, which can be sent to the EoC as input to test if

it behaves as expected. Another function is instead used to read and send to the EoC the realistic data frame generated by the Python script.

IPbus manager

The IPbus is an Ethernet-based protocol, created to read and write packet of data within FPGA hardware. The bus implementation works in such a way that the connection of several slaves requires an address decoder and logic for multiplexing the data read from the slaves to the master connection [56], referred to as bus fabric in Fig. 4.5.

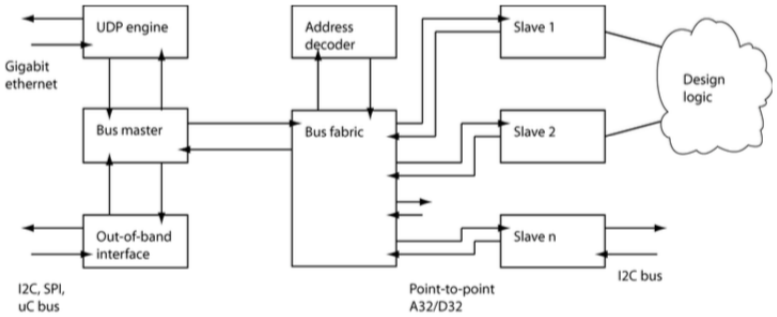

Figure 4.5: Bus topology.

The bus structure allows a slave to see activity on the bus when it is being addressed. It is therefore necessary for a slave to decode only its internal address space. The on-chip bus is fully synchronous and the firmware for each transport interface contains handshaking logic to transmit data packages over a serial digital data stream. Typically, IPbus clock has a frequency equal to 31.25 MHz.

There are only two types of bus cycles: read and write. A bus cycle begins with the master driving the address and writing a bit onto the bus, along with writing data (if necessary) and strobe assertion. The cycle ends when the slave asserts ack or err. The slave can respond on the same cycle, or may insert one or more wait states by delaying the ack or err signal. The number of wait states can be different on read and write cycles. The slave may assert ack on the same cycle as strobe for a zero wait state transaction. The master registers the data on the cycle that ack is asserted.

After the termination of the cycle, the master will either deassert strobe, or present new address or data onto the bus, and hold strobe high to signal a new cycle. An example of a write and read transaction is illustrated in Fig. 4.6.

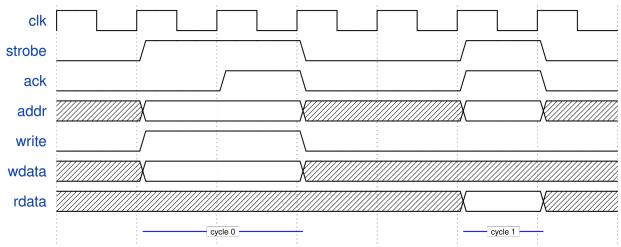

Figure 4.6: A write to a slave with one wait state is shown. The bus is idle for two clock cycles, then there is a read from a slave with zero wait states.

In the context of this project, three slaves (2 RAMs and 1 register) are used to control the EoC. The two RAMs are used for the comma control bit and the input data, whose values are then put into two FIFOs, while the register has four bits: one to force the alignment comma instead of the input word, one to enable the reading of the aforementioned FIFOs, one to reset the EoC and the last one to enable the use of the ring buffers FIFOs.

Available words from the bus are assigned to a comma and a data signals in a process. These signals are then used as output for two dual clock FIFOs. The output of the two FIFOs are inserted into ring buffer FIFOs if the flag to enable the mechanism is on. In the end, the outputs are produced when the reading of the FIFOs is enabled. Subsequently, these outputs are connected to the Xilinx OBUFDS primitive (Differential Output Buffer) which gives a differential output, since the LVDS standard was used.

A summary diagram showing the clocks, the inputs, the outputs and the main connections, is shown in Fig. 4.7.

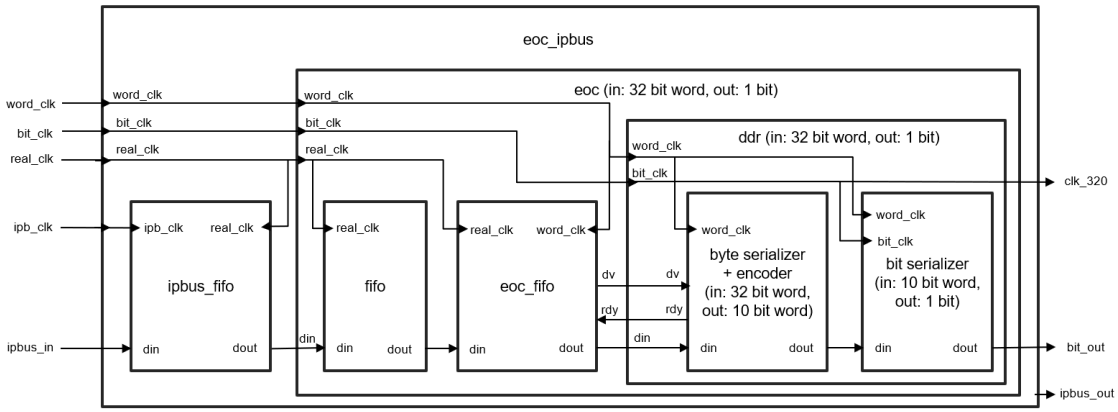

Figure 4.7: Logic scheme of the project's clocks, data inputs and outputs.

4.2.2 Usage

I used Vivado 2021.2 for simulations, synthesis and implementation of the emulator.

Simulations

Different source file can be chosen to be simulated. All of them have test benches that show their working principle and robustness.

In particular, I added a random jitter with maximum value of 50 ps, as per specifications[54], to the EoC test bench's clocks to make the simulation more realistic.

An example of a simulation of the IPbus mechanism is shown in Fig. 4.8.

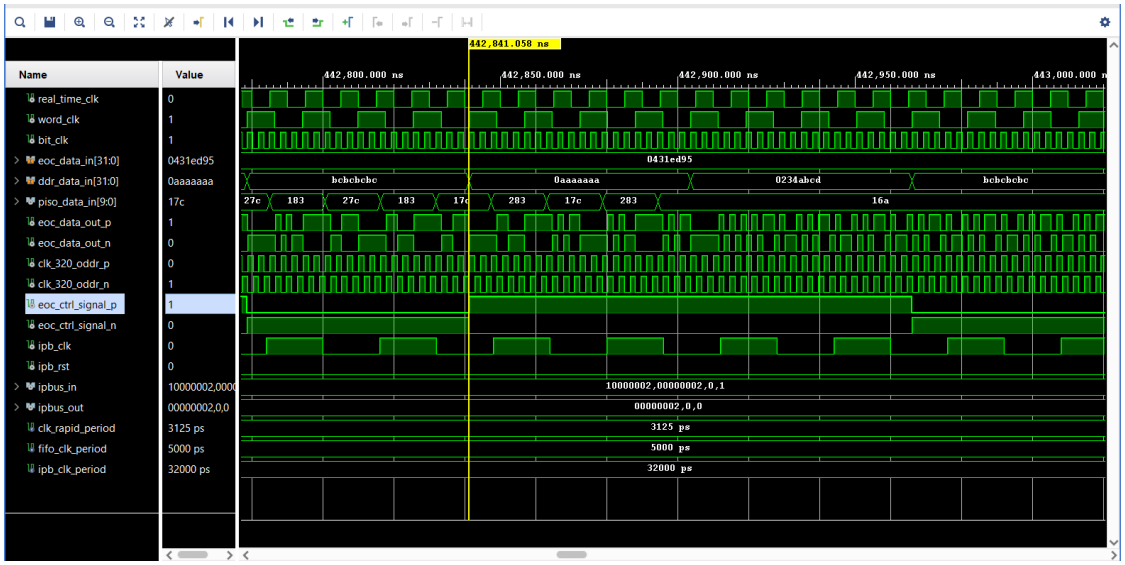

Figure 4.8: Example of simulation of the IPbus mechanism.

I also tested the synchronization of the serial links using a VHDL test bench, whose signals are shown in Fig. 4.9.

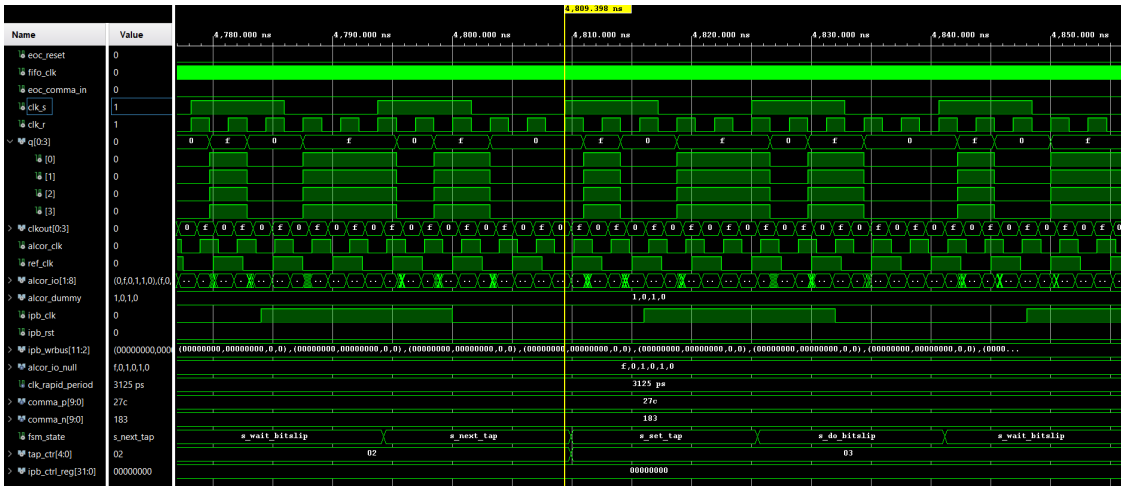

Figure 4.9: Link alignment mechanism demonstration test bench.

Implementation

After the synthesis and the implementation, I downloaded the bitstream file generated onto the FPGA.

I used the IPbus protocol to link a `C++` software and the VHDL firmware. The software reads data from a file or sends directly some data, which subsequently are used as input for the EoC. Some examples of the expected outputs, obtained with an oscilloscope, are shown in Fig. 4.10.

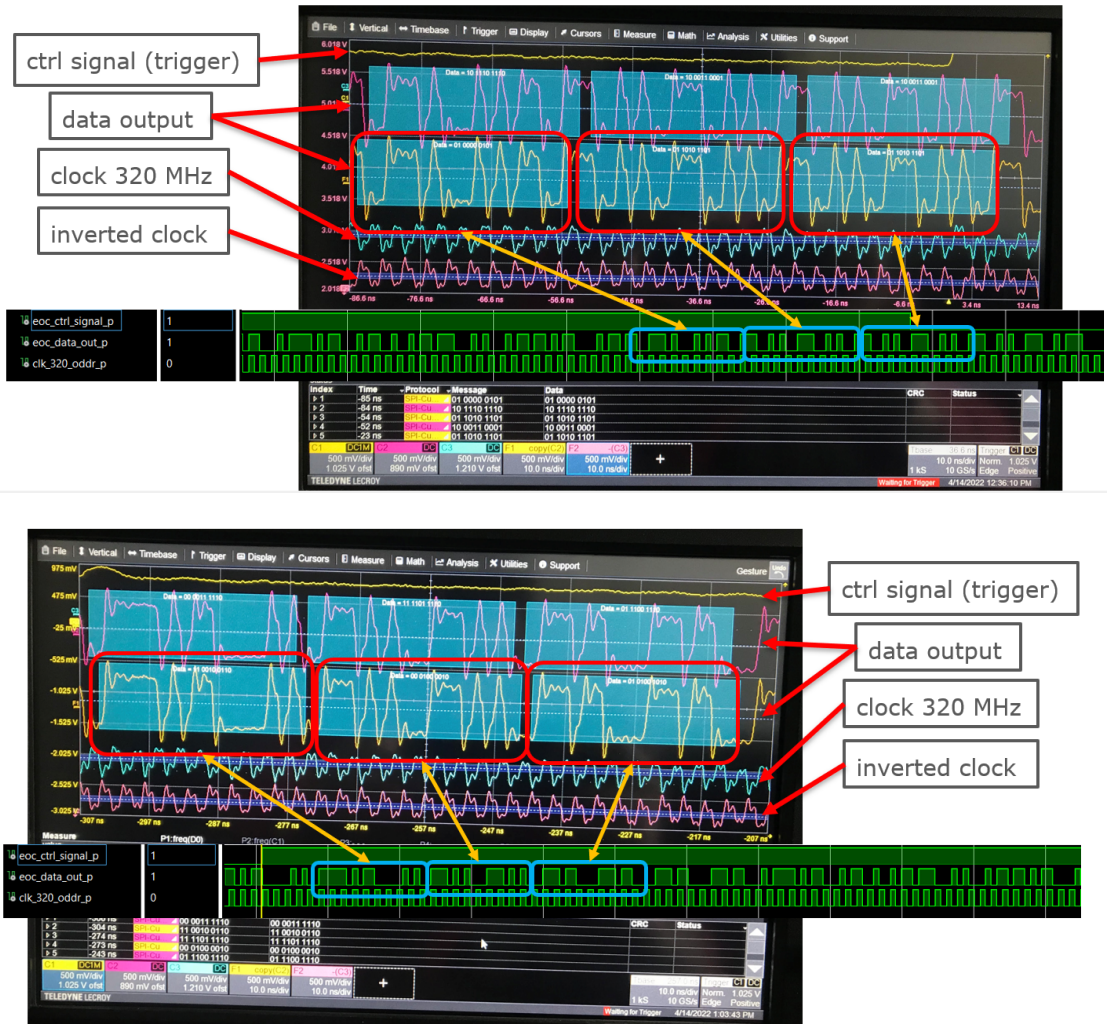

Figure 4.10: Examples of inputs and outputs with an oscilloscope. It can be seen that the simulated signal and the real signal match.

Final testing

I needed to test the DAQ firmware during its development, so that I could be sure it would be able to correctly receive data from the chip. First, I downloaded the DAQ firmware onto one FPGA Virtex-7 VC707, that will be used for the GRAIN demonstrator. Then, I downloaded my emulator firmware onto another FPGA of the same model, since it was available. Afterwards, I connected the two FPGAs through an FMC cable. In this way, the FPGA with the emulator replaced the ALCOR ASIC and I used it to send data to the FPGA with the DAQ firmware. In order to transmit data, I developed a `C++` software to be able to communicate with both the FPGAs at the same time, using two different URI addresses. After the registers are configured, comma and data blocks are written using the IPbus protocol.

The differential output of the first FPGA is connected to the differential input of the second FPGA, whose firmware receives the data, performs the alignment mechanism and returns some words. These words are read using the software.

Furthermore, alignment and idle comma words can be ignored. In this way, only words belonging to data frames are read.

Words sent to the emulator, and encoded by it, were then decoded by the DAQ firmware. This made it possible to modify and correct the firmware during its development. Thanks to the emulator, it was possible to communicate with the ASIC and verify the functioning of its digital part as soon as it was integrated.

4.3 DAQ firmware

The DAQ firmware will be used to communicate with the ALCOR ASIC. First, the words transmitted serially are reconstructed and aligned, using known transitions between 0s and 1s to find the boundary of different words. Then, a Finite State Machine (FSM) is used to keep track of the stream status and to preserve just data words and useful information. The user is then able to read the data words and the information through the IPbus protocol, for which a control software is used.

After the reconstruction and alignment of the words from the ALCOR, it is important to correctly use their information and to identify the data words using the event builder part of the firmware. The event builder constitutes the core of the DAQ, since it parses the data frame and extracts useful information. It receives aligned data as an input and it then places its output in a private buffer, with a private index containing also the part of metadata that is actually useful.

4.3.1 DAQ event builder FSM

The most important part of the event builder is a Finite State Machine (FSM) which, depending on the input word, manages the different states of the stream and performs different operations. The possible states are: reset, link alignment, link idle, event header, data words, counter rollover, status header, status words, crc header, crc check, waiting for a new frame. The FSM scheme is shown in Fig. 4.11.

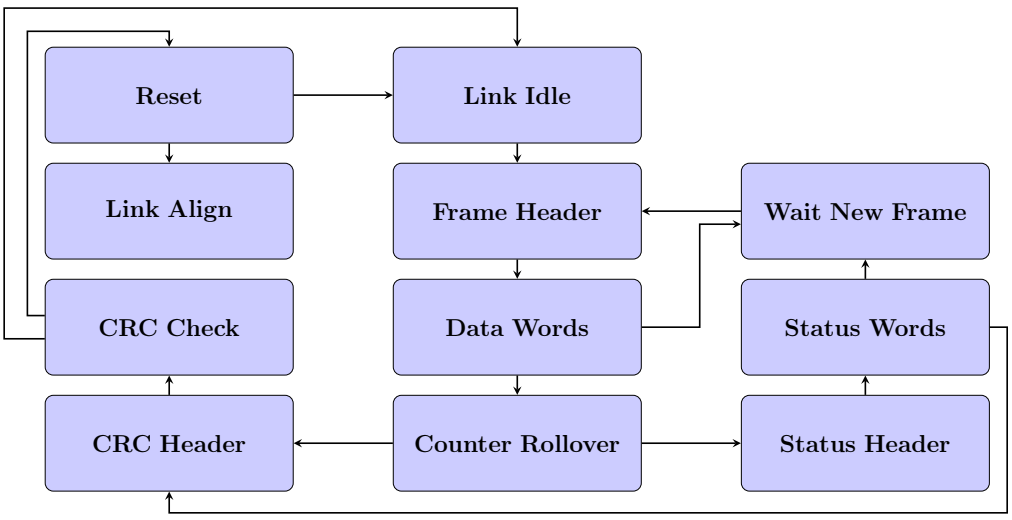

Figure 4.11: Event builder finite state machine.

In case of the reset state, indices are set to zero and the write enable is disabled. Instead, if alignment commas are sent by the ALCOR to synchronize the data stream, the selected state becomes link alignment. Then the ALCOR sends idle commas, waiting the arrival of data words. The arrive of data words is announced by an event header comma. The index and the output of the event builder are updated only when the state is data words.

At the end of a data frame, the ALCOR sends a counter rollover comma. Then, two cases are available, depending on the ALCOR setup. The first possibility is that a status header comma is sent, followed by status words that tells the user useful information about the data stream condition. The other possibility is that a crc header comma is subsequently sent after the counter rollover comma, if the raw mode of the ALCOR is selected. In this way, all the status words are ignored. Then the crc value is checked and the data acquisition stops ore continue with another frame.

Errors can occur during a certain state and this would lead to a loss of all the data stream. For this reason, the wait new frame state was introduced to not update the index and the output of the event builder, loosing just a single frame and starting again when another one is sent.

4.4 DAQ software

A `C++` interface is used to communicate with the FPGA and to set ALCOR parameters through the IPbus protocol. In particular, the computer interfaces with the FPGA using the IPbus protocol, while the FPGA and the ASIC communicate with two different serial protocols: SPI (Serial Peripheral Interface) and 8b/10b. SPI is used by the FPGA to set the ALCOR parameters, while the 8b/10b is used to send data streams from the ALCOR to the FPGA. The software is a library of classes and functions that represent system components and allow them to be configured consistently. The software is organized in such a way to minimize the dead time between different read/write operations. To do so, the number of dispatches, i.e. the actualization of such operations, is kept as low as possible.

4.4.1 Architecture

The software architecture is divided into two main parts: one relative to the FPGA and one relative to the ASIC. The FPGA part contains some useful methods such the ones to retrieve the information on the hardware identity and on the firmware version. Furthermore, it contains a method to reset the ASIC, setup the clocks, setup the links, use the spy process to read data words before and after the decoding. Finally, it contains a test pulse method that can be used to configure the parameter with which a test pulse is generated by the ALCOR ASIC.

Another part of the software is the one relative to the ASIC configuration. It contains all the methods to read and write on the different registers of the ALCOR ASIC. It is possible also to configure the default setup through the appropriate method. The different registers' setups are grouped into preamplifier setup, threshold setup and tdc setup methods.

Beyond these parts, there is also an acquisition code, in which it is possible to select the duration or the size of a data acquisition. It is used to read data output from the FPGA, after the different processes explained previously.

4.4.2 DAQ tool

The DAQ tool exploits the methods just described in order to perform tests and read data from the ALCOR ASIC. First, an FPGA is selected. Then, after verification that the connection is successful, all the clocks are set up correctly. Afterwards, the ASIC is configured with its default values. The link alignment is performed to identify the word boundaries, in order to make sure that the data stream is not corrupted. Subsequently, it is possible to enable the test pulse and set its parameters. Alternatively, if a sensor is mounted on the board, it is not necessary to use the test pulse. In any case, the ALCOR's parameter such gain, threshold level and offset are set. After the acquisition starts, it is possible to study the signals with an oscilloscope, probing the threshold and the output debug pads of the ALCOR ASIC.

Chapter 5

Measurements

The cryogenic environment, the channel density needed for imaging purpose and the wavelength of the photons emitted by liquid argon, pose a real challenge for the implementation of the GRAIN technology.

It is the first time that such a technique is implemented and since it presents several issues that have to be addressed, I took part in the realization of of demonstrator of the GRAIN imaging system and then I proceeded to test it.

5.1 Preliminary operations

The demonstrator system is shown in Fig. 5.1. I used it to perform measurements at both room temperature and cryogenic temperature. First, I conducted some preliminary operations before the real tests. I used the DAQ software described in Sec. 4.4 to perform the synchronization of the serial links with the 8b/10b encoding. Then, I generated test pulses using the FPGA to characterize the response of the ASIC. Subsequently, I performed parameters scans to find the optimal ASIC settings, such as offset, gain and threshold for each channel.

Figure 5.1: Demonstrator system setup. The FPGA is shown in the bottom-left corner, while the PCB with an ALCOR ASIC and a SiPM matrix is present on the right, above the Dewar.

5.1.1 Connector test in liquid nitrogen

A quadruple connector (Samtec Q Strip) is used to link the PCB with the board that hosts a SiPM matrix. In order to test the connector's capability to withstand mechanical stress and immersion in liquid nitrogen, I developed a simple firmware and I downloaded it onto an FPGA. Clock signals were continuously sent to all the channels in order to control if some of them had problems or stopped working. The tests were performed using a *mechanical demo* of the system which has a different circuit, not with the real motherboard and matrix, which are not connected to the FPGA. The immersion cycle was completed many times and no particular problems were found, even considering the stress suffered during the tests. In fact, the board was inserted and removed very quickly, whereas in the actual detector, the same cycle will be gradual, modifying the temperature with progressive steps to avoid high stress and ensure an optimal performance. Furthermore, the connector was subjected to 20 *mating cycles* every immersion, to test mechanical resistance as well.

5.1.2 Link alignment

I synchronized the serial links by using the DAQ software. Indeed, I tested the accurate functioning of the alignment mechanism, by finding the correct boundaries between different words of real data frames sent by the ALCOR ASIC, after it was mounted on the PCB, as shown in Fig. 5.2.

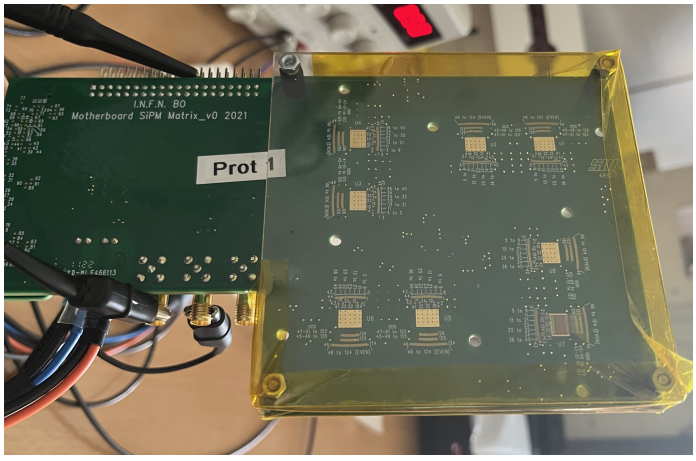

Figure 5.2: An ALCOR ASIC mounted on the PCB in the bottom right corner.

The ASIC uses the 8b/10b protocol to send data words to the FPGA. This encoding mechanism has a single and double bit error detection mechanism. It is therefore possible for the DAQ firmware to keep track of errors by increasing a counter coded in the firmware. As the counter remained zero during all tests, no errors were detected and the data stream was successfully aligned.

5.1.3 Test pulse configuration

Using the DAQ software, I sent test pulses generated by the FPGA to the chip. They can be used to test the ALCOR ASIC response before mounting a SiPM

photosensor and using a light source. With the oscilloscope it is possible to probe the threshold level and the amplifier output of the channels 0 and 28, because they are connected to debug pads, as shown in Fig. 5.3.

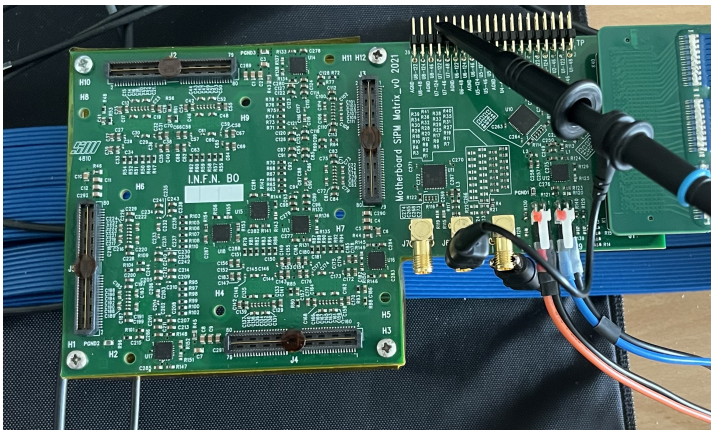

Figure 5.3: Connections to the oscilloscope to probe the test pulse.

I used the wave-forms observed at the oscilloscope to find the starting parameters for the ALCOR channels, which were not optimized, but they were used as initial values during the subsequent parameter scans.

5.1.4 Parameter scans

I used the DAQ software to vary one parameter at the time, obtaining the optimal ones. The parameter were chosen to maximize the amplitude, which was measured using the oscilloscope.

A constant voltage threshold needs to be set for each channel to configure the discriminator. To adapt to multiple types of signals, the ALCOR chip uses several parameters to tune the voltage threshold range and resolution. In this measurement the ALCOR parameters were set in such a way that the threshold could cover all the voltage values between the minimum and maximum values that the test pulse could assume. Then, I performed a scan of the discriminator threshold over the configured range by changing the relevant parameter of the ALCOR from 0 to 63.

Using these scans, the number of events for each channel was counted and plotted as a function of the threshold setting. At low values, the signal baseline is completely above the threshold level, therefore no events are triggered. This phenomenon is due to the fact that the ASIC is edge-triggered and not level-triggered, therefore, if no edge crosses the threshold, the discriminator does not trigger. No entries are present also for high values, since the threshold is above the signal and does not trigger any events. Instead, for intermediate values, from approximately 20 to 50, the events number was almost constant. The common threshold of the discriminator was then set to the average center value of the plateau, to increase the margin against fluctuations. An example of the behaviour of the number of events in function of the pixel threshold can be seen in Fig. 5.4.

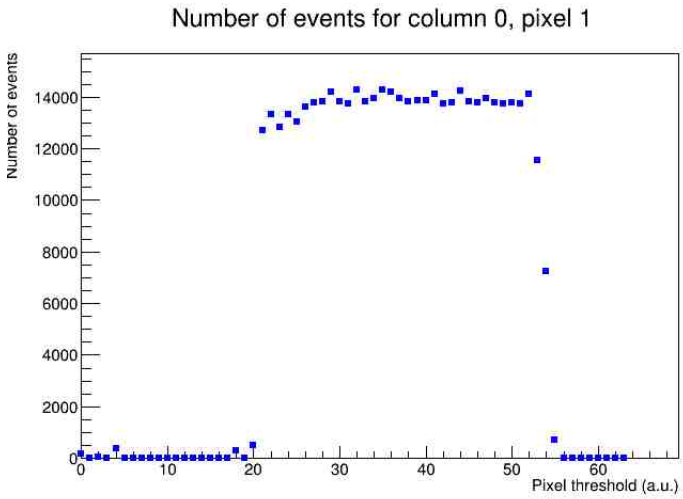

Figure 5.4: Number of events as a function of the pixel threshold (LEDAC parameter of the chip). The measurement was performed at room temperature using the internal test pulse generator triggered by the FPGA.

5.2 Test pulse measurements

I performed measurements at room temperature, in nitrogen gas just above the surface (approximately $-100\,^{\circ}\mathrm{C}$) and at liquid nitrogen temperature ($-196\,^{\circ}\mathrm{C}$). Indeed, even if GRAIN will use liquid argon, liquid nitrogen was used for the demonstrator to test the ALCOR performance and parameters inside a cryogenic environment, because they have a similar boiling point temperature. The liquid nitrogen Dewar, together with the board on which the ALCOR was mounted is shown in Fig. 5.5.

Figure 5.5: Experimental setup for cryogenic measurements: a liquid nitrogen Dewar, on top of which is present an ALCOR ASIC mounted on a board ready to be immersed.

5.2.1 Test pulse measurements at room temperature

I performed the setting of the parameters of the ALCOR ASIC using the experimental apparatus previously described. In particular, for what regards the preamplifier parameters, the polarity was set negative for the test pulse, while for the SiPM signals it has to be set positive. The gain was set at its maximum value, which is approximately 577 mV/pC. Two other parameters are the *boost*, which defines the current bias of the preamplifier boost stage, and the *common gate*, which defines instead the current bias of the preamplifier input stage. They are important because they modulate the output signals and both of them can assume a value from 0 to 31. The boost bias parameter can range from 1.17 mA to 3.97 mA, and it was set to 25 for the initial measurements, which corresponds to a value of approximately 3.67 mA. On the other hand, the common gate bias parameter can vary between 17.3 µA and 93.2 µA, and it was set to 12, which corresponds to a value of approximately 54.73 µA. For what regards the threshold parameters, the range of the threshold was set to its maximum value, to allow more freedom in changing the threshold, at the expense of resolution. The discriminator threshold was set to a value around 40, as a result of the parameter scans described in the previous section.

The initial tests confirmed that the digital part of the chip and its communication with the FPGA were working properly at room temperature. The data frames were sent correctly and it was possible to acquire the data words. Also the analog part of the ASIC worked correctly, the test pulse signal was present as it is shown in Fig. 5.6.

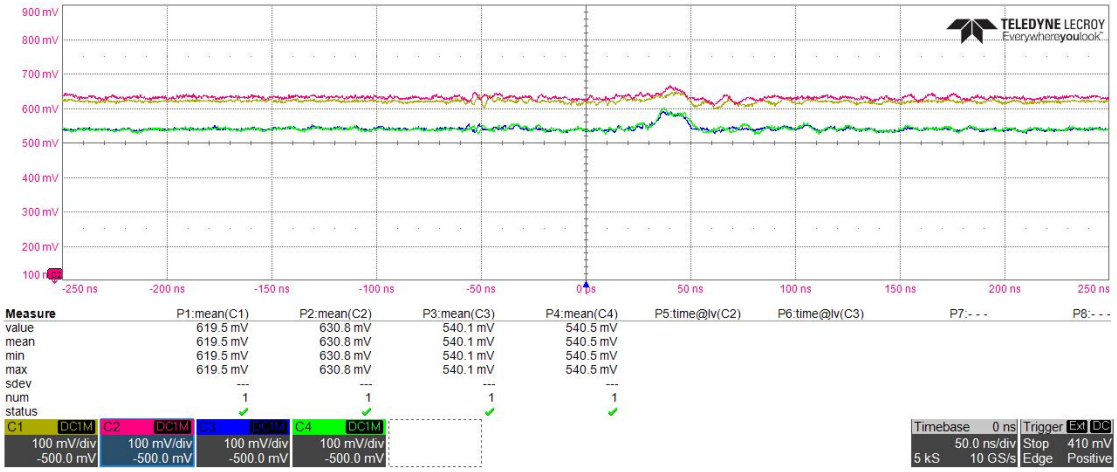

Figure 5.6: Measurement at room temperature, with negative polarity, offset 0, boost 25, cg 12. C1 and C2 are the thresholds, C3 and C4 the signals for channel 0 and 28. Trigger is EXT given by the FPGA synchronous with the test pulse signal.

5.2.2 Test pulse measurements at cryogenic temperature

The PCB on which the ALCOR ASIC was mounted, was then immersed in a Dewar filled with liquid nitrogen, as it is shown in Fig. 5.7.

I monitored the temperature of the board during the immersion in liquid nitrogen with a PT100 sensor. Up to −60 °C, with the ASIC above the liquid nitro-

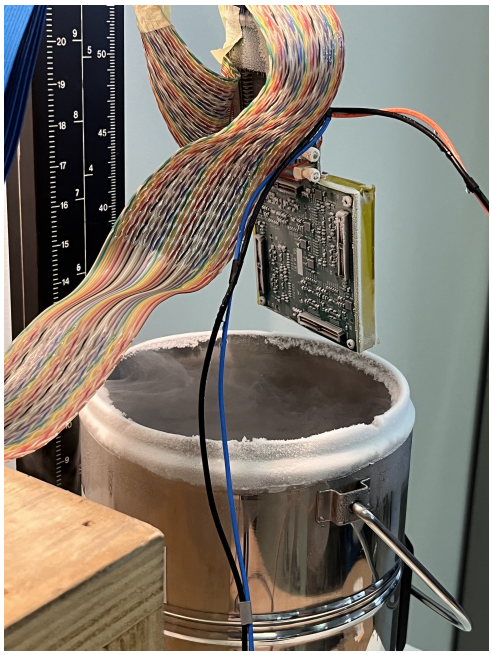

Figure 5.7: Frozen PCB after an immersion in liquid nitrogen.

gen, the signal was still visible. By further lowering the temperature, the signal progressively lost amplitude and the baseline shifted downward, until the chip reached $-100\,°C$, at which point the signal completely disappeared and flattened out. During the immersion, I tried to change the parameter values of the ASIC (in particular, boost and cg), to attempt to recover the signal, but this was not successful. Indeed, the output signals decreased gradually when the temperature was becoming lower.

An exchange of information with the chip designers allowed to conclude that it was indeed the pulse generator itself, and not the amplifier, that was malfunctioning. Therefore, it was decided to continue the test with a real signal from SiPMs. Nevertheless, thanks to these tests, it has been possible to demonstrate that the digital part of the chip and its communication with the FPGA are working just as well in cryogenics as they do at room temperature. In fact, the data frames were sill sent correctly, even though no data words were sent, since no pulse was detected. Incidentally, this also proved that external clock buffers and voltage regulators also continued to work in a cryogenic environment.

5.3 SiPM matrix measurements

A SiPM matrix with 16×16 channels, Hamamatsu model S13615, was mounted on the board after having been obscured. First, the polarity of the chip was inverted and set to positive, since the threshold only triggers for positive signals. Then, tests at room temperature and at cryogenic temperature were performed, biasing the SiPM matrix to observe dark count signals from the SiPMs.

In order to obtain the expected SiPM signals both at room and cryogenic temperature, the reference voltages of the ALCOR were changed from 600 mV to

745 mV, while the supply voltage was increased from the nominal 1.2 V to 1.36 V, based on additional information from the chip designers.

5.3.1 SiPM matrix measurements at room temperature

First, the global I-V characteristic curve of the SiPM matrix was obtained, varying the bias voltage and measuring the current. This operation was performed in order to find the point in which the current grows rapidly after being almost constant. This happens in correspondence of the breakdown voltage. For the SiPM matrix selected, the nominal value according the datasheet was (53 ± 5) V [57], and a value of approximately 54 V was found measuring the I-V curves with a source measure unit.

Using the oscilloscope and probing the debug pads, it was then possible to observe the well-known waveform signal of the SiPM. In particular, it was possible to distinguish different waveforms for one, two and three photons. In order to make the signals clearer and eliminate ringing in the amplifier output, the boost bias and the common gate bias parameters of the ALCOR were modified and both were set to a value of 2, which corresponds to 1.4 mA and 27.7 µA respectively. The signal is shown in Fig. 5.8. The same measurement was also performed maintaining the persistence active, which is shown in Fig. 5.9. As can be seen in the waveform, the attempt to eliminate ringing was only partially successful, but the signal-to-noise ratio is acceptable.

This test showed that it was possible to readout a SiPM matrix using the chip and that the system worked at room temperature.

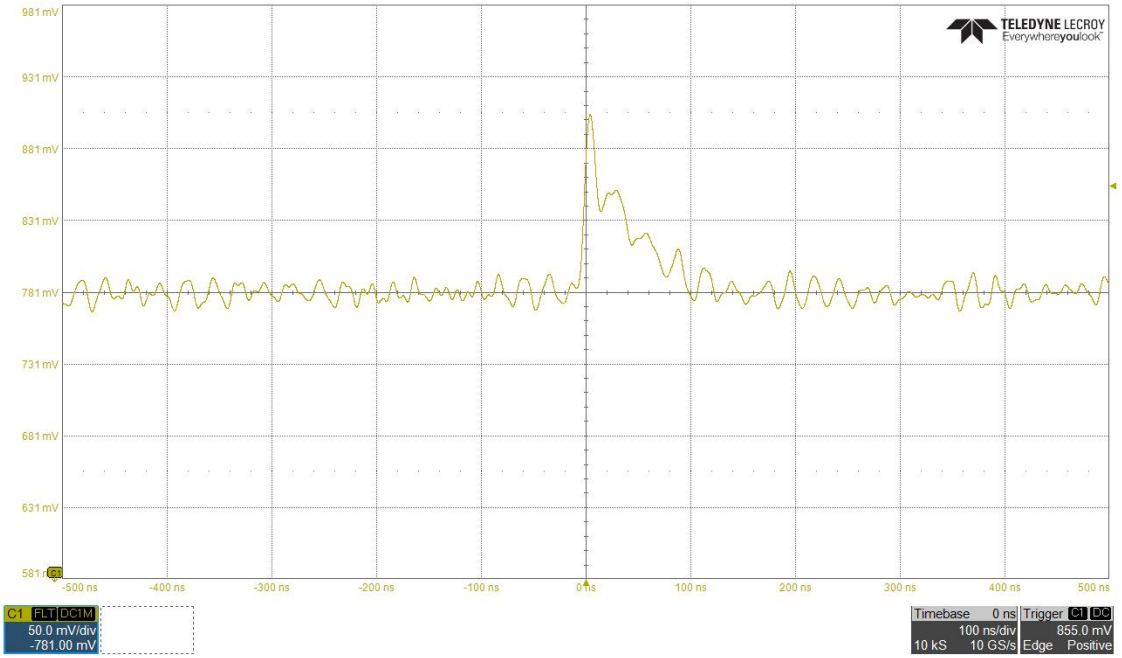

Figure 5.8: Measurement at room temperature, with positive polarity, boost 2, cg 2, SiPM matrix with $V_{bias} \sim 54\,\mathrm{V}$. SiPM matrix output signal for channel 0. A 80 MHz filter is used.

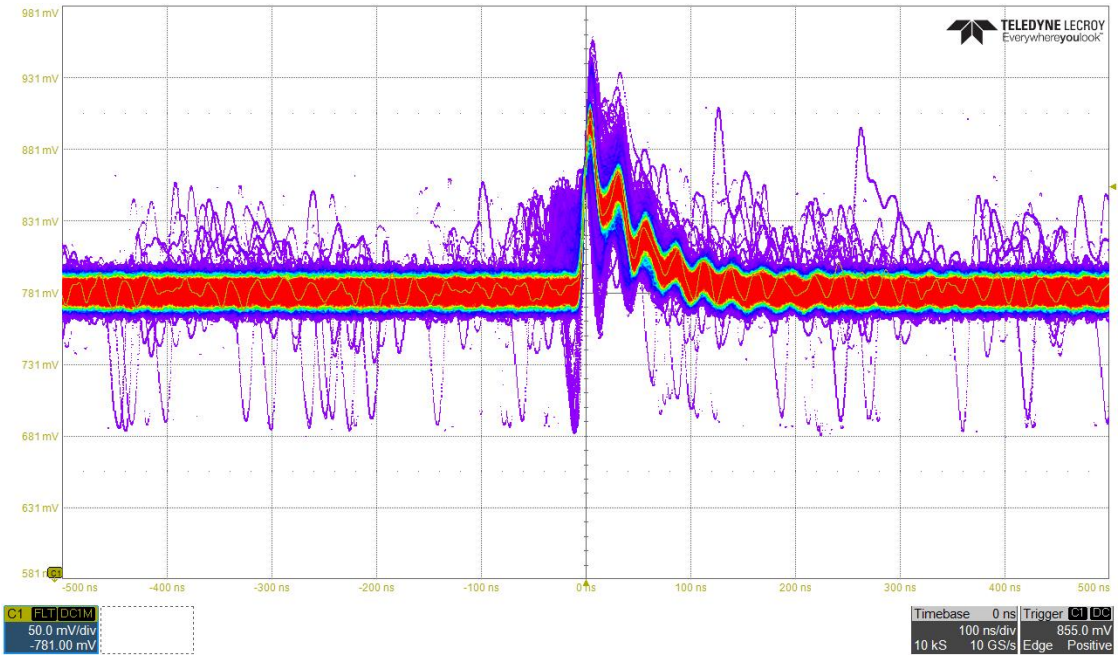

Figure 5.9: Measurement at room temperature, with positive polarity, boost 2, cg 2, SiPM matrix with $V_{bias} \sim 54\,\mathrm{V}$. Persistence of the SiPM matrix output signal for channel 0. A 80 MHz filter is used.

5.3.2 SiPM matrix measurements at cryogenic temperature

Similar tests were performed also in liquid nitrogen, using the setup shown in Fig. 5.10. At liquid nitrogen temperature (77 K), the breakdown voltage for the SiPM matrix decreased by approximately 6 V.

Figure 5.10: PCB with SiPM matrix mounted on, after an immersion in liquid nitrogen.

In the very fist tests, the only thing that one could see at cryogenic temperatures was a sinusoidal waveform which oscillated at a frequency of 50 Hz.

The situation improved after the replacement of the supply and reference voltage values of the ALCOR. The SiPM waveforms became visible also at cryogenic temperature, showing that the analog part of the ALCOR ASIC was now working correctly.

Decreasing the temperature, it is necessary to further change the values of the boost and cg parameters, otherwise the signal is obscured by a self-oscillation of the amplifier. Therefore, I used the DAQ software to perform the scan on these two parameters. From the measurements, it is evident that the best signal-to-noise ratio is obtained for cg equal to 0. Indeed, for cg equal to 31 (Fig. 5.11) and 2 (5.12), the noise is really high and the signal is modulated. Instead, the modulation is reduced in case cg is set to 0, which is shown in Fig. 5.13, where the signal is due to a single photo-electron.

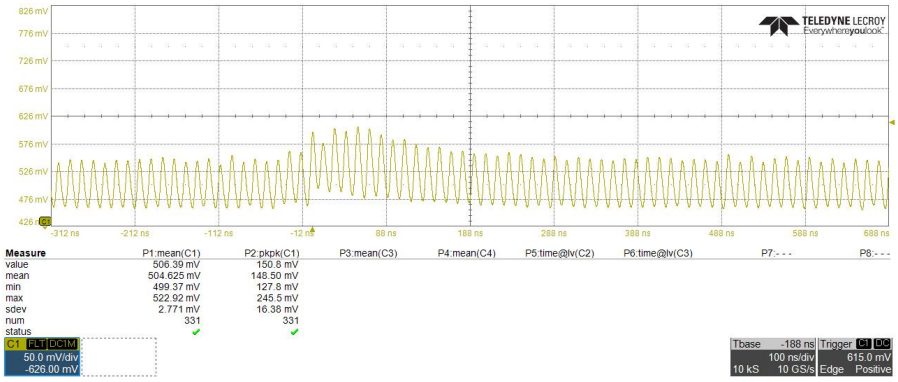

Figure 5.11: Measurement inside the LAr at 77 K*, with positive polarity, boost 2, cg 31, SiPM matrix with* $V_{bias} \sim 48$ V*. SiPM matrix output signal for channel 0. A 80 MHz filter is used.*

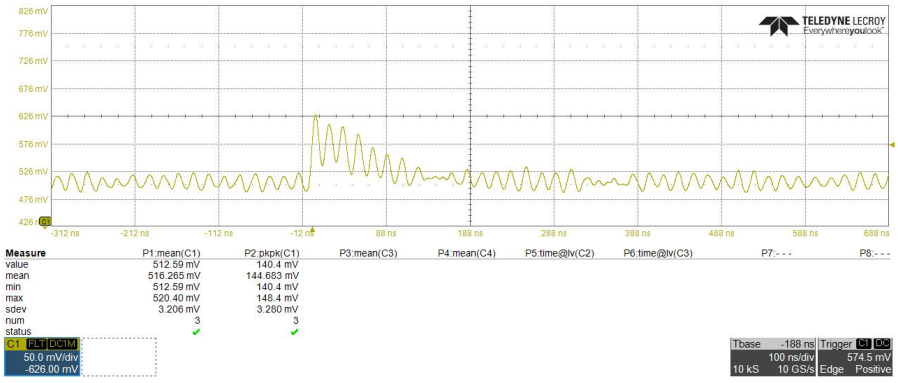

Figure 5.12: Measurement inside the LAr at 77 K*, with positive polarity, boost 2, cg 2, SiPM matrix with* $V_{bias} \sim 48$ V*. SiPM matrix output signal for channel 0. A 80 MHz filter is used.*

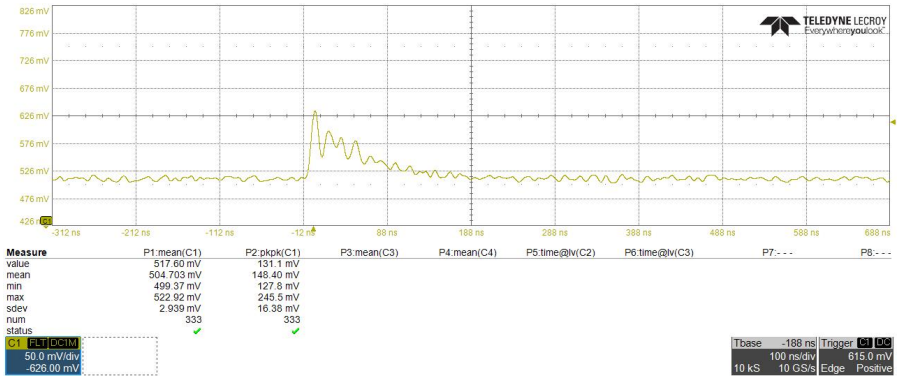

Figure 5.13: Measurement inside the LAr at 77 K*, with positive polarity, boost 2, cg 0, SiPM matrix with* $V_{bias} \sim 48$ V*. SiPM matrix output signal for channel 0. A 80 MHz filter is used. The signal for a single photo-electron is shown. While the ringing is still present, the SNR is acceptable.*

A signal due to two photo-electrons is shown instead in Fig. 5.14 and Fig. 5.15 shows the superposition from many waveforms.

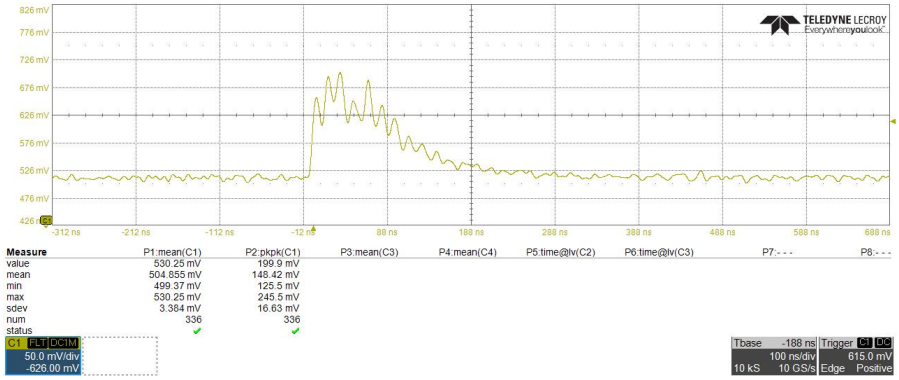

Figure 5.14: Measurement inside the LAr at 77 K*, with positive polarity, boost 2, cg 0, SiPM matrix with* $V_{bias} \sim 48$ V*. SiPM matrix output signal for channel 0. A 80 MHz filter is used. The signal for two photo-electrons is shown.*

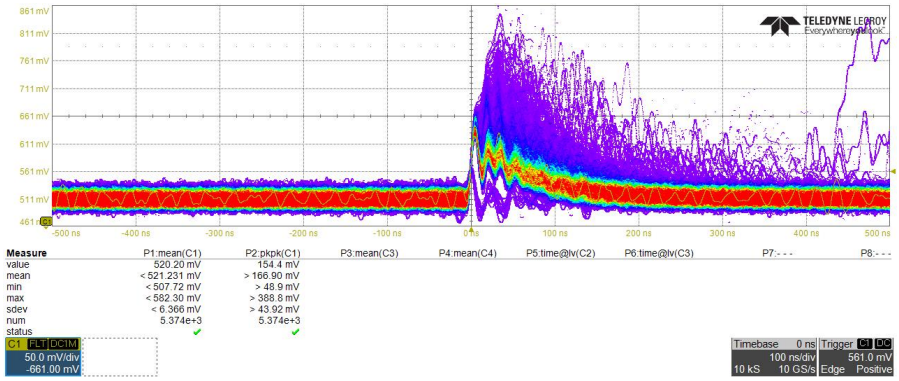

Figure 5.15: Measurement inside the LAr at 77 K*, with positive polarity, boost 2, cg 0, SiPM matrix with* $V_{bias} \sim 48$ V*. Persistence of the SiPM matrix output signal for channel 0. A 20 MHz filter is used.*

Then the bias voltage was increased, to make the SiPM matrix saturate, in an effort to find the maximum range of the amplifier, as it is shown in Fig. 5.16.

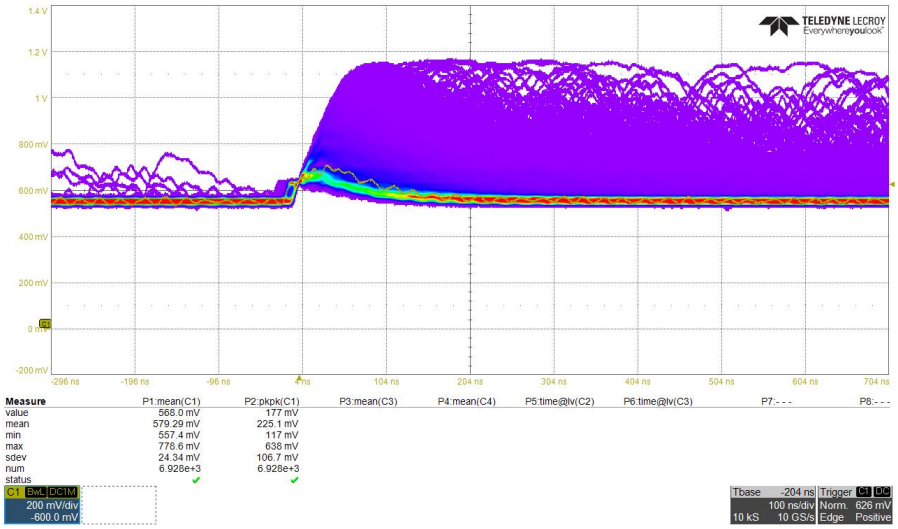

Figure 5.16: Measurement inside the LAr at 77 K*, with positive polarity, boost 2, cg 0, SiPM matrix with* $V_{bias} \sim 54$ V *(substantially above normal operating voltages). Persistence of the SiPM matrix output signal for channel 0. A 20 MHz filter is used. The signal saturation is evident at* ∼1.1 V *compatible with the maximum supply voltage.*

Having proved that the ALCOR works sufficiently well from the analog point of view and does not have any issue in the digital domain, the demonstrator project will continue to be carried out to test the imaging capability of the GRAIN detector.

5.4 Prototype limitations

The ALCOR ASIC employed for the thesis work presents potential limitations for the imaging in GRAIN beyond the performance of its analog front-end. Its architecture only has 8 channels per link and has a relatively high power consumption. While not a problem by themselves, these features limit the number of the channels that could be effectively integrated in the limited GRAIN volume.

A higher number of channels per link would allow more SiPM arrays to be read with just a few links.

In addition, power consumption due to the ASIC themselves and the number of cables that are used to communicate between ASICs and FPGAs can constitute a potential issue. Indeed, both a high-power consumption and a high number of cables would result in heat entering the cryostat, leading liquid argon to boil.

It is possible to observe this phenomenon also in liquid nitrogen. Indeed, the boiling effect is evident just after the immersion of the board inside the liquid nitrogen and it can be observed in Fig. 5.17.

By considering the voltage and the current necessary to power the ALCOR ASIC and the associated circuitry, which are respectively 3.9 V and 0.38 A, the total power consumption due to Joule heating is ~ 1.5 W. Considering then the latent heat of vaporization of the nitrogen, which is equal to 1.992×10^5 J/kg,

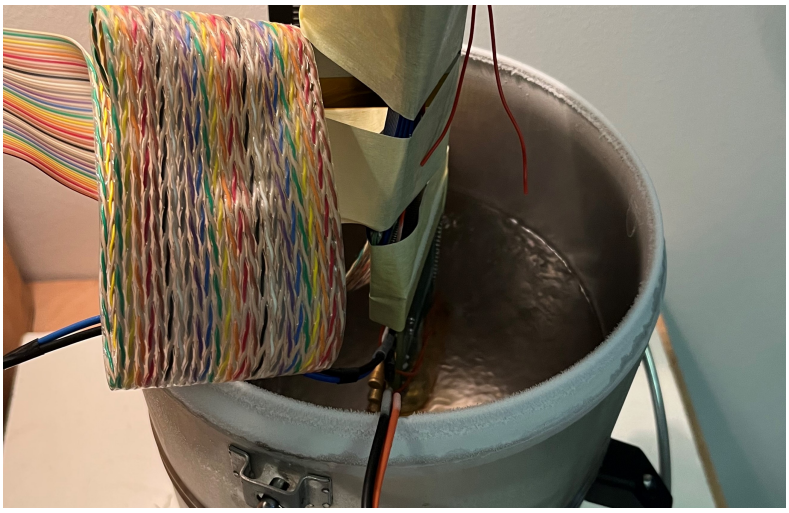

Figure 5.17: Nitrogen boiling due to the heat produced by the chip power supply.

it is possible to calculate that 0.75×10^{-5} kg evaporates every second. These calculations hold for a single ALCOR, with just 32 channels, while several tens of thousands of channels will be used in GRAIN, leading to a considerable boil-off rate on the order of a kilogram per minute.

In the future, an ASIC with an increased number of channels, e.g. 128 per link, will be needed. Furthermore, the desired chip has to operate at cryogenic temperatures, and it needs to have a lower power consumption.

The ALCOR ASIC will still be fundamental in the realization of a GRAIN demonstrator.

Conclusions

The GRAIN detector will be a part of the Near Detector complex of DUNE. It will be based on an innovative imaging technique to exploit the scintillation light emitted by liquid argon at 127 nm. The optical system foresees the use of coded aperture masks and/or lenses, while SiPM matrices will be used as photo sensors. A mixed-signal ASIC will be used to read out SiPMs inside the liquid argon, while the back-end electronics will be implemented in FPGAs outside the cryogenic environment.

The present thesis work focused on the realization of a demonstrator of this novel technology. Indeed, there are several critical requirements that have to be satisfied, such as the use of complex electronics at cryogenic temperature, the channel density necessary for imaging purpose and the detection of photons at the wavelength emitted by LAr when crossed by charged particles.

Therefore, a demonstrator was realized with the purpose of proving the imaging capability of the system. It consists of a 16 $\times$ 16 SiPM matrix connected to a custom PCB on which it is possible to mount up to 8 ASICs. The ALCOR (A Low-power Circuit for Optical sensor Readout) mixed-signal ASIC prototype optimized for the readout of SiPMs at cryogenic temperatures is being used for the demonstrator.

The first step of this work was the development of a VHDL emulator of the ALCOR ASIC. It allowed the development and validation of the DAQ firmware even when the integration of the ASIC was not yet possible. Thanks to the completeness of the emulator, that allowed thorough verification of the DAQ firmware, the integration between ASIC and FPGA was immediately successful.

Subsequently, the experimental setup with the ASIC was tested both at room and cryogenic temperature. With these tests, I proved that the digital part of the chip and its communication with the FPGA were working both in cryogenics and at room temperature.

Finally, a SiPM matrix was also integrated in the system and this allowed to test the analog part of the ALCOR ASIC as well. Indeed, it was possible to observe the photo-electron signals both at room and cryogenic temperature. The complete SiPM matrix readout system was tested in order to ensure its full functionality, with the purpose of proving the imaging capability of the system.

Through this work I could verify that the ALCOR ASIC satisfies the requirements of the readout chip for the GRAIN demonstrator, despite some limitations outlined above.

Bibliography

[1] Giunti C. and Kim C.W., *Fundamentals of Neutrino Physics and Astrophysics*, 2007, Oxford University Press.

[2] Bilenky S., *Introduction to the Physics of Massive and Mixed Neutrinos*, 2010, Springer.

[3] Takaaki K., *Atmospheric Neutrinos*, New Journal of Physics, vol. 6, 2004, doi:10.1088/1367-2630/6/1/194.

[4] McDonald A. et al., *Astrophysical Neutrino Telescopes*, Review of Scientific Instruments, vol. 75, 2003, doi:10.1063/1.1642740.

[5] ANTARES Collaboration, *Nobel Prize in Physics 2015 for the discovery of neutrino oscillations, which shows that neutrinos have masses*, 2015, `https://antares.in2p3.fr/News/news_nobel2015.html`.

[6] Fisher P. et al., *Neutrino Mass And Oscillation*, Annual Review of Nuclear and Particle Science, vol. 49, 1999, doi:10.1146%2Fannurev.nucl.49.1.481.

[7] Michael D.G. et al., *MINOS Collaboration*, Phys. Rev. Lett., vol. 101, 2008, doi:10.1103/PhysRevLett.101.131802.

[8] Habig A., *A Brief Review of MINOS neutrino oscillation results*, Modern Physics Letters A, 2010, doi:10.1142/s0217732310033232.

[9] Aharmim B. et al., *Combined analysis of all three phases of solar neutrino data from the Sudbury Neutrino Observatory*, Physical Review C, vol. 88, 2013 doi:10.1103/physrevc.88.025501.

[10] Chavarria A., *Solar neutrinos in 2011*, Proceedings of XXXI Physics in Collision 2011, 2012, doi:10.48550/ARXIV.1201.6311.

[11] NuFIT, `http://www.nu-fit.org/`.

[12] Abe K. et al., *Proposal for an Extended Run of T2K to* 20×10^{21} *POT*, 2016.

[13] Adrián-Martínez S. et al., *Letter of intent for KM3NeT 2.0*, Journal of Physics G: Nuclear and Particle Physics, vol. 43, 2016, doi:10.1088/0954-3899/43/8/084001.

[14] Ghosh M., *Maximizing the DUNE early physics output with current experiments*, Eur. Phys. J. C, vol. 76, 2016, doi:10.1140/epjc/s10052-016-3962-7.

[15] Muether M. et al., *Initial Performance from the NOνA Surface Prototype Detector*, Physics Procedia, vol. 37, 2012, doi:10.1016/j.phpro.2012.02.453.

[16] Patterson R. et al., *Development of a joint oscillation analysis by the NOvA and T2K collaborations*, 2021, `https://www.snowmass21.org`.

[17] Manly S., *Snapshots of neutrino oscillation physics today and a preview of tomorrow*, EPJ Web of Conferences, 2018, doi:10.1051/epjconf/201818202080.

[18] Giunti C., *Double Beta Decay and the Absolute Neutrino Mass Scale*, 2003, doi:10.1063/1.1818390.

[19] Gatti F. et al., *Microcalorimeter Arrays for a Rhenium Experiment*, 2022.

[20] Juan G.H., *Some aspects of neutrino phenomenology*, 2011.

[21] Aker M. et al., *Improved Upper Limit on the Neutrino Mass from a Direct Kinematic Method by KATRIN*, Physical Review Letters, vol. 123, 2019, doi:10.1103/physrevlett.123.221802.

[22] Giuliani A. and Poves A., *Neutrinoless Double-Beta Decay*, 2012, doi:10.1155/2012/857016.

[23] Guofo C., *Search for 0$\nu\beta\beta$ Decay with EXO-200 and nEXO*, Proceedings of Science, 2018.

[24] Aghanim N. et al., *Planck 2018 results. VI. Cosmological parameters*, Astronomy and Astrophysics, vol. 641, 2020, doi:10.1051/0004-6361/201833910.

[25] DUNE collaboration, *An International Experiment for Neutrino Science*, 2020, `https://www.dunescience.org/`.

[26] Abi B. et al., *Deep Underground Neutrino Experiment (DUNE), Far Detector Technical Design Report, Volume II: DUNE Physics*, 2020, doi:10.48550/ARXIV.2002.03005.

[27] DUNE collaboration et al., *Long-Baseline Neutrino Facility (LBNF) and Deep Underground Neutrino Experiment (DUNE) Conceptual Design Report Volume 2: The Physics Program for DUNE at LBNF*, 2015, doi:10.48550/ARXIV.1512.06148.

[28] Abi B. et al., *Supernova neutrino burst detection with the Deep Underground Neutrino Experiment*, The European Physical Journal C, vol. 81, 2021, doi:10.1140/epjc/s10052-021-09166-w.

[29] Boccone V., *Recent updates on the ArDM project: A Liquid Argon TPC for Dark Matter Detection*, J. Phys. Conf. Ser., vol. 65, 2007, doi:10.1088/1742-6596/160/1/012032.

[30] Heindl T. et al., *The scintillation of liquid argon*, EPL, vol. 91, 2010, doi:10.1209/0295-5075/91/62002.

[31] Machado A.A. et al., *The X-ARAPUCA: an improvement of the ARAPUCA device*, Journal of Instrumentation, vol. 13, 2018, doi:10.1088/1748-0221/13/04/C04026.

[32] Falcone A. et al., *Cryogenic SiPM arrays for the DUNE photon detection system*, 2020.

[33] Abi B. et al., *Volume IV. The DUNE far detector single-phase technology*, Journal of Instrumentation, vol. 15, 2020, doi:10.1088/1748-0221/15/08/t08010.

[34] DUNE collaboration et al., *The DUNE Far Detector Interim Design Report, Volume 2: Single-Phase Module*, 2018, doi:10.48550/ARXIV.1807.10327.

[35] Abud, A.A. et al., *Deep Underground Neutrino Experiment (DUNE) Near Detector Conceptual Design Report*, Instruments, vol.5, 2021, doi:10.3390/instruments5040031.

[36] Doke T., Masuda K. and Shibamura E., *Estimation of absolute photon yields in liquid argon and xenon for relativistic (1 MeV) electrons*, in Nucl. Instrum. Meth. A 291, 1990, doi:10.1016/0168-9002(90)90011-T.

[37] Babicz M. et al., *A measurement of the group velocity of scintillation light in liquid argon*, in J. Instrum. 15.09, 2020, doi:10.1088/1748-0221/15/09/P09009.

[38] Accorsi R., *Design of a near-field coded aperture cameras for high-resolution medical and industrial gamma-ray imaging*, 2001, `http://hdl.handle.net/1721.1/8684`.

[39] Gottesman S. and Fenimore E. E. *New family of binary arrays for coded aperture imaging*, Applied optics 28, 1989, pp. 4344–52, doi:10.1364/AO.28.004344.

[40] Andreotti M. et al., *Coded masks for imaging of neutrino events*, 2021, doi:10.1140/epjc/s10052-021-09798-y.

[41] SensL, *An Introduction to the Silicon Photomultiplier*, 2017, `https://www.sensl.com/downloads/ds/TN-IntrotoSPMTech.pdf`.

[42] Taggart M. et al., *Suitability of a SiPM Photodetector for Implementation in an Automated Thermoluminescent Dosimeter Reader*, in Radiation Physics and Chemistry, vol. 161, 2019, doi:10.1016/j.radphyschem.2019.01.015.

[43] Piemonte C., *A new Silicon Photomultiplier structure for blue light detections*, in Nucl. Instrum. Meth. A 568, 2006, pp. 224-232, doi:10.1016/j.nima.2006.07.018.

[44] Piemonte C. e Gola A., *Overview on the main parameters and technology of modern Silicon Photomultipliers*, in Nucl. Instrum. Meth. A 926, 2019, pp. 2-15, doi:10.1016/j.nima.2018.11.119.

[45] Hamamatsu Photonics, *A technical guide to silicon photomultipliers (MPPC) - Section 1*, 2018, https://hub.hamamatsu.com/us/en/technical-note/sipm-mppc-technical-note/section1.html.

[46] Grodzicka-Kobylka M. et al., *Silicon photomultipliers in gamma spectroscopy with scintillators*, in Nucl. Instrum. Meth. A 926, 2019, pp. 129-147, doi:10.1016/j.nima.2018.10.065.

[47] Arosio V. et al., *An Educational Kit Based on a Modular Silicon Photomultiplier System*, 2014, doi:10.48550/ARXIV.1308.3622.

[48] SensL, *C-Series Low Noise, Blue-Sensitive Silicon Photomultipliers Datasheet*, 2018, https://sensl.com/downloads/ds/DS-MicroCseries.pdf.

[49] Liu F. et al., *Characterization of a Mass-Produced SiPM at Liquid Nitrogen Temperature for CsI Neutrino Coherent Detectors*, 2022, doi:10.3390/s22031099.

[50] Hamamatsu Photonics, *Hamamatsu MPPC S13360 Series Datasheet*, 2019, https://www.hamamatsu.com/resources/pdf/ssd/s13360_series_kapd1052e.pdf.

[51] Kindt W.J., *Geiger Mode Avalanche Photodiode Arrays: For spatially resolved single photon counting*, Delft University Press, 1999.

[52] Hamamatsu Photonics, *Si-APD and MPPC Handbook*, 2014, www.hamamatsu.com/resources/pdf/ssd/e03_handbook_si_apd_mppc.pdf.

[53] Cervi T. et al., *Performances of some SiPM models for cryogenic applications*, in Nucl. Instrum. Meth. A 912, 2018, pp. 326-328, doi:10.1016/j.nima.2017.12.011.

[54] Cossio F., *ALCOR - User Guide*, 2022.

[55] Dellacasa G., *ALCOR End Of Column Datasheet*, 2021.

[56] Rose A., Williams T., *IPbus user guide*, 2016, https://ipbus.web.cern.ch/doc/user/html/index.html.

[57] Hamamatsu Photonics, *Hamamatsu MPPC arrays S13615 series datasheet*, 2020, https://www.hamamatsu.com/resources/pdf/ssd/s13615_series_kapd1062e.pdf.

Acknowledgements

I would like to thank my supervisor Dr. Sirri G. for his dedicated support through my thesis work.
I would also like to thank Dr. Tosi N. for providing guidance and for his patience during my internship.
I am also grateful to Dr. Montanari A. and Dr. Patrizii L. for their advice throughout the project.
Many thanks also to all the PhD students and other researchers who helped me with their suggestions.
Finally, I want also to thank my family, my friends and Anna for all the unconditional support and affection they have shown me, when I needed it most.